



HAL
open science

Atomistic contribution to the understanding of metallic and silica glasses

Pawel Koziatek

► **To cite this version:**

Pawel Koziatek. Atomistic contribution to the understanding of metallic and silica glasses. Materials. Université de Grenoble, 2014. English. NNT : 2014GRENI024 . tel-01293527

HAL Id: tel-01293527

<https://theses.hal.science/tel-01293527>

Submitted on 24 Mar 2016

HAL is a multi-disciplinary open access archive for the deposit and dissemination of scientific research documents, whether they are published or not. The documents may come from teaching and research institutions in France or abroad, or from public or private research centers.

L'archive ouverte pluridisciplinaire **HAL**, est destinée au dépôt et à la diffusion de documents scientifiques de niveau recherche, publiés ou non, émanant des établissements d'enseignement et de recherche français ou étrangers, des laboratoires publics ou privés.

THÈSE

Pour obtenir le grade de

DOCTEUR DE L'UNIVERSITÉ DE GRENOBLE

Spécialité : **Matériaux, Mécanique, Génie Civil, Electrochimie**

Arrêté ministériel : 7 août 2006

Présentée par

Paweł Koziatek

Thèse dirigée par **David RODNEY**

et codirigée par **Jean-Louis BARRAT**

préparée au sein **Laboratoire SIMaP**

et de l'**École Doctorale IMEP²**

Atomistic contribution to the understanding of metallic and silica glasses.

Contribution atomistique à la compréhension des verres métalliques et de silice.

Thèse soutenue publiquement le **28 mai 2014**,
devant le jury composé de :

Noel JAKSE

Professeur à Grenoble INP, Président

Anne TANGUY

Professeur à l'Université de Lyon, Rapporteur

Jörg ROTTNER

Professeur à l'Université de la Colombie-Britannique, Rapporteur

Peter DERLET

Senior Researcher à l'Institut Paul Scherrer, Examineur

David RODNEY

Professeur à l'Université de Lyon, Directeur de thèse

Jean-Louis BARRAT

Professeur à l'Université Joseph Fourier, Co-Directeur de thèse



Acknowledgements

I would like to thank the SIMaP laboratory for giving me the opportunity to carry out and successfully finish this project. It would not have been possible without the help of some key people. Foremost, I would like to express my sincere gratitude to David Rodney and Jean-Louis Barrat, my advisors. Their support, knowledge, experience and patience led me through the difficulties that emerged on the way. They have always been there to show the right direction and encouraged to dig deeper. Thank you for that. It will always be appreciated.

Claude Ghiotti and Claire Thomasson - once I heard that the complexity of a bureaucracy is inversely proportionate to the clarity of the idea behind it. With your help, this complexity seemed easy to figure out and entirely bearable. I would also like to acknowledge your understanding and patience towards my stubbornness to avoid speaking French.

I thank my friends from the lab: Achraf Kallel, Edouard Biguereau, Jérémy Croquesel, Denis Roussel, Zilin Yan, Leslie Lhomond, Natalia Kolebina, Emmanuelle Bichaud, Mathieu Suard, Benjamin Gadot, Robin Sarshad, Hareesh Tummala, Aaron Lichtner, Damien Lajoie, Samir Chandra Roy, Xavier Just, Sébastien Pinson and Anthony Papillon. Thank you guys for the time we shared together.

I also thank my fellow labmates at UJF: Francesco Puosi, Alexandre Nicolas, Hideyuki Mizuno, Sara Jabbari, Ezequiel Ferrero, Kirsten Martens, Marc Joyeux, Eric Bertin, Luca Marradi, Natalia Bedoya and Elian Masnada.

I appreciate the opportunity to work with and learn from the SIMaP staff members. They have always had time and willingness to help. I am very grateful for these three years.

Special thanks to Monika Krystian, Lena Zieniewicz, Bartłomiej Pilch, Konrad Koch, Jakub Kubica, Maciej Sufa, Jakub Zera, Wojtek Brodziński and Jakub Lewicki for our fruitful conversations and exchange of thoughts.

Last but not the least, I would like to thank my parents and siblings for supporting me throughout my life. I dedicate this dissertation to them.

CONTENTS

Acknowledgements	iii
Contents	iv
List of Figures	vii
List of Tables	xiii
Introduction en français	7
Introduction in English	13
1 Bibliography review	17
1.1 Glasses in history and life	17
1.2 How do we investigate glasses?	22
1.2.1 Experimental methods	22
1.2.2 Computer simulations	32
1.3 Potential Energy Landscape	38
2 Potentials and methods	47
2.1 Interatomic potentials	47
2.1.1 Wahnström potential	48
2.1.2 Kob-Andersen potential	50
2.1.3 BKS potential	51
2.1.4 Periodic boundary conditions	54
2.2 Potential Energy Landscape exploration	55
2.2.1 Molecular Dynamics	55
2.2.2 Transition State Theory	58
2.2.3 Activation-Relaxation Technique	60
2.2.4 Nudged Elastic Band	64
2.2.5 Autonomous Basin Climbing	67
2.3 Structural analysis of glasses	70

2.3.1	Voronoi tessellation	70
2.3.2	Rings statistics in silica glasses	72
3	Metallic glasses	77
3.1	Atomic structure of metallic glasses	79
3.1.1	Short range order	79
3.1.2	Influence of density and concentration of the atomic species	82
3.2	MD trajectories of metallic glasses	85
3.2.1	Return probabilities	85
3.2.2	Angular characteristics of escapes	88
3.2.3	Broken bonds	89
3.3	Thermally-activated processes	91
3.3.1	Distributions of activation energies and attempt frequencies	92
3.3.2	Meyer-Neldel compensation rule	94
3.3.3	Kinetics of metallic glasses	101
4	Silica glasses	107
4.1	As-quenched silica glasses	109
4.1.1	Structural characteristics	109
4.1.2	Potential energy landscape of as-quenched glasses	114
4.2	Evolution of SiO_2 under deformation.	119
4.2.1	Comparison with as-quenched silica glasses	132
4.2.2	Comparison with experiments	136
	Summary and perspectives	147
	Bibliography	149
	Résumé:	
	Abstract:	

LIST OF FIGURES

1.1	Critical casting thickness as a function of the year in which alloys were discovered [1].	19
1.2	A sample of Zr-based metallic glass [2].	19
1.3	High strength of metallic glasses combined with elasticity of polymers [2].	20
1.4	USB flash drive having a bulk metallic glass for its casing [3].	21
1.5	Golf clubs made of bulk metallic glass [4].	21
1.6	HRTEM image and SAED pattern of Cu-based metallic glass [5].	23
1.7	Bright-field image of the shear bands [6].	23
1.8	Electron nanodiffraction pattern from the Zr-Cu-Al metallic glass obtained with scanning transmission electron microscope [7].	24
1.9	SEM micrographs of the fracture morphology of the Fe-based amorphous rod [8].	25
1.10	SEM image of the shear bands in Zr-Cu-Ni-Al bulk metallic glass during tension [9].	25
1.11	Atomic arrangement in metallic glasses [10].	26
1.12	STM topograph of Zr-based metallic glass film [11].	27
1.13	Schematic illustration of potential energy landscape in two (left) and three dimensions (right) [12].	38
1.14	Local energy minimum located with steepest descent energy minimization [13].	40
1.15	Local energy minimum located with conjugate gradient method [13].	40
1.16	Inherent structure energy per particle during quenches at different rates [12].	42
2.1	Interactions between different types of particles for the Wahnström potential	49
2.2	Interactions between different types of particles for the Kob-Andersen potential	51
2.3	Interactions between different types of particles for the BKS potential	53

2.4	A two-dimensional periodic system. Figure reproduced from Ref. [14].	55
2.5	A two-state system illustrating the definition of the TST escape rate as the outgoing flux through the dividing surface between adjacent equilibrium states.	58
2.6	Pushing the system along a random direction until a negative eigenvalue appears.	61
2.7	An illustration of the NEB method by using the energy contour of a model system with two degrees of freedom. The dashed line represents an initially guessed MEP that links the initial (circle) and final (square) states of local energy minima. The solid curve is the converged MEP passing through the saddle point (star). Figure reproduced from Ref. [15].	65
2.8	Schematic illustration explaining the ABC method. Dashed and solid lines indicate original PEL and penalty potential, respectively. Figure reproduced from Ref. [16].	67
2.9	Construction of a two dimensional Voronoi polygon. Figure reproduced from Ref. [17].	71
2.10	The atomic packing configurations of different Voronoi polyhedra corresponding to the different CNs. Results taken from Ref. [18].	71
2.11	King's criterion in the rings statistics [19].	72
3.1	Metallic glass systems investigated in this dissertation. The cells on the left and on the right present Wahnström systems, the central cell visualizes a Kob-Andersen model glass.	78
3.2	Influence of quench rate on the cooling of Wahnström glasses.	79
3.3	Influence of quench rate on the cooling of Kob-Andersen glasses.	79
3.4	The fraction of different coordination numbers in Wahnström glasses as a function of a cooling rate.	80
3.5	The cooling rate dependence of the abundance of icosahedra in Wahnström glasses.	80
3.6	Population of the Voronoi polyhedra according to the type of atom in the centre.	81
3.7	Influence of atomic composition on the system energy.	83
3.8	Influence of density on the system energy (Kob-Andersen potential).	84
3.9	Molecular dynamics trajectory of a 100-atom Wahnström glass at $T = 0.43$. The magnified area is presented in the figure on the right.	85
3.10	A slice of the MD trajectory with probability of returning to a given metabasin.	85
3.11	Definition of angle θ between initial and final metabasins.	89
3.12	The dependence of $\cos \theta$ on the distance in configuration space between initial and final metabasins.	89

3.13	The fraction of broken bonds during the transitions to the highest intermediate state (left graph) and to the final minimum (right graph) as a function of distances between two states.	90
3.14	Influence of thermostat on system's dynamics.	90
3.15	Distributions of activation energies in glasses quenched at different rates.	93
3.16	Distributions of attempt frequencies in glasses quenched at different rates. The inset shows the distribution of eigenfrequencies (vibrational density of states) in the initial quenched glasses.	94
3.17	Relation between activation energy and attempt frequency within the hTST for thermally activated transitions in glasses consisting of 4000 atoms, quenched at different rates. For the sake of clarity, only two quench rates are shown.	96
3.18	Relation between activation energy and attempt frequency in 100-atom glasses quenched at different rates.	97
3.19	The comparison between 100 and 4000-atom systems quenched at the slowest rate.	97
3.20	Relation between activation energy and attempt frequency in 100-atom glass obtained with three different methods for identifying saddle points.	98
3.21	Attempt frequency in function of activation energy for 2000-atom Kob-Andersen system.	98
3.22	Relation between activation energy and attempt frequency near a plastic instability in a sheared glass (which corresponds to $E_A = 0$). The insets show the dependence of the activation energy and attempt frequency on the distance to instability.	100
3.23	Prediction of the escape rate in glasses quenched at different rates. The fits were obtained using only the lowest energy transition (dash-dotted lines) or the transitions with $k_B T_C$ from the lowest energy transition (dashed lines).	102
3.24	Twenty lowest energy barriers for glasses quenched at different rates. Filled circles represent the transitions within $k_B T_C$	102
4.1	Visualization of the amorphous silica system investigated in this study.	108
4.2	Energy per atom versus density for different densities and quench rates.	109
4.3	Pressure in function of density for different densities and quench rates.	109
4.4	Inter-tetrahedral angle $\theta_{Si-O-Si}$ in silica quenched at different pressures (in black). In red data from experiments.	110
4.5	$Si - O$, $O - O$ and $Si - Si$ bonds lengths versus density for the highest (dashed lines) and the lowest cooling rates (solid lines).	111

4.6	Coordination numbers of Si atoms as a function of density for the highest (dashed lines) and the lowest cooling rates (solid lines).	111
4.7	Percentage of rings of size n versus the cooling rate.	113
4.8	Percentage of rings of size n versus density.	113
4.9	Distributions of activation energies in silica glasses quenched at different rates when only oxygen atoms are involved ($X_{range} = 1.5\text{\AA}$).	115
4.10	Distributions of activation energies in silica glasses quenched at different rates when both Si and O atoms are involved ($X_{range} = 4.0\text{\AA}$).	115
4.11	Distributions of attempt frequencies in glasses quenched at different rates (for the $X_{range} = 4.0$).	116
4.12	Distributions of activation energies in silica glasses quenched at different densities at the slowest cooling rate ($X_{range} = 4.0$).	117
4.13	Relation between activation energy and attempt frequency within the hTST for thermally activated transitions in silica glasses quenched at two different rates.	118
4.14	Relation between pressure and density for quasi-static compression and unloads from chosen configurations at different pressures.	120
4.15	Relative volume variation after unloadings as a function of maximum pressure applied.	121
4.16	Inter-tetrahedral angle at ambient pressure as a function of the maximum pressure reached.	122
4.17	Coordination number of Si atoms as a function of pressure, during the compression (squares) and decompression (dashed lines) from 10 and 25GPa. Black lined denote changes obtained from the compression at 1200K.	122
4.18	Average coordination number of silicon atoms during the quasi-static compression (blue squares) and the decompression (dashed lines) from 10 and 25GPa.	122
4.19	Bonds lengths between Si and O atoms in function of the applied pressure for quasistatic compression and decompression from 10 and 25GPa.	124
4.20	Bonds lengths between oxygen atoms in function of the applied pressure for quasistatic compression and decompression from 10 and 25GPa.	124
4.21	Bonds lengths between silicon atoms in function of the applied pressure for quasistatic compression and decompression from 10 and 25GPa.	125
4.22	Comparison of the bonds lengths between atoms obtained from athermal compression (squares) and deformation at 1200K (diamonds).	125

4.23	Distribution of 3-, 4- and 5-membered rings in function of pressure (left) and density (right) for quasistatic compression (squares) and decompression from 10 and 25GPa (solid and dashed lines, respectively).	126
4.24	Distribution of 6- and 7-membered rings in function of pressure (left) and density (right) for quasistatic compression (squares) and decompression from 10 and 25GPa (solid and dashed lines, respectively).	126
4.25	Distribution of all rings sizes in function of pressure for quasistatic compression (squares) and deformation at constant strain rate (black solid lines for smaller and orange solid lines for larger rings).	128
4.26	Distributions of activation energies for quasistatic compression and decompression from 10 and 25GPa	129
4.27	Distributions of attempt frequencies for quasistatic compression and decompression from 10 and 25GPa	129
4.28	Relation between activation energy and attempt frequency for thermally activated transitions in different amorphous phases of silica glasses.	130
4.29	Vibrational density of states for different amorphous phases of silica.	131
4.30	Relation between pressure and density for quasi-statically compressed and as-quenched silica glasses.	132
4.31	Evolution of coordination number as a function of density for deformed glasses (squares) and as-quenched glasses (solid lines).	133
4.32	Evolution of coordination number as a function of pressure for deformed glasses (squares) and as-quenched glasses (solid lines).	133
4.33	Average coordination number as a function of density for deformed glasses (squares) and as-quenched glasses (solid line).	133
4.34	Average coordination number as a function of pressure for deformed glasses (squares) and as-quenched glasses (solid line).	133
4.35	Bond lengths as a function of density for deformed glasses (squares) and as-quenched glasses (dashed lines).	134
4.36	Bond lengths as a function of pressure for deformed glasses (squares) and as-quenched glasses (dashed line).	134
4.37	Evolution of small ring sizes as a function of density for deformed glasses (squares) and as-quenched glasses (solid lines).	135
4.38	Evolution of small ring sizes as a function of pressure for deformed glasses (squares) and as-quenched glasses (solid lines).	135
4.39	Evolution of small ring sizes as a function of density for deformed glasses (squares) and as-quenched glasses (solid lines).	135
4.40	Evolution of small ring sizes as a function of pressure for deformed glasses (squares) and as-quenched glasses (solid lines).	135

LIST OF TABLES

1.1	Experimental methods used to investigate structural properties of glasses.	31
2.1	Parameters of the Wahnström potential. The cut-off radius is expressed in units of the corresponding σ_{ij} . C_A and C_B are the concentrations of the two species.	50
2.2	Parameters of the Kob potential. The cut-off radius is expressed in units of the corresponding σ_{ij} . C_A and C_B meaning as in Table 2.1.	51
2.3	Parameters of the BKS potential.	54
2.4	Parameters used to search for saddle points with ART.	62
3.1	p_{back} 's and distances to metabasins for examples from Fig. 3.10.	88

Rodzicom

INTRODUCTION

Les matériaux amorphes sont omniprésents dans la vie quotidienne. Ils comprennent des verres "durs" et "mous". Les applications vont des vitres en silicate aux "matières plastiques" constituées essentiellement de polymères amorphes. Ces derniers permettent de synthétiser un dentifrice, diverses sortes d'émulsions, de pâtes, de mousses ou de matériaux granulaires. Certains - tels que les verres métalliques massifs - sont prometteurs pour de nouveaux matériaux avec de nombreuses applications potentielles. Mais la plupart sont importantes car elles sont déjà présentes à tous les niveaux de l'industrie et de la technologie. Les systèmes amorphes durs sont généralement considérés comme des matériaux de structure, dont les propriétés et l'utilisation sont comparable à celles des solides cristallins. Les verres mous sont généralement considérés comme des fluides complexes, décrits pour leurs propriétés rhéologiques et les applications correspondantes pratiques (béton, peintures, boues de forage, gels cosmétiques, crèmes ou de mousses, etc.). Les matériaux amorphes peuvent soit présenter un comportement de type solide ou de flux en fonction de leur charge mécanique: tous sont des fluides à limite apparente d'élasticité. Leurs limites d'utilisation sont souvent définies par l'apparition de bandes de cisaillement, une forme extrême de localisation vu dans des verres moléculaires ainsi que dans les matériaux granulaires. La similitude frappante de leur comportement macroscopique n'est pas fortuit. Il ya maintenant des preuves considérables que ce sont les conséquences de l'existence d'une structure désordonnée au niveau des constituants élémentaires (atomes, particules, ...). C'est la raison pour laquelle les matériaux amorphes peuvent être considérés comme une classe de systèmes, sous réserve d'un domaine particulier d'études. Par conséquent, la possibilité de prévoir l'organisation rhéologique et la

formation de divers modèles de déformation dans les matériaux amorphes subissant différents types de déformation est une question en suspens dans deux domaines de l'ingénierie - rhéologie d'un côté si l'on a affaire avec des matières molles colloïdales, et la plasticité d'autre part, pour les matériaux "durs".

L'activité existante dans le domaine de la rhéologie et de la plasticité des systèmes amorphes s'étend sur plus de trois catégories principales: le développement de techniques expérimentales non intrusives, le développement de modèles théoriques et l'approche numérique. La dernière catégorie, la simulation numérique à l'échelle atomique, est un sujet qui a été développé essentiellement dans les deux dernières décennies. Des simulations numériques se sont montrées cruciales dans les études de matériaux amorphes, car ils fournissent l'information locale critique qui est inaccessible par l'expérience, que ce soit des mesures de contraintes ou des modules locaux. La vitesse et la taille des systèmes simulés continuent, cependant, à poser des problèmes majeurs car il est difficile de parvenir à des situations qui peuvent réellement se comparer avec les expériences. Dans le cas des matériaux amorphes, cette difficulté est particulièrement critique car il y a de plus en plus de preuves que les mécanismes physiques qui régissent des problèmes tels que la localisation se produisent à des longueurs et à des échelles de temps qui sont au-delà des capacités actuelles des ordinateurs et des algorithmes.

Les études de la plasticité des solides amorphes, sont encore gênées par l'absence de tout défaut identifiable responsable de la réponse plastique. Il est maintenant reconnu que la plasticité est le résultat net des réarrangements locaux, ou "transformations de cisaillement", impliquant des petits groupes de (disons quelques dizaines de) particules. Mais c'est une observation après-coup: ces groupes n'ont ni frontières nettes, ni identité claire qui pourrait aider à prédire l'avance où la transition suivante se produira. Ces réarrangements sont thermiquement - activés et sont ubiquitaires dans le processus de relaxation de déformation structurelle des verres à basse température. Malheureusement, ils se déroulent sur des échelles de temps long par rapport à ceux qui sont accessibles aux simulations de dynamique moléculaire.

Certains nouveaux outils très prometteurs, cependant, ouvrent la voie vers des algorithmes accélérés pour la simulation de systèmes thermiques. Ils sont basés sur les méthodes numériques développées au cours de ces deux dernières décennies pour

déterminer les transitions thermiquement activés dans les systèmes atomiques. Un intérêt particulier ici est la technique d'activation-relaxation (ART) développé par N. Mousseau et ses collègues, une méthode de vecteur propre-suivant qui permet l'identification des états et des chemins activés dans le paysage de l'énergie potentielle des systèmes atomiques. Dans cette étude, nous allons montrer que, même si une recherche exhaustive des points de selle pour des solides désordonnés est impossible (en raison du nombre exponentiel d'états activés), ART peut identifier assez de points de selles pour construire des échantillons statistiquement pertinents, à partir desquelle des distributions stationnaires peuvent être calculées. En dehors d'ART, d'autres méthodes pour trouver les transitions thermiquement activés ont été utilisées pour le but de cette thèse. L'une d'elles est la méthode Nudged Elastic Band, qui sera décrit dans le chapitre 2. La méthode de NEB est utilisé pour trouver des voies de réaction lorsque les états initiaux et finaux sont tous les deux connus. Ces états ont été obtenues à partir de simulations de Dynamique Moléculaire à temperature constante de verres métalliques constitués de 100 et 4000 particules. Une autre méthode, appliquée à des systèmes de verre métalliques est la méthode Autonomoums Basin Climbing (ABC), développé comme une modification de la métadynamique.

Les verres métalliques ne sont pas le seul type de systèmes étudiés dans cette étude. Le deuxième type sont les verres de silice. Le but de cette thèse strictement numérique était de prédire les cinétiques thermiquement activées dans des verres telles que celles rencontrées expérimentalement. La nature de ces événements microscopique qui se produisent dans miscroscopic systèmes désordonnés a été étudiée à la fois sous des contraintes mécaniques et dans des conditions de vieillissement.

Le Chapitre 1 présente une bref historique des verres et de leur importance pour le genre humain. Il souligne les inconvénients et les avantages de ces matériaux et les applications possibles dans l'industrie. Plus loin dans ce chapitre, les méthodes expérimentales utilisées pour étudier les verres sont répertoriées. Une revue exhaustive n'est pas possible et n'est pas un objectif de cette thèse, donc cette partie est limitée aux familles de techniques qui aident à examiner les solides désordonnés sous des angles différents. La partie suivante du chapitre 1 traite de simulations informatiques et de leur importance pour l'étude des propriétés des verres à l'échelle

atomique. Une bref historique de l'utilisation des ordinateurs à des fins scientifiques est présenté et des techniques principales, largement appliquées par les chercheurs aujourd'hui. Le chapitre se termine par une section présentant le concept de paysage énergétique potentiel et son rôle dans de procédés thermiquement activés dans les systèmes désordonnés.

La première section du chapitre 2 montre et décrit les potentiels utilisés dans cette étude pour modéliser des systèmes vitreux. Les potentiels Wahnström et Kob - Andersen pour reconstruire les interactions entre les atomes dans des verres métalliques et le potentiel BKS sont introduits pour représenter les interactions entre les atomes dans les silicates . La deuxième section présente les méthodes et les théories sur lesquelles nous nous sommes appuyées dans nos enquêtes. La section comprend les descriptions des techniques telles que la dynamique moléculaire, Activation–Relaxation Technique, Nudged Elastic Band et Autonomous Basin Climbing. Il décrit également la théorie de transition d'état (et son approximation harmonique), qui a été utilisé pour faire face à l'un des principaux problèmes de simulations de dynamique moléculaire , à savoir un limitation d'échelle du temps. Outre les processus activés thermiquement, les analyses structurelles de verres métalliques et de silice ont été réalisées. Les ordres de courte et moyenne portée ont été caractérisées par deux méthodes: pavages de Voronoi pour les verres métalliques, nous fournissant des informations sur les conformations voisines proches, et dans le cas de la silice, les statistiques de distributions de chaînes moléculaires.

Le Chapitre 3 contient les résultats de l'enquête des verres métalliques. Le chapitre commence par une analyse de la structure à courte portée l'influence de la composition atomique et la densité sur le niveau de relaxation des verres et structures. Dans la deuxième partie, l'enquête des trajectoires MD pour un système de 100 atomes est présentée. Cette partie de l'étude a été axée sur le concept de probabilités de retour proposés par Doliwa et Heuer pour des températures autour de la température de couplage de mode. Nous montrons que la fuite d'un metabasin (structure sur la surface de l'énergie potentielle décrite dans le chapitre 1) ne se fait pas par un passage de la barrière unique entre deux minima longue durée de vie, mais plutôt par un certain nombre d'états intermédiaires de courte durée. En outre, dans cette section, ces passages sont analysés en termes de liens rompus et de

dépendances angulaires sur la distance dans l'espace de configuration entre deux états d'équilibre visités. Dans la dernière partie de ce chapitre, les événements thermiquement activés sont caractérisés. Nous étudions deux grandeurs décrivant ces événements au sein de l'approximation harmonique de la théorie de l'état de transition, c'est à dire l'énergie d'activation et la fréquence d'attaque. Etant donné que dans la définition d'une fréquence d'attaque la courbure du minimum initial et le point de selle sont présents, nous voulions voir s'il y avait une relation entre les fréquences de tentative et les énergies d'activation d'un événement donné. Cette corrélation a été précédemment observée pour un large éventail de phénomènes et est appelé la règle de compensation Meyer-Neldel. Il se termine par l'analyse de la cinétique de verres métalliques et montre qu'il est possible d'être décrit avec une seule énergie d'activation et d'un fréquence d'attaque effective, au moins à basse température.

Le dernier chapitre présente les résultats obtenus pour les verres de silice. Dans ce chapitre, les structures à court et à moyen terme d'un système de 3000 atomes de verre de silice en fonction de la vitesse de refroidissement, de la densité et de la pression ont été étudiées. Nous tentons de répondre si le simple potentiel BKS sans sommation d'Ewald est capable de reproduire le polyamorphisme observé dans les verres de silice soumis à une compression hydrostatique et caractérisé principalement en termes de nombres de coordination. Ici, la distribution de chaînes moléculaires et du paysage d'énergie potentielle sont également considérés dans la description des différences dans la structure du verre sous pression. La variation de la masse volumique a été obtenue de deux façons: par la trempe des verres directement à différents volumes ou par compression un verre de faible densité initiale. Nous montrerons aussi que la dépendance des fréquences d'attaque sur les énergies d'activation des processus thermiquement activés dans les verres de silice est en ligne avec la règle de compensation Meyer-Neldel, contrairement aux résultats obtenus pour les verres métalliques.

INTRODUCTION

Amorphous materials are ubiquitous in everyday life. They comprise "hard" and "soft" glasses: the former range from silicates forming window panes to the amorphous polymers that constitute the bulk of most "plastics". The latter include toothpaste, various sorts of emulsions, pastes, foams, or granular materials. Some—such as bulk metallic glasses—are promising new materials with many potential applications, but most are important because they are already present at all levels of industry and technology. Hard amorphous systems are usually seen as structure materials, with properties and use comparable to those of crystalline solids. Soft glasses are usually seen as complex fluids, described in terms of their rheological properties with the corresponding practical applications (concrete, paints, drilling mud, cosmetic gels, creams or foams, etc). Amorphous materials can either present a solid-like behaviour or flow depending on their mechanical load: all are yield-stress fluids. Their usage limits are often defined by the occurrence of shear-banding, an extreme form of localization seen in molecular glasses as well as in granular materials. The striking similarity of their macroscopic behaviour is not fortuitous. There is now considerable evidence that they are consequences of the existence of a disordered structure at the level of the elementary constituents (atoms, particles,...). This is the reason why amorphous materials can be seen as a class of systems, subject of a particular field of studies. Therefore the possibility of predicting the rheological organisation and the formation of various deformation patterns in amorphous materials undergoing various types of deformation is an outstanding question in two fields of engineering—rheology on one side if one is dealing with soft, colloidal materials, and plasticity on the other hand for "hard" materials.

The existing activity in the field of rheology and plasticity of amorphous systems spans over three main categories: development of non intrusive experimental techniques, development of theoretical models and numerical approach. The last category, atomic scale numerical simulation, is a topic that has been developed substantially in the last two decades. Numerical simulations have proven crucial in studies of amorphous materials, as they provide critical local information which is inaccessible to experiments, such as measurements of local stresses and moduli. The speed and size of simulated systems continue, though, to pose major problems as it is difficult to reach situations which can actually compare with experiments. In the case of amorphous materials, this is particularly critical as there is growing evidence that the physical mechanisms which govern problems such as localization occur at length- and time-scales which are beyond the current capacities of computers and algorithms.

Studies of plasticity in amorphous solids, are still hampered by the lack of any identifiable defect responsible for the plastic response. It is now acknowledged that plasticity is the net result of local rearrangements, or "shear transformations", involving small clusters of (say a few tens of) particles. But this is an after-the-fact observation: these clusters have neither sharp boundaries, nor clear identity that could help tell beforehand where the next transition will occur. These rearrangements are thermally-activated and are ubiquitous processes in the structural relaxation and deformation of glasses at low temperatures. Unfortunately, they take place over timescales long compared to those accessible to direct Molecular Dynamics simulations.

Some extremely promising new tools, however, are opening the route towards accelerated algorithms for the simulation of thermal systems. They are based on numerical methods developed over these last two decades to determine thermally activated transitions in atomic systems. Of particular interest here is the Activation-Relaxation Technique (ART) developed by N. Mousseau and co-workers, an eigenvector-following method that allows the identification of activated states and paths in the potential energy landscape of atomic systems. In this study, we will show that although an exhaustive search for saddle points in case of disordered solids is unfeasible (because of the exponential number of activated states), ART can identify enough saddles to build statistically relevant samples,

from which stationary distributions can be computed. Apart from ART, other methods to investigate thermally-activated transitions were used for the purpose of this dissertation. One of them is the Nudged Elastic Band method, which will be described in Chapter 2. The NEB method is used to find reaction pathways when both the initial and final states are known. These states were obtained from finite-temperature Molecular Dynamics simulations of model metallic glasses consisting of 100 and 4000 particles. Another method, applied to metallic glass systems is the Autonomous Basin Climbing (ABC) method, developed as a modification of metadynamics.

Metallic glasses were not the only type of systems investigated in this study. The second type were silica glasses. The purpose of this strictly numerical thesis was the prediction of thermally activated kinetics in glasses such as those encountered experimentally. The nature of such microscopic events occurring in disordered systems was studied both under mechanical stress and in ageing conditions.

Chapter 1 presents a brief history of glasses and their importance for man kind. It points out the downsides and upsides of these materials and possible applications in the industry. Further in this chapter, the experimental methods used to study glasses are listed. An exhaustive review is not possible and is not a goal of this thesis, therefore that section is limited to the families of techniques that help examine disordered solids from different angles. The next part of Chapter 1 deals with computer simulations and their importance for investigating the properties of glasses at atomic scale. A short history of using computers for scientific purposes is presented and main techniques, broadly applied by researchers nowadays. The chapter ends with a section presenting the concept of potential energy landscape and its role in investigating thermally activated processes in disordered systems.

The first section of Chapter 2 shows and describes the potentials used in this study to model glassy systems. The Wahnström and Kob-Andersen potentials to reconstruct interactions between atoms in metallic glasses and the BKS potential introduced to represent the interatomic interactions in silicates. The second section presents methods and theories that we relied on for our investigations. The section includes the descriptions of the techniques such as Molecular Dynamics, Activation-Relaxation Technique, Nudged Elastic Band and Autonomous Basin

Climbing. It also outlines the Transition State Theory (and its harmonic approximation), which was used to deal with one of the main problems of MD simulations, i.e. the timescale limitation. Apart from thermally activated processes, the structural analyses of metallic and silica glasses were performed. The short and medium range orders were characterized using two methods: Voronoi tessellations for metallic glasses, providing us information about near neighbor conformations, and in case of silica, statistics of ring distributions.

Chapter 3 contains the results from investigation of metallic glasses. The chapter begins with an analysis of the short range structure and the influence of atomic composition and density on the level of glass relaxation and structure. In the second part, the investigation of MD trajectories for the 100-atom system is presented. This part of the study was focused on the concept of return probabilities proposed by Doliwa and Heuer for temperatures around the mode coupling temperature. We show that the escape from a metabasin (structure on the potential energy landscape described in Chapter 1) does not happen by a single barrier crossing between two long-lived minima, but rather a number of short-lived intermediate states. Further in this section, these crossings are analysed in terms of broken bonds and angular dependencies on the distance in configuration space between two visited equilibrium states. In the last part of this chapter, thermally activated events are characterized. We investigate two quantities that describe such events within the harmonic approximation of the transition state theory, i.e. activation energy and attempt frequency. Since in the definition of an attempt frequency the curvature of the initial minimum and the saddle point are present, we wanted to see if there was a relation between attempt frequencies and activation energies of a given event. Such correlation had been observed before for a wide range of phenomena and is referred to as the Meyer-Neldel compensation rule. The chapter ends with the analysis of the kinetics of metallic glasses and shows that it is possible to be described with a single effective activation energy and attempt frequency, at least at low temperatures.

The last chapter presents the results obtained for silica glasses. In this chapter the short- and intermediate-range structures of a 3000-atom silica glass system as a function of cooling rate, density and pressure was investigated. We attempt to answer if the simple BKS potential without Ewald summation is able to reproduce

polyamorphism observed in silica glasses subject to hydrostatic compression and characterized mainly in terms of coordination numbers. Here, the ring distribution and potential energy landscape are also considered in describing the differences in the glass structure under pressure. The change in density was obtained in two ways: by quenching glasses directly at various volumes or by compressing an initial low density glass. We will also show that the dependence of attempt frequencies on activation energies for thermally-activated processes in silica glasses is in line with the Meyer-Neldel compensation rule, as opposed to the results obtained for metallic glasses.

BIBLIOGRAPHY REVIEW

1.1 Glasses in history and life

The role of glasses in our everyday life has been essential for thousands of years. Volcanic obsidian glass was used by the human kind for carving knives, arrows and other tools necessary to survive. The first objects made of glass produced by man date back from around 7000 B.C. [20]. Approximately 5500 years later the first glass vessels were made. The technique used to manufacture glassware was simple. Molten glass was formed around a molded core of clay. When the material cooled down, the core was removed leaving a ready glass dish [20]. Glass applications for practical purposes vastly increased after inventing the technology of glass blowing in the first century B.C.. This method was developed and widely used by the Romans throughout the Empire. After the fall of the latter, glass manufacturing was continued in the Middle East and in the West. From about 1300 and later, Venice became the center of a glass industry in the western world. The craftsmen were able to produce the glasses needed for lenses and mirrors. By the XVIIIth century glass products became very popular and glass makers were spread all over Europe.

In the 1800's the scientists began to study glasses in a more insightful way. Amongst the most successful were Michael Faraday and Heinrich Buff who worked on the electrolysis and conductivity of glasses, Gustav Tamman, working on viscosity and the glass transition and Otto Schott developing glass technology. In

1856 Justus von Liebig, a German chemist, invented the silver mirror [21, 22]. In 1918, Emile Fourcault from Belgium and Irving Colburn from the USA invented independently the technique to produce sheet glass. Over forty years later the float glass process was introduced, improving the mass production of flat glasses [23].

Until 1960 highly disordered arrangements of the atoms had never been observed in solid metals and alloys. Amorphous configurations could be retained in the solid state for some metalloids by cooling from the melt fast enough to prevent crystallization [24]. It was suspected that such non-crystalline structures might be obtained also for metals and alloys using the same technique. In 1960, at the California Institute of Technology, Pol Duwez and co-workers discovered that if a liquid metal is undercooled uniformly and rapidly, the atoms do not have enough time for crystal nucleation. They employed a rapid cooling process to successfully create a thin $Au_{80}Si_{20}$ alloy [2, 24]. This ribbon-like form of amorphous metal caught on. Since then amorphous metals and their composites have produced extensive scientific and commercial interests [2, 25, 26]. In 1969, Chen and Turnbull formed amorphous spheres consisting of three components, Pd- M -Si with $M=Ag, Cu$ or Au [27] at critical cooling rates of 100 K/s to 1000 K/s. The alloy $Pd_{77.5}Cu_6Si_{16.5}$ could be made glassy with a diameter of 0.5 mm and the existence of a glass transition was demonstrated. Extending the supercooled liquid regime (between the crystallization and glass transition temperatures) up to 40K in some Pd-Cu-Si and Pd-Ag-Si alloys enabled the first detailed studies of crystallization in metallic glasses [1, 2]. Chen also conducted systematic researches on Pd- M -P alloys with $M=Ni, Co$ or Fe , obtaining in 1974 a critical casting thickness of 1 mm [28] and a slightly greater thickness in $Au_{55}Pb_{22.5}Sb_{22.5}$ in 1982 [29]. In the early 1980s, glassy ingots of $Pd_{40}Ni_{40}P_{20}$ with a diameter of 5 mm were produced by the Turnbull group using surface etching followed by heating and cooling cycles. In 1984, the same group extended the critical casting thickness of this alloy to 1 cm by processing in a boron oxide flux [30]. $Pd_{40}Ni_{40}P_{20}$ can therefore be considered as the first bulk metallic glass. An overview of critical casting thickness and the date of discovery is presented in Fig. 1.1.

Since the 1980s, the Inoue group of Tohoku University and the Johnson group of Caltech have discovered strongly glass forming multi-component La-, Mg-, Zr-, Pd-, Fe-, Cu- and Ti-based alloys with low critical cooling rates of 1 K/s to 100 K/s, enabling a larger critical casting thickness [2]. In 1988, while studying rapid solidification in rare-earth materials mixed with ferrous metals, Inoue's group

found exceptional glass-forming ability in La-Al-Ni and La-Al-Cu alloys, reaching the critical casting thickness of 9 mm [31]. In 1991, the same group developed glassy Mg-Cu-Y and Mg-Ni-Y alloys with the highest glass-forming ability obtained in $Mg_{65}Cu_{25}Y_{10}$ [32]. An extended supercooled region of 127 K was achieved for the family of Zr-based alloys having high glass-forming ability and thermal stability. The critical casting thickness in these alloys ranged up to 15 mm [33].

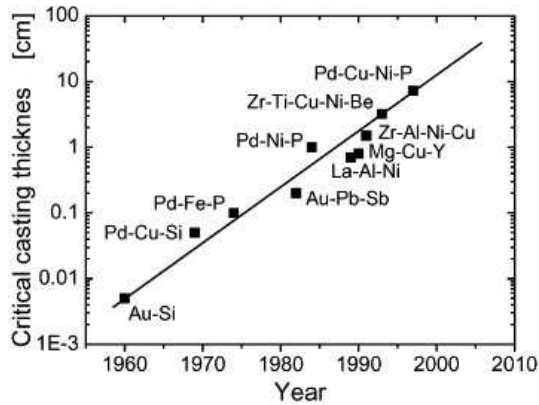


FIGURE 1.1: Critical casting thickness as a function of the year in which alloys were discovered [1].



FIGURE 1.2: A sample of Zr-based metallic glass [2].

It showed that metallic glasses could be quite interesting for engineering applications. In 1993, the Johnson and Piker group developed the quinary alloy $Zr_{41.2}Ti_{13.8}Cu_{12.5}Ni_{10}Be_{22.5}$, commonly known as *Vitreloy 1* [34] (see Fig. 1.2). The casting thickness reached several centimeters. This work along with Inoue's work can be regarded as the starting point for the use of bulk metallic glasses in commercial applications. In 1997, the Inoue group continued their work with $Pd_{40}Ni_{40}P_{20}$ replacing 30% of Ni by Cu. As a result, alloy rods up to 72 mm in diameter were obtained [35]. The Pd-Cu-Ni-P family is the metallic system with the highest glass-forming ability yet known, exhibiting the lowest cooling rate (0.067 K/s) and reaching a critical thickness of 85 mm [36–39].

Fig. 1.1 depicts the critical casting thickness as a function of the year the corresponding alloy was introduced. It increased by more than three orders of magnitude since the first experiments by Duwez and others and the trend is the increase by an order of magnitude every 10–12 years. Currently, many scientists are searching for new alloy compositions and investigating their mechanical, structural, thermophysical and magnetic properties. Research is aimed at increasing

the concentration of light elements such as Ti, Al and Mg in environmentally safe, Be-free Zr-based alloys [2].

It has been shown that metallic glasses are stronger than their crystalline counterparts and many other materials [2, 40, 41] (see Fig. 1.3). The highest strength known to date exceeds 5 GPa [42]. Amorphous metals show high hardness but relatively low fracture toughness and low ductility which is due to the localization of the plastic deformation in thin shear bands where local heating leads to decohesion and catastrophic failure [12, 43]. The mechanical properties of bulk metallic glasses are extremely dependent on material quality, oxygen content and the presence of unwanted phases or partial crystallization [44, 45].

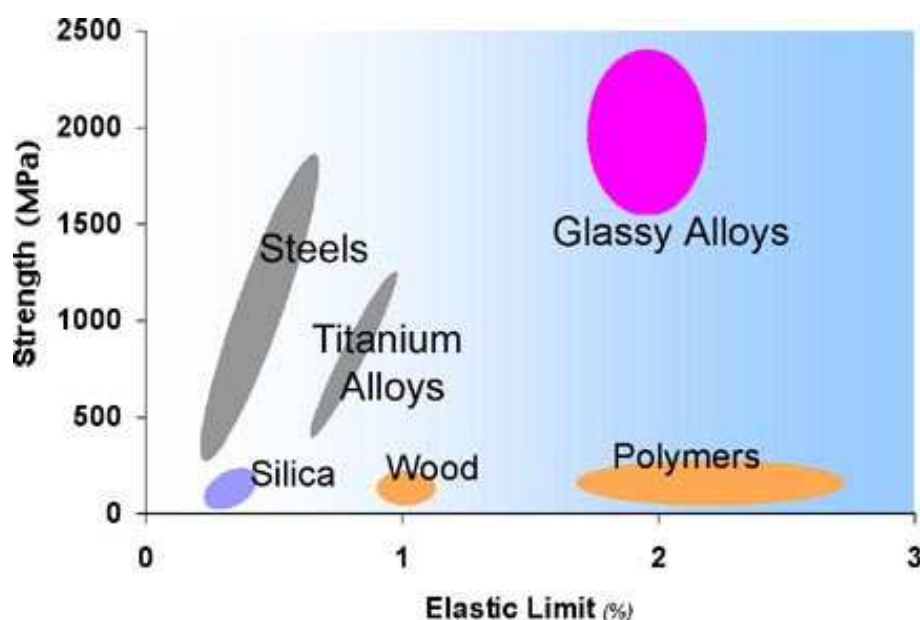


FIGURE 1.3: High strength of metallic glasses combined with elasticity of polymers [2].

Hence, the present cost of components and processing is high and the products, to be cost-competitive, are made of material of lower quality. The development of bulk metallic glasses using low-cost alloy compositions, such as for instance Cu-Zr-Al, opened the door for many commercial implementations [39]. The first application was a golf club head (Fig.1.5). Thanks to the elastic properties of metallic glasses, 99% of the impact energy from a head is transferred to the ball, whereas for Ti-based heads it is only 70%. Higher strength-to-weight ratio allows mass to be distributed differently and enables various shapes and sizes of head.

Targeting leisure equipments that require good rebound, many commercial corporations started to use metallic alloys to produce baseball and softball bats. HEAD was the first company to use Vitreloy in tennis rackets.



FIGURE 1.4: USB flash drive having a bulk metallic glass for its casing [3].



FIGURE 1.5: Golf clubs made of bulk metallic glass [4].

This increased stiffness, enhancing energy return with 29%. Other potential applications in sports include fishing equipment, hunting bows, guns, bicycle frames, snowboards and marine applications [2].

The lack of grain structure and associated microstructural features provide corrosion resistance and high precision in casting [41]. Because of that metallic glass components are used to fabricate casings for flash drives (see Fig.1.4), digital cameras and computer screens. Vitreloy can also be used for watch cases and jewellery to replace Ni and other metals, which can cause allergic reactions. High hardness and corrosion resistance give good durability, enabling production of smooth, hard coatings. Corrosion- and wear-resistance also make metallic glasses excellent materials for medical applications. They are used in knee-replacement devices, scalpel blades and also non-medical, edged tools, such as knives and razor blades [2, 39].

Attempts are being made to develop military materials based on metallic alloys, that would be stronger and lighter. This includes metallic-glass-composite Kinetic Energy Penetrator (KEP) rod . The KEP is the key component of the highly effective armor-piercing ammunition system. Also casings for lightweight fragmentation bombs and metallic-glass-composite armor tiles are on the wishlist of the army.

The flaws in the metallic alloy materials, indicated above, began research shifted towards toughening strategies for bulk metallic glasses. In the early 2000s, progress

was made by recognizing that the brittle failure of such alloys could be attenuated with the addition of crystalline phases into metallic glass matrix [46]. The first alloy of metallic glass to exhibit both the high tensile strength and increased ductility consisted of 60% of bulk metallic glass and 40% of bcc¹ crystalline inclusions [47]. Therefore based on the present developments, one can expect further major applications of metallic glasses in the near future.

1.2 How do we investigate glasses?

1.2.1 Experimental methods

The role of experiments has always been essential for our understanding of processes and phenomena in nature. The experimental methods are the only methods of research that can truly test hypotheses concerning cause-and-effect relationships. With the advent of metallic glasses, there was a need for incorporating appropriate research methods to study their properties. The key factor determining physical properties and practical applications of metallic glasses is their atomic structure. In most cases, metallic glasses are complex, multi-component systems, which essentially limits possibilities of the structural investigations.

Different experimental techniques have been proposed to elucidate the atomic structure of glassy alloys. Local structural analyses are usually carried out by means of advanced **transmission electron microscopy (TEM)**, or **scanning electron microscopy (SEM)** [48, 49].

Transmission electron microscopy is a method in which electrons, accelerated to high energy levels (typically few hundreds of keV) are focused by electrostatic and electromagnetic lenses and transmitted through the specimen that is in part transparent to electrons and in part scatters them out of the beam [50]. One of the advantages of using modern TEM is the possibility to obtain structural information from local regions as small as 1 nm by using **nanobeam electron diffraction (NBED)** in combination with high resolution imaging [48, 51, 52]. Thanks to this technique a presence of extended medium range order (MRO) structures and their sensitivity to alloy composition were proved [53, 54]. Moreover, average structural information, such as including local atomic coordinations, can also be obtained

¹bcc (body centered cubic)-a crystal structure where atoms are arranged at the corners of the cube with another atom at the cube center

precisely by **selected area electron diffraction (SAED)** patterns from wide areas ($0.1 \sim 1\mu\text{m}$) of the specimens. SAED is used for indicating sites containing crystalline inclusions in toughened metallic glasses [48].

Transmission electron microscopy is one of the most useful tools for studying defects, such as dislocations, in crystalline metals. Defects are also important in amorphous materials, but the fact that these alloys are disordered makes the identification and characterization of defects by the means of TEM difficult [55]. Some progress has been made towards developing TEM techniques for imaging defects in amorphous materials. **High-resolution transmission electron microscopy (HRTEM)** has been applied to investigate nanometer-scale defects in shear bands in bulk metallic glasses [55]. The exemplary image of a Cu-based metallic glass obtained from HRTEM is depicted in Fig. 1.6. The formation of shear bands and deformation mechanisms in metallic glasses in general have always attracted attention from both experimental and theoretical side [6, 56–58]. The carried out TEM experiments, however, were not very successful, because of relatively small and therefore difficult to detect structural changes in shear bands.

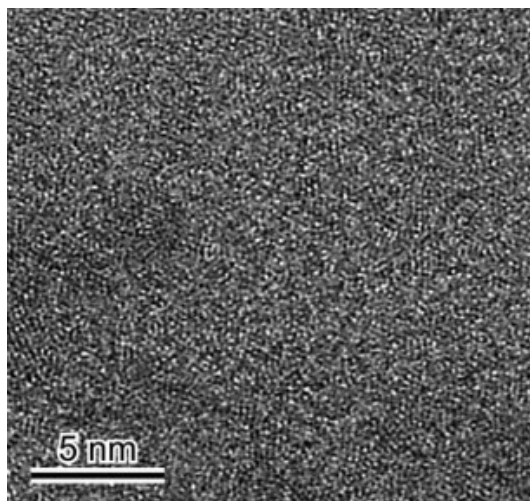


FIGURE 1.6: HRTEM image and SAED pattern of Cu-based metallic glass [5].

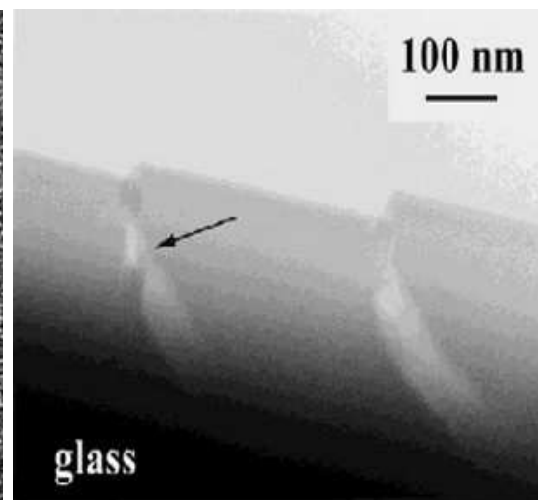


FIGURE 1.7: Bright-field image of the shear bands [6].

A very good approach turned out to be propagation study of shear bands in thin films of material without successive thinning, using **bright- and dark-field transmission electron microscopy** (see Fig. 1.7). **Bright field imaging** is the simplest optical microscopy method. A sample is illuminated by unpolarized white light and the contrast in the image results from direct interaction of the

probing light with the sample (absorption, refraction, scattering, reflection, etc.). The name of the method comes from the typical appearance of images obtained with it, namely a dark sample on a bright background [59–62].

Dark field microscopy is a method in which the image is formed by collecting only the light scattered by the sample. All unscattered light coming directly from the illumination source is excluded from the image. This produces the classic appearance of a dark, almost black, background with bright objects on it [62, 63]. The application of bright-field and dark-field techniques revealed the reduction in density of the material in shear bands [6].

The effects of oxygen impurities and microalloying on the microstructure of metallic glasses are characterized by **scanning transmission electron microscopy (STEM)**, which was developed at about the same time as TEM [64, 65]. STEM provides information on elemental composition and electronic structure at the ultimate sensitivity of a single atom. The scanning process is the mechanism which allows to use small probes to build images of large areas [66]. This method works by forming a focused beam of electrons that is scanned over the sample while some desired signal is collected to form an image [67]. Dedicated STEM instruments permit much higher resolution microanalysis than previously attainable in TEM and are also easier to use.

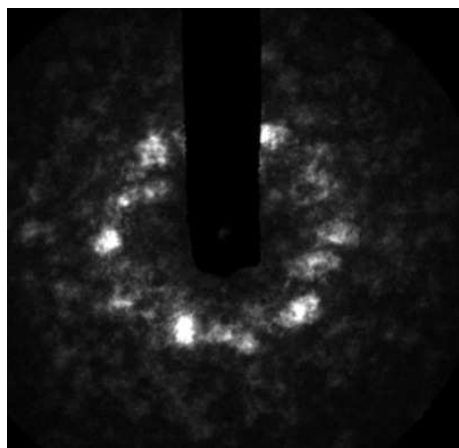


FIGURE 1.8: Electron nanodiffraction pattern from the Zr-Cu-Al metallic glass obtained with scanning transmission electron microscope [7].

By using STEM it is possible to obtain images with the contrast directly related to the atomic number, whereas for example HRTEM produces results that need to be interpreted by simulation [68]. Thanks to state-of-the-art scanning transmission electron microscope it has been lately shown that in addition to clusters of pentagons, metallic glasses are arranged in clusters of squares and hexagons (see Fig. 1.8) [7, 69].

One of the methods working on the same principle as STEM is **scanning electron microscopy (SEM)**. SEM is a powerful method for the investigation of surface structures of conducting bulk metallic glasses [8, 70]. This technique provides a large depth of field, which implies that an area of the sample can be viewed in focus but

the resolution of SEM is not high enough to image individual atoms. In order to produce images the electron beam is focused into a probe, which is scanned across the surface of the specimen with the help of scanning coils. The most common imaging mode collects low-energy (less than 50eV) secondary electrons that are ejected from the atoms by inelastic scattering interactions with beam electrons.

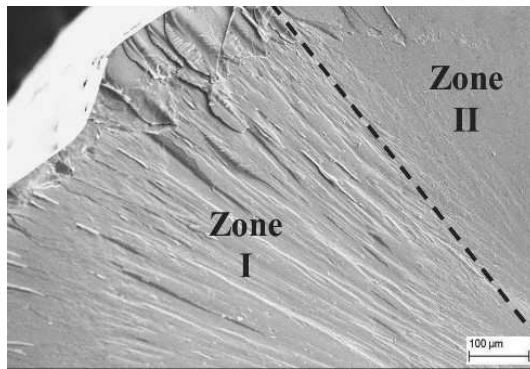


FIGURE 1.9: SEM micrographs of the fracture morphology of the Fe-based amorphous rod [8].

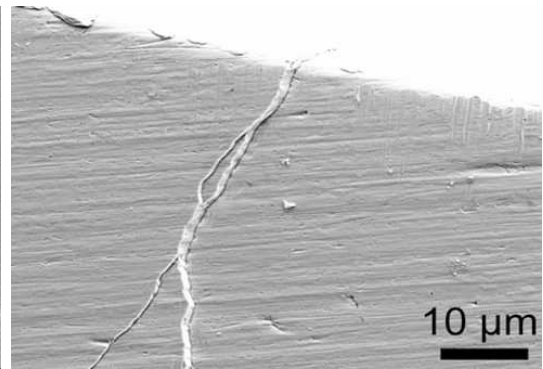


FIGURE 1.10: SEM image of the shear bands in Zr-Cu-Ni-Al bulk metallic glass during tension [9].

Due to their low energy, these electrons originate within nanometres to micrometres from the sample surface. Specimens can be observed in high vacuum, in low vacuum, and in wet conditions. [71, 72]. SEM examination of amorphous Fe-based rods revealed that the fracture surface consist of two different zones, which suggests different amorphous structures of the studied glassy samples (Fig. 1.9) [8]. SEM is also used to follow the initiation and evolution of shear bands (Fig. 1.10) [9].

Using **fluctuation electron microscopy (FEM)**, the researchers found that the structure of this Zr-based glass was not random, but composed in large part by efficiently arranged 13-atom icosahedral clusters [10, 73]. Icosahedra have 20 faces, 12 vertices and 12 axes of five-fold symmetry but they cannot be packed into an ordered, three-dimensional crystalline structure (see Fig. 1.11). FEM is a transmission electron microscopy technique for studying medium-range order in disordered materials, including amorphous silicon and germanium and oxide glasses [73–75]. The fluctuations being studied are the differences in structural arrangement and orientation between small sub-volumes within the thin sample [76]. There are two equivalent ways to conduct FEM experiments: by collecting tilted dark field images from a thin amorphous sample or by using the STEM

mode [76]. In case of Zr-based metallic glasses FEM has been used to study shear bands [75].

The surface structure of metallic glasses can also be studied by **scanning tunneling microscopy (STM)**. This method is well known for imaging topographic and electronic features of surfaces with high resolutions ($0.01nm$ for vertical and $0.1nm$ for lateral [11]). It allows to find topographic structures correlated over a distance of several nanometers and is based on quantum tunneling [77].

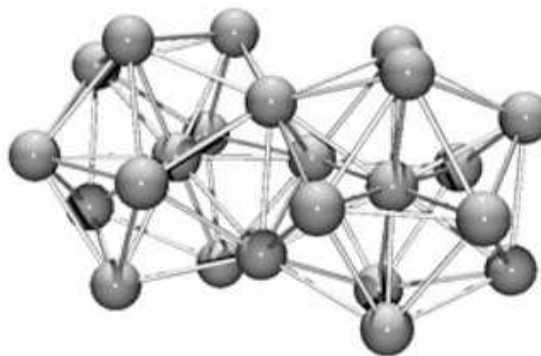


FIGURE 1.11: Atomic arrangement in metallic glasses [10].

The interpretation of STM images (see Fig. 1.12) is often complicated by distortions resulting from the non-negligible size of the probe tip and the topographs tend to underestimate the sharpness and depth of surface features [78]. Scanning tunneling microscopy has also been applied to perform experiments on the surface crystallization of metallic glasses, which has been observed to occur even at temperatures far below the temperature of any crystallization event in the bulk [79, 80]. It allows to investigate phase transformation at the surface of bulk metallic glasses from initial nucleation to full crystallization [81].

Following on from invention of scanning tunneling microscope, the **atomic force microscope (AFM)** was invented in 1986 by G. Binnig, C. F. Quate and Ch. Gerber [82, 83]. They proposed a new tool allowing to obtain images with a resolution of a single atom. The basic principle of AFM is to measure the force experienced by a very sharp tip under the action of intermolecular interactions with atoms of the sample surface. This technique is invaluable for performing surface height measurements with precision better than $0.1nm$. For that reason, AFM became a widely used tool to detect surface defects and measure surface roughness in glasses [82]. Performing atomic force microscopy on the deformation regions in metallic glasses allows to show the height of shear bands [84]. AFM is also an appropriate tool for imaging the topographic changes of glass surfaces undergoing corrosion by the attack of air and water [82].

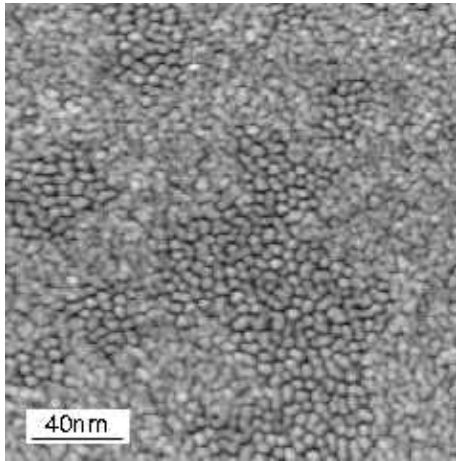


FIGURE 1.12: STM topograph of Zr-based metallic glass film [11].

Another method used in the characterization of amorphous materials belongs to a family of X-ray scattering techniques. This method, called **Small-angle X-ray scattering (SAXS)**, is a technique where the X rays scattered elastically by a sample are recorded at very low angles [85]. SAXS is used for the determination of the microscale or nanoscale structure of particle systems in terms of such parameters as averaged particle sizes, shapes, distribution, and surface-to-volume ratio. It is the most direct way to observe structural inhomogeneities occur-

ing on length scales defining medium range order ($\sim 10 - 1000\text{\AA}$). SAXS is also able to detect phase separation in amorphous alloys [86, 87]. The method is accurate, non-destructive and usually requires only a minimum of sample preparation.

In materials such as glasses, it is this local, atomic structure that governs the properties of the system in overall. A very powerful technique to obtain structural, atom specific information even for the most complex multicomponent systems is **extended X-ray absorption fine structure (EXAFS)** [88]. In this method X-rays are transmitted through a sample and when the x-ray energy matches the binding energy of an electron to an atom within the sample, the number of absorbed x-rays highly increases causing a drop in the transmitted x-ray intensity. This results in an absorption edge. Each element from the periodic table has unique absorption edges and it is possible to quantify the number of atoms of a particular element and their distances from an atom indicated by the absorption edge. Since EXAFS requires a tunable x-ray source, data are always collected at synchrotrons, often at beamlines which are especially optimized for their purpose. As a short range technique, EXAFS is able to give information on the average interatomic distances and the compaction rate of local atomic packing in glassy systems (it was shown for example that Cu-Zr metallic glass has a more compact atomic structure than Ni-Zr) [89].

To investigate the structure of various amorphous solids at a mesoscopic scale, an experimental technique employing **elastic neutron scattering at small scattering angles (SANS)** is used [90]. SANS arises from different kinds of inhomogeneities, such as density or concentration fluctuations, segregation, impurities or

surface states [91]. Using SANS, growth mechanisms in materials and soft matter phase transitions can also be explored [92]. Small angle neutron scattering is in many respects very similar to SAXS but one of the advantages of SANS over SAXS is its sensitivity to light elements [90, 93]. During a SANS experiment a beam of neutrons is directed at a sample and neutrons are elastically scattered by interaction with the nuclei (and this interaction depends on isotope) or through interaction of unpaired electrons with the magnetic moments of the neutrons [94]. SANS has evolved into a powerful method for the study of different kinds of materials and thus it has been widely used by industrial scientists. It allows to compute volume fractions of each component in two-phase systems and (along with x-ray scattering techniques) showed that silica glasses have corner-sharing tetrahedral structure with well-defined Si-O bond lengths and O-Si-O angles [95].

For the understanding of thermodynamics, transport and other properties of amorphous systems on a microscopic level, knowledge of their atomic structure and dynamics on the basis of interatomic forces is required [96]. Interatomic forces can be studied by **inelastic scattering** experiments if the energy change of the scattered particle can be directly related to the atomic dynamics of the system. Neutrons are especially suited for this kind of investigations because their energies match those of diffusive and vibrational motion of solids and their wavelength is of the order of distances between atoms in solids [96, 97]. It is possible to study single particle and collective dynamics separately depending on the scattering properties of the nuclei. In case of disordered solids the interatomic forces experienced by an atom depend on the actual local structure in its neighborhood. Because of that, the spectra measured in inelastic neutron scattering experiments on these materials can be interpreted by comparing them with the results obtained for complicated models or from computer simulations. In case of lack of computer simulation data, the results have mostly been compared with spectra of corresponding crystalline materials [96, 98]. In spite of these difficulties, neutron inelastic scattering experiments are still very important for studying the atomic dynamics of metallic glasses. The investigation of the vibrational dynamics of metallic glasses has also been conducted using neutron inelastic scattering techniques. For multi-component metallic glasses, inelastic neutron scattering has been applied to study their magnetic properties [96, 99–102]. In case of oxide glasses, **Raman and Brillouin spectroscopy** are used to study the structure and vibrational properties. The application of these techniques revealed for instance stretching modes of Si-O-Si angle involving the motion of oxygen atoms in

silica glasses [103, 104].

Knowledge of atomic diffusion is a fundamental issue in stability of materials. Alas, direct studies of the elementary diffusion events are difficult and limited [105]. The dynamical behaviour of single atoms as a function of their neighborhood can be investigated by monitoring the spatial and temporal variations of the scattered coherent X-ray intensity [105, 106]. This nanometer-scale dynamics of atoms can be followed using **X-ray photon correlation spectroscopy (XPCS)** technique. XPCS is a technique that studies the slow dynamics of various equilibrium and non-equilibrium processes occurring in condensed matter systems. It is based on the generation of a speckle pattern by the scattered coherent light originating from a material where some spatial inhomogeneities are present [107]. A speckle pattern is a diffraction limited structure factor, and is typically observed when laser light is reflected from a rough surface [107, 108]. If the state of disorder of the system changes with time, the speckle pattern will change, thus by studying the time dependence of the scattered intensity at a fixed wavevector, the dynamics of materials in thermodynamic equilibrium or out of equilibrium can be probed [107].

Glasses are considered as liquids being trapped in a metastable state from which they evolve towards the equilibrium state and this process is referred to as ageing [106, 109]. A full understanding of ageing requires a detailed description of the particle-level dynamics and structural relaxation time. XPCS technique has been widely used to collect information on the connection between ageing and the underlying microscopic dynamics [106]. The age dependence of the dynamics is directly captured by XPCS through the analysis of the two-time correlation function. It has been recently shown that the structural relaxation times for metallic glasses grow exponentially with the sample age [110].

Finishing this brief review, I would like to mention methods used to address questions concerning the electronic structure of metallic glasses. Energy measurements of electrons emitted from a sample by the photoelectric effect in order to determine the binding energies of electrons are carried out using **photoemission spectroscopy (PES)** techniques [111, 112]. Depending on the ionization energy origin one can name two techniques within PES: **X-ray photoelectron spectroscopy (XPS)**, where the energy is provided by X-ray photons, and **ultraviolet photoelectron spectroscopy (UPS)**, where ejection of electrons occurs with the participation of ultraviolet photons [112].

Photoelectron spectroscopy has been performed on metallic glasses for more than 30 years and a variety of amorphous alloys were investigated [113]. Ultraviolet photoelectron spectroscopy allows the researchers to study the occupied electron states of the valence bands (especially when characterizing surface properties), whereas XPS provides information on the energy of inner shells of electrons [112, 113].

Techniques for determining atomic arrangements like extended x-ray absorption fine structure (EXAFS) usually give only the pair-correlation functions of the system. To study many-body correlations in disordered solids, **x-ray absorption spectroscopy is used (XAS)** [114]. XAS is a widely used technique for determining the local geometric or electronic structure of matter (it probes the unoccupied density of electronic states of a sample) [114, 115]. Photons are absorbed by valence electrons which are then promoted to higher and unoccupied energy levels. XAS measurements can distinguish between the different binding energies of specific elements, as well as different bonding sites for the same element [116].

A complementary technique that has been applied to probe the occupied density of electronic states of amorphous alloys is **x-ray emission spectroscopy (XES)**, which is also element-specific and site-specific [116].

Even though this brief review of contemporary experimental methods is obviously not complete, it outlines the major techniques and proves their importance in the process of studying amorphous materials and development of physics in general. All the methods described in the present section are listed in Table 1.1.

Robert Andrews Millikan once said that science walks forward on two feet - theory and experiment and it is necessary to take into account these two standpoints when doing research. One can say that with the invention of the computer a third pillar has been set, namely computational physics. Computers paved their way through to experiments and data processing as well as to simulations of processes responsible for various phenomena. Thanks to computers, the experimental results can be monitored "on the fly", which lets the conditions of an experiment to be adjusted accordingly if necessary. The most outstanding advantage of computer simulations is that they are able to investigate any systems at the atomic resolution in three dimensions. But despite their importance in science, computer simulations cannot be overestimated and the conclusive role belongs to experimental physics.

TABLE 1.1: Experimental methods used to investigate structural properties of glasses.

Method family	Methods and techniques	Applications in glasses
Transmission Electron Microscopy	<p>Nanobeam Electron Diffraction (NBED)</p> <p>Selected Area Electron Diffraction (SAED)</p> <p>High Resolution Electron Microscopy (HRTEM)</p> <p>Brigh- and dark-field Transmission Electron Microscopy</p> <p>Scanning Transmission Electron Microscopy (STEM)</p> <p>Fluctuation Electron Microscopy (FEM)</p>	<p>Determination of medium range order.</p> <p>Local atomic coordinations.</p> <p>Nanometer-scale defects.</p> <p>Structural changes in shear bands.</p> <p>Influence of oxygen impurities on the structure. Medium range order.</p> <p>Medium range order. Shear bands.</p>
Scanning Electron Microscopy		<p>Surface structures.</p> <p>Evolution of shear bands.</p>
Scanning Tunneling Microscopy (STM)		<p>Surface structure.</p> <p>Suface crystallization.</p>
Atomic Force Microscopy		<p>Surface defects and roughness. Shear bands height.</p>

X-ray scattering	<p>Small Angle X-ray Scattering (SAXS)</p> <p>Extended X-ray Absorption Fine Structure (EXAFS)</p> <p>X-ray Photon Correlation Spectroscopy (XPCS)</p> <p>Photoemission Spectroscopy (PES)</p> <p>X-ray Absorption and Emission Spectroscopy (XES and XAS)</p>	<p>Particle sizes, shapes, structural inhomogeneities.</p> <p>Interatomic distances, local atomic packing.</p> <p>Connection between ageing and microscopic dynamics.</p> <p>Surface properties, electronic structure.</p> <p>Many-body correlations, electronic structure</p>
Neutron Scattering	<p>Small Angle Neutron Scattering (SANS)</p> <p>Inelastic neutron scattering</p>	<p>Structure at a mesoscopic scale, phase transitions</p> <p>Diffusive and vibrational motion of glasses</p>
Raman and Brillouin Spectroscopy		<p>Structure and vibrational properties of oxide glasses.</p>

1.2.2 Computer simulations

Computer simulation (modeling) is the programming of a computer to imitate the dynamic behaviour of a real or hypothesized system in all pertinent respects [117]. Performing the system analyses by computer was an extension of the approach in which models of liquids or glasses involved the physical manipulation of a large number of gelatine balls representing molecules [118, 119].

The first computer simulation of a liquid was carried out in the early 1950s at the Los Alamos National Laboratories, USA, and it laid the foundations of modern Monte Carlo (MC) simulations [120]. The simulated model used hard spheres and disks, but a few years later simulations were conducted with the Lennard-Jones

potential, which enabled comparing the data derived from a model with those obtained from experiments [118, 121].

To find the dynamic properties of multiparticle systems, a technique termed molecular dynamics (MD) was used to carry out simulations on a system of hard spheres in 1957 as well as on a set of Lennard-Jones particles within the next seven years [122–124]. Since the late 1960s, computer simulations have developed rapidly and have been performed on various systems imitating either liquids or solids. They play a valuable role in providing essentially exact results for problems in statistical mechanics, which converts the detailed information from computer simulation into macroscopic terms (pressure, internal energy etc.).

The most outstanding advantage of computer simulations is that they can be conducted on an extremely wide range of systems under various conditions. It is possible for instance to simulate molecules with exactly specified sizes and shapes [125, 126], systems under negative pressures and at very high temperatures [127–130] and lots more. Thanks to simulations of supercooled water researchers have found its liquid-to-liquid transition and predicted crystalline phases of SiO_2 [131–133].

Experimental study of glasses at the atomic scale is difficult due to their disordered structure. In simulations one can obtain at any given time the complete information on the positions and velocities of all the atoms in the system, which gives the opportunity to access any observable of interest. It is therefore possible for simulations to test theoretical concepts and determine quantities that may not be easily reachable for experiments.

Depending on the purpose, computer simulations can be divided into two types. First one provides a general picture of some universal properties of glassy systems (for example the accuracy of Mode Coupling Theory predictions of the dynamics) and such simulations are usually carried out with very simple systems [134–137]. In the second type, computer simulations attempt to answer specific questions concerning a given material or a class of materials (for example the nature of the boson peak in glasses or distribution of rings in SiO_2) [138–141].

To set up a realistic simulation of a given system one needs a reliable potential at hand which would be able to give a good description of the interactions between particles. First, a reasonable potential model has to be constructed. A model that should allow some preliminary simulations to be performed. Then, the results from these simulations are used to refine the potential model in a systematic

way. Unfortunately one of the main drawbacks of computer simulations is the availability of good potentials for the materials of interest. The development of a reliable potential model involves many *ab initio* calculations in order to determine the potential energy of a configuration, which requires a substantial amount of expertise and work [142–144]. For some materials (for example SiO_2) there are many available potential models and their reliability depends on the question that one is interested in. A potential that might be appropriate to describe structural properties of the system under study may be unsuitable for describing its dynamics [144]. Ideally empirical potentials should be transferable and applicable to possibly many systems under different conditions, regardless of the quantities of interest. This implies that designing a good force field is a challenging task and it is clear that there is vast room for improvement.

According to statistical mechanics, physical quantities are represented by averages over microscopic states of the system, distributed in accord with a given statistical (thermodynamical) ensemble. The thermodynamical ensemble is a collection of microscopic states that all realize an identical macroscopic state [118]. For systems in thermodynamic equilibrium one important example is the micro-canonical ensemble, where all states have the same energy. Another example is the canonical ensemble, where the temperature is constant and the energy can be exchanged with a thermostat. In both ensembles the number of particles in the system is kept constant throughout the simulation. The ensembles that allow energy changes while maintaining the pressure and the temperature constant with constant or also changing number of particles are often applied in computer simulations as well. Statistical systems are very complex and we cannot obtain all the information to completely characterize them. Ensembles are used because one needs reference configurations and is interested in some average properties of simulated systems. These properties do not depend on every detail of each atom [118, 145].

As mentioned before, a physical quantity can be measured by Molecular Dynamics (MD) simulations. Molecular Dynamics is the most detailed molecular simulation method that computes the motions of individual molecules. In MD simulations the time evolution of a set of interacting particles (usually corresponding to atoms) is followed via the solution of Newton's equations of motion which are second-order differential equations[118]. In order to integrate these equations, the instantaneous forces acting on the particles and their initial positions and velocities must

be specified. The positions and velocities are propagated with a finite time interval using numerical integrators, for example the Verlet algorithm [118, 146]. As the particles move, their trajectories can be analysed and the averaged values of physical quantities in question are provided. To ensure the stability of the integration, the time step should be on the order of femtoseconds since this is the typical timescale of atomic vibrations.

Molecular Dynamics evolved into an important and widely used theoretical tool that allows researchers to model many different types of systems. It enables obtaining the evolution of the system with temperature and pressure in case of equilibrium phenomena and the evolution of the system with time in the case where the system is reacting to a specific disturbance during the simulation [147]. MD simulations can also produce a wealth of information on the structure of the system under study. Even though at finite temperatures the atoms will never be at rest, the system will have a definite structure. The atomic density of the disordered or crystalline systems at each point in space will increase at the average positions of the atoms, and will fall to low values (close to zero) in the regions that will not be visited frequently by the atoms. Quantifying this information with the radial distribution function and the bond-angle distribution function leads to obtaining the characterization of the short range order in amorphous materials [148].

The power of MD simulation is that it also provides information on the dynamics of the system, not just the structure. The dynamics of a system can be looked at from many angles, but the most frequent kind of dynamical analysis is related to diffusive motion. In order to gain knowledge about how much each atom of the system moved from its initial position in a given time, one can calculate the mean squared displacement (MSD). MSD enables to find the diffusion constant for the system and if there is more than one species of atoms in the simulated configuration, the diffusion constant for each species can be computed. In simulation of solids, studies of fluctuations through time correlation functions give detailed information on the time scales of dynamic processes. For example, the vibrational density of states can be obtained from the Fourier transform of the velocity autocorrelation function [147, 148].

Thermodynamic and structural equilibrium properties are static averages independent of the dynamics of the system and they can be obtained by any correct and efficient sampling method. One of such methods to sample the infinite number of available configurations of a material, developed even before Molecular Dynamics

is the widely used Monte Carlo (MC) technique [118, 146, 147]. In MD simulations the successive configurations of the system are connected in time. In case of MC, each configuration depends only on the previously visited configuration. The MC technique generates configurations in a random manner and uses a special set of criteria to decide if the new configuration visited by the system can be accepted or not (Metropolis algorithm). Such new configuration can be obtained for example by moving randomly an atom or a molecule (or several atoms or molecules). The energy of the new configuration is computed using the potential energy function. According to Metropolis algorithm, if the energy of the new configuration is lower than the energy of the configuration it originated from, the configuration is accepted. If the energy is higher, then the Boltzmann factor of the energy difference is calculated. Also a random number between 0 and 1 is generated and compared with the Boltzmann factor. If the number is higher than this factor, then the new configuration is rejected and the previous one is used for the next iteration. If the random number is lower, the new configuration becomes the next state of the simulated system [118]. In the 1960s researchers began to develop a Monte Carlo algorithm for evolving systems dynamically from state to state and since the 1990s this approach is termed *kinetic Monte Carlo (KMC)*. The popularity and range of applications of KMC has continued to grow and it is now a common tool for studying materials. An appealing property of KMC is that it can give the exact dynamical evolution of a system. [149].

The choice between Monte Carlo and molecular dynamics is largely determined by the phenomenon under investigation. There are cases when MD simulations are not efficient enough, particularly when sampling configurations that evolve at an extremely slow rate [147]. The advantage of the MC method is its generality and a relatively weak dependence on the dimensionality of the system. The disadvantage is that it is mostly efficient on rigid structures. MC can also be used as a global optimization method to look for a global minimum of the potential energy [146] and for simulations with varying particle numbers by adding moves for the creation and destruction of particles. [150].

Despite all advantages of computer simulations there are drawbacks. Apart from difficulties with building a reliable potential model, the most severe problem in simulations is the problem of time scales. One of the reasons why the time scale that can be covered is limited is related to the timestep, which determines the computational cost involved in calculating the energy and forces necessary to perform MD simulations. Depending on the system, MD may be limited to time scales

ranging from a few picoseconds to typically a few tens of nanoseconds [12, 148]. This is a consequence of the timestep which is usually set to $10^{-15}s$. If, for example, a simulation runs for 10^9 MD steps, the time scale accessible for this simulation is $t = 10^{-15} \cdot 10^9 = 10^{-6}s$. Even systems containing few thousands of particles, such MD simulation would take weeks. As for further consequences, simulated glasses are far less relaxed than experimental glasses because of the cooling rates reachable in simulations. For the system at the temperature initially set to 10^4K , that is quenched within 10^9 MD steps, the cooling rate is $\dot{T} = 10^4K/(10^{-15}s \cdot 10^9) = 10^{10}K/s$ (typically $\dot{T} = 10^{12}K/s$), which is enormously high compared to experimental cooling rates (below $0.1K/s$) [151]. When simulating the deformation of glasses using MD, one wishes to reach a strain of order 1 in the time scale of the simulation. The time scale limitation causes that the strain rate available in simulations is $\dot{\epsilon} = 1/(10^{-15}s \cdot 10^9) = 10^6s^{-1}$ (typically on the order of 10^8s^{-1}), whereas the experimental values are 11-12 orders of magnitude lower [12].

To overcome these limitations kinetic Monte Carlo can be used. It exploits the fact that the long-time dynamics of the system typically consists of diffusive jumps from state to state. Rather than following the trajectory through every vibrational period, these state-to-state transitions are treated directly [149]. Alas, the KMC algorithm relies upon a fixed database of possible transitions that are used to update the position of each atom at each time step in the simulation. Building such exhaustive database of transitions in case of glasses is difficult, because glassy systems rarely return to previous configurations. Other techniques allowing to access larger time scales, such as temperature-accelerated dynamics or parallel replica dynamics [152], have also been developed. But even massively parallel simulations can reach time scales only of the order of microseconds [153].

Even this time scale is too short to simulate the slow thermally-activated events that control the structural relaxation and deformation of glasses at low temperatures [154, 155]. It was shown that the dynamics of the system becomes dominated by thermally activated transitions between local equilibrium configurations when the temperature decreases below the mode coupling temperature [156]. In this regime, MD simulations become inefficient because the waiting time between transitions increases exponentially with decreasing temperature and rapidly exceeds the MD time scale. An alternative approach, applied for the purpose of this thesis, is to use the transition state theory (TST), which will be described in detail in the next chapter. To identify the transitions mentioned above, the concept based on

an exploration of the potential energy landscape is employed.

1.3 Potential Energy Landscape

An atomic configuration is represented in configuration space by a $3N$ -dimensional vector consisting of the coordinates of N particles in 3 dimensions. The potential energy of the system, a function of these coordinates, defines a $3N$ -dimensional surface in the $(3N + 1)$ -dimensional space composed of configuration space and the energy axis. This surface is often referred to as the *potential energy landscape* (PEL) [12, 157]. PEL depends only on the interatomic potential and boundary conditions and therefore all configurations of the system, whether they are crystalline, amorphous or liquid, share the same PEL for given potential and boundary conditions [12].

Though it is not possible to visualize the PEL directly, Fig. 1.13 shows some of its structural features. As sketched in these figures in two and three dimensions, the potential energy landscape consists of extrema, or *stationary points*. Within the stationary points local maxima, local minima, called *inherent structures* (IS) [158] and saddle points (activated states) can be listed. In the right picture of Fig. 1.13 two inherent structures are denoted as IS^1 and IS^2 and the saddle point as A.

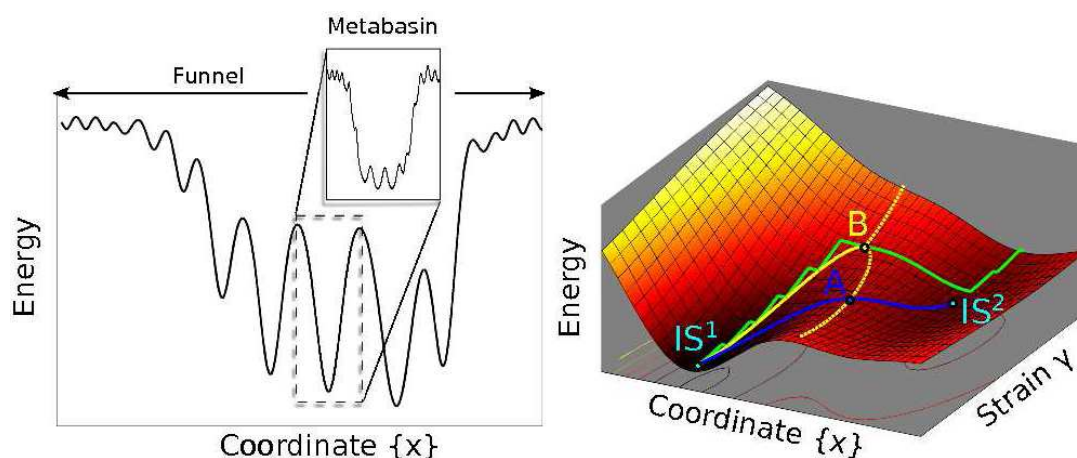


FIGURE 1.13: Schematic illustration of potential energy landscape in two (left) and three dimensions (right) [12].

Stationary points correspond to the condition where the slope of the PEL is zero:

$$\frac{\partial V(\mathbf{r}^N)}{\partial x_i} = 0 \quad \frac{\partial V(\mathbf{r}^N)}{\partial y_i} = 0 \quad \frac{\partial V(\mathbf{r}^N)}{\partial z_i} = 0 \quad i = 1, 2, \dots, N,$$

where $V(\mathbf{r}^N)$ is the potential energy of the atomic configuration and \mathbf{r}^N its position vector. These equations imply that the net force acting on each particle is zero:

$$\mathbf{f}_i = 0 \quad i = 1, 2, \dots, N$$

To distinguish potential energy minima from saddle points the Hessian matrix is computed at the stationary point, which allows to classify the extrema of the PEL by the number of negative eigenvalues of the dynamical matrix [12]. The Hessian matrix of a minimum has no negative eigenvalues, one negative eigenvalue denotes an activated state - 1st order saddle point, more than one negative eigenvalues characterize saddle points of higher order. For minima, all curvatures surrounding the stationary point are positive. That is, any movement away from this point increases the potential energy. For activated states, one can move in one (1st order saddle points) or more (higher order saddle points) directions around a stationary point and experience a decrease in potential energy.

The PEL of a disordered system contains numerous stationary points. Their number increases roughly exponentially with the number of atoms in the system [159, 160]. It is extraordinarily difficult to search exhaustively for all of the minima and activated states for systems containing more than 32 atoms, since their number is so great [161, 162]. Fortunately, statistical information, such as the distribution of activation energies, can be computed accurately on samples containing a few thousand transitions [163].

The potential energy landscape can be divided into valleys, or *basins*, that surround each local minimum [158, 164] (see Fig. 1.13). The basin (of attraction) of an inherent structure is the region of configuration space where all configurations converge to the IS upon the steepest descent energy minimization [12, 13]. In the right picture of Fig. 1.13 the basins denoted as IS^1 and IS^2 are delimited by the yellow dashed line.

The steepest descent energy minimization method within the basin of a minimum starts its search in the direction of the steepest slope. A steepest descent protocol leading to the minimum can be defined as:

$$\frac{d\mathbf{r}^N}{ds} = -\nabla V(\mathbf{r}^N) = \mathbf{f}^N(\mathbf{r}^N) \quad (\lim s \rightarrow \infty), \quad (1.1)$$

where s is a time-like variable [13]. The solution to this first order differential equation in the limit that $s \rightarrow \infty$ is the set of coordinates at a minimum \mathbf{r}_{min}^N .

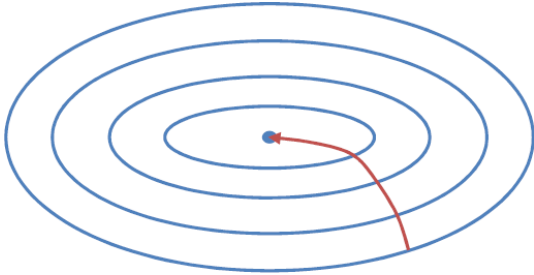


FIGURE 1.14: Local energy minimum located with steepest descent energy minimization [13].

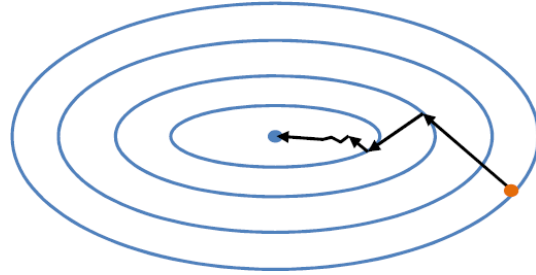


FIGURE 1.15: Local energy minimum located with conjugate gradient method [13].

A two-dimensional contour plot of energies (as a function of coordinates) shown in Fig. 1.14 pictures the steepest descent minimization path. The steepest descent method is equivalent to an instantaneous quench of a system to absolute zero - we continuously remove energy from the system until we cannot remove anymore [13].

It is very inefficient to use the Eq. 1.1 because the closer the minimum, the slower the convergence due to the fact that the forces grow increasingly small. More efficient methods to search for a local minimum are available. The overall approach they use is to find a minimum along one particular direction in configuration space. One of the most popular methods, especially effective in case of long, narrow basins in the PEL is conjugate gradient (CG) method [13]. It also uses the gradient of the potential energy surface, but chooses search directions that are perpendicular (conjugate) to previous gradients found (see Fig. 1.15). The approach used in our work includes inertia in the steepest descent energy minimization method and can be defined as:

$$m \frac{d^2 \mathbf{r}^N}{ds^2} = \mathbf{f}^N(\mathbf{r}^N) + friction \quad (\lim s \rightarrow \infty) \quad (1.2)$$

The *friction* is set to zero if the product $\frac{d\mathbf{r}^N}{ds} \cdot \mathbf{f}^N > 0$ and to infinity when negative. With this approach, called "quenched dynamics", the convergence doesn't slow down close to the minimum. The minimization proceeds until the force decreases below a required threshold. In case of overshooting the minimum, the velocities are set to zero (the friction is infinitely large) and the procedure continues towards the minimum.

Several methods have also been proposed to identify saddle points on the potential energy landscape, including excitation methods [165, 166], basin-filling methods [16, 167] and eigenvector-following methods [168–170]. As said before, an exhaustive search is unfeasible because of the exponential number of saddle points. It is possible however to determine enough saddles to compute relevant distribution functions. The search methods used for the purpose of this thesis will be described in detail in the second chapter.

Potential energy landscape relation to the complex dynamics observed in glass-forming liquids has become an appealing approach to understand the processes occurring in such systems. This approach can be pursued by means of Molecular Dynamics simulations where the succession of inherent structures visited by the system during the simulation is generated by regular energy minimizations [158, 171, 172]. Fig. 1.16 depicts examples of atomic configurations quenched at different rates using Wahnström parametrization of Lennard-Jones potential (described in Chapter 2) [173].

The dynamics of the glass formers can be divided into three temperature dependent regimes [171]. At the atomic scale the role of reference temperature is played by the mode coupling temperature (T_c), predicted by the mode coupling theory (MCT) [174]. MCT gives a good kinetic description of glassy dynamics and in its ideal version, T_c corresponds to the temperature at which the system undergoes a structural arrest [171, 175].

At high temperatures, above about $1.5T_c$ the system is fully liquid and has sufficient kinetic energy to sample the entire energy landscape. In this free diffusion regime the system hardly feels the underlying potential energy landscape and the overwhelming number of sampled energy minima are shallow [12, 176].

Between $1.5T_c$ and T_c , the system is supercooled and the dynamics becomes *landscape influenced*. The activation energy increases upon cooling (the liquid gets progressively trapped in basins of decreasing energy) and the system remains for longer periods of time in a given inherent structure before jumping to the next

basin due to thermal activation. In the landscape influenced regime, a decoupling develops between the motion of the supercooled liquid inside a basin and the infrequent transitions to an adjacent energy minima [177] and the system spends most of its time in the basins of attraction of saddle points (stationary points with index 1 and above [178, 179]).

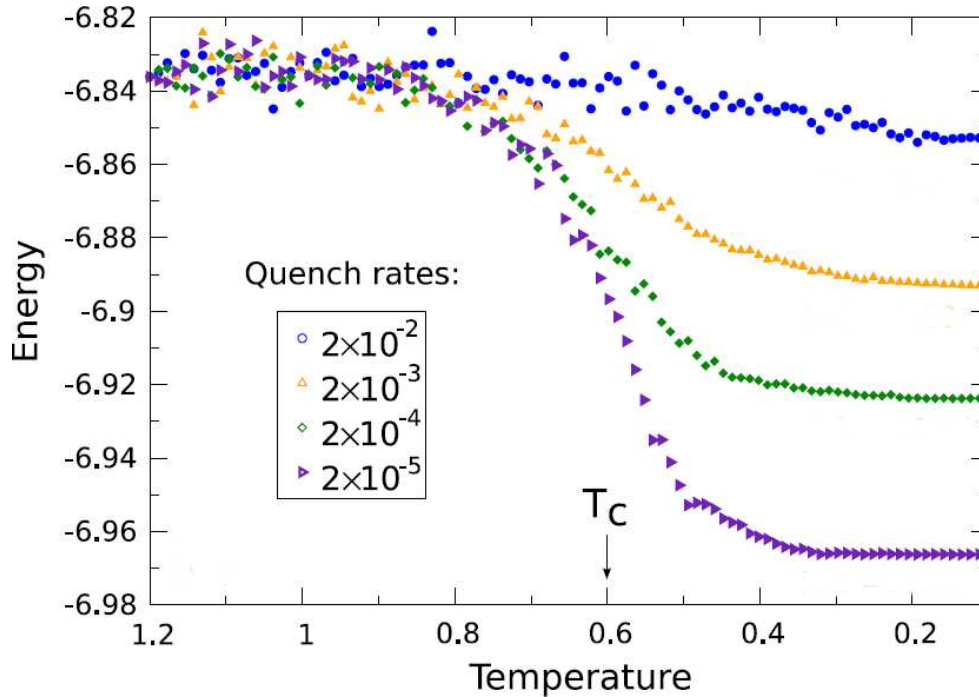


FIGURE 1.16: Inherent structure energy per particle during quenches at different rates [12].

The fact that the system gets progressively trapped is consistent with the multifunnel structure of the PEL, as demonstrated in the left picture of Fig. 1.13 [180]. The basins are organized in pockets of inherent structures with increasing energy barriers for decreasing IS energy [12]. Funnels have a hierarchical structure. The system's dynamics on short timescales can be seen as a back and forth motion within the cluster of basins, called a *metabasin* [12, 164]. On longer timescales, the system performs an irreversible Brownian diffusion between metabasins [12, 181–184]. Such dynamics suggests that metabasins are composed of basins connected by low-energy saddle points, whereas different metabasins are separated by higher energy barriers (see the magnified area in the left graph of Fig. 1.13). During the evolution, the system visits numerous metabasins, some of them are long-lived

and some are visited very quickly [185]. Therefore, the overall structure of the potential energy landscape can be thought of as a multifunnel landscape with a hierarchy of energy barriers connecting basins and metabasins [12, 180].

Below T_c , the system enters the true thermally-activated regime. This is the *landscape dominated regime*, where the system spends most time vibrating near local minima, rarely experiencing thermally-activated transitions between inherent structures. It is important to point out that the energy of the final inherent structure decreases with decreasing quench rate, as shown in Fig. 1.16. The quench rate informs how fast the initial atomic configuration was cooled down and how much time was given to the system to explore regions of the funnel before being trapped. The lower the quench rate, the better relaxed the glassy state. When the temperature is lowered below T_c , the waiting time between transitions increases rapidly, exceeding Molecular Dynamics timescales (as outlined in the previous section of this chapter) and the PEL cannot be probed by direct MD simulations [12]. As mentioned before, the alternative methods to identify activated states on the potential energy landscape will be discussed in the next chapter.

Glasses are materials that are continuously evolving towards thermal equilibrium. Even at low temperatures, they keep exploring deeper regions of the PEL and this slow process is referred to as structural relaxation or physical ageing [186]. In relation with the picture of the PEL, two relaxation timescales were identified, β -relaxation on short timescales and α -relaxation on longer timescales [12, 187]. β -relaxations are transitions inside a given metabasin and correspond to small rearrangements of atoms inside their shell of nearest neighbors (cage effect) [12, 164, 188], while α -relaxations consist of several (5 to 10) transitions between metabasins and involve bonds breaking [12, 189]. These crossings between metabasins turn out to be close to a simple random walk in configuration space [190]. This simplification allows to characterize the dynamics of supercooled liquids. Using metabasins it is also possible to relate the energy to the mobility (i.e. establish a quantitative relation between thermodynamics and dynamics) and characterize the properties of systems as different as binary Lennard-Jones glasses and silica glasses [190]. In general, the PEL approach is very versatile to elucidate basic mechanisms of the thermodynamics and dynamics of supercooled liquids and will definitely answer many questions concerning processes occurring in glasses.

The goal of this chapter was to give a short introduction to the broad field of amorphous systems and outline major methods, both experimental and numerical, used to describe their structural and dynamic properties. The next chapter will consist of a detailed characterization of the systems studied for the purpose of this thesis, including a thorough description of applied potentials, theoretical basis to study infrequent, thermally-activated processes and an insightful look into methods enabling an efficient exploration of the potential energy landscape.

POTENTIALS AND METHODS

2.1 Interatomic potentials

The potential energy depends on the atomic configuration. It can therefore be divided into terms depending on the coordinates of individual atoms, pairs, triplets etc. For a system containing N atoms:

$$V(\mathbf{r}_1, \dots, \mathbf{r}_N) = \sum_i v_1(\mathbf{r}_i) + \sum_{i < j} v_2(\mathbf{r}_i, \mathbf{r}_j) + \sum_{i < j < k} v_3(\mathbf{r}_i, \mathbf{r}_j, \mathbf{r}_k) + \dots \quad (2.1)$$

The term $v_1(\mathbf{r}_i)$ represents the effect of an external field on the system. The other terms represent interactions between pairs of particles. The pair potential, v_2 is the most important and depends only on the magnitude of the pair separation and can be written $v_2(r_{ij})$. The v_3 term, involving triplets of particles, also contains information about the angle between the bonds ji and jk . Four-body and higher terms are expected to be small in comparison with v_2 and v_3 since they describe torsional angles, the angular springs between the osculating planes formed by the first three and last three atoms of a consecutively bonded quadruple of atoms. Because of the time consumption of the calculations involving a sum over triplets or more particles, the terms beyond the pair potential are frequently not included. Fortunately, the pairwise approximation gives a good description of system properties because the average three-body effects can be partially included by defining an "effective" pair potential [118]. In case of charged species, Coulombic terms would be present in Eq. 2.1. For example the ionic character of the bond in silica

glasses is usually described through a two-body potential and this is enough to characterize the tetrahedral structure of SiO_2 [12].

In the field of computer simulations of liquids and glasses, given the complexity of processes, a qualitative understanding is of interest and in this context simple, phenomenological potentials are applied. Most of the works employ a binary Lennard-Jones (LJ) potential, which provides a reasonable description of the properties of noble gases. It is expressed as:

$$v_2(r_{ij}) = 4\epsilon_{ij} \left[\left(\frac{\sigma_{ij}}{r_{ij}} \right)^{12} - \left(\frac{\sigma_{ij}}{r_{ij}} \right)^6 \right] \quad (2.2)$$

At large separations this potential has an attractive tail of the form $-1/r^6$, basically due to correlation between the electron clouds surrounding the atoms (van der Waals interactions) and a steeply rising repulsive part at distances less than $r \sim \sigma$ (as a result of Pauli's exclusion principle, which comes into action when electronic clouds overlap). Whereas the functional form of the attractive term has a clear physical justification, the repulsive term is purely phenomenological (there is no theory that describes a repulsion due to Pauli's principle) and in this form it is easy to compute since r_{ij}^{12} is the square of r_{ij}^6 . The parameters of the Lennard-Jones potential differ depending on the model used. For the purpose of this thesis two widely used binary LJ potentials have been applied, first developed by Wahnström [173] and by Kob and Andersen [191]. They were employed in two generic systems that meant to model metallic glasses. Apart from these, a more specific system, amorphous silica, using another type of pair potential (the BKS potential) has been investigated [192].

2.1.1 Wahnström potential

In this binary model, the two particle types are equimolar. The only differences between them are that their masses and diameters differ, $m_A/m_B = 2.0$ and $\sigma_{AA}/\sigma_{BB} = 1.2$. This potential does not represent any existing metallic glass system, but was introduced to imitate a mixture of big and small atoms. One particularity of this potential is that it is strictly additive, i.e. the cross-interaction diameter is $\sigma_{AB} = (\sigma_{AA} + \sigma_{BB})/2$. The depths of the potential wells are equal: $\epsilon_{AA} = \epsilon_{AB} = \epsilon_{BB} = 1.0$, i.e. also additive. To ensure smoothness of the second derivative at the cut-off radius, the quadratic function $B_{ij}r^2 + C_{ij}$ was added to the potential, where:

$$B_{ij} = 4\epsilon_{ij} \frac{\left[6 \left(\frac{\sigma_{ij}}{R_c^{ij}} \right)^{12} - 3 \left(\frac{\sigma_{ij}}{R_c^{ij}} \right)^6 \right]}{(R_c^{ij})^2} \quad (2.3)$$

and

$$C_{ij} = 4\epsilon_{ij} \left[-7 \left(\frac{\sigma_{ij}}{R_c^{ij}} \right)^{12} + 4 \left(\frac{\sigma_{ij}}{R_c^{ij}} \right)^6 \right] \quad (2.4)$$

The potential was usually truncated at $R_c^{ij} = 2.5\sigma_{ij}$.

Figure 2.1 presents the interactions between different types of atoms of the binary mixture used in the simulations performed for the purpose of this thesis (to be described in the next chapter).

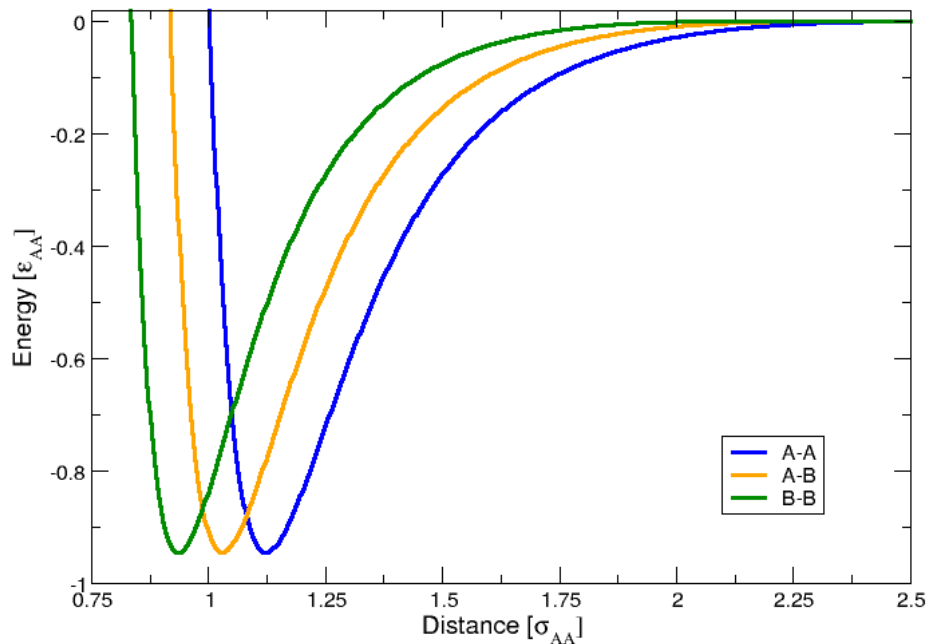


FIGURE 2.1: Interactions between different types of particles for the Wahnström potential

The distance r_{ij}^{min} , at which the potential reaches its minimum (the unshifted potential function has the value $-\epsilon_{ij}$) is related to σ_{ij} as:

$$r_{ij}^{min} = 2^{1/6} \sigma_{ij} \quad (2.5)$$

ϵ_{AA}	ϵ_{BB}	ϵ_{AB}	σ_{AA}	σ_{BB}	σ_{AB}	R_C	C_A	C_B	m_A/m_B
1	1	1	1	$\frac{5}{6}$	$\frac{11}{12}$	2.5	0.5	0.5	2.0

TABLE 2.1: Parameters of the Wahnström potential. The cut-off radius is expressed in units of the corresponding σ_{ij} . C_A and C_B are the concentrations of the two species.

The complete set of parameters used to build the Wahnström potential function is presented in Table 2.1.

Wahnström potential was employed in many studies of dynamics below the mode-coupling temperature, which for this model is equal to $T_C = 0.59\epsilon_{AA}/k_B$ [12, 140, 193–195]. Simulated systems mostly have a density of $\rho = 1.2\sigma_{AA}^{-3}$. This model is usually used to show and describe icosahedral short range order in metallic glasses as a function of, for example, level of glass relaxation [196].

2.1.2 Kob-Andersen potential

This is the most widely used potential, developed to reproduce the properties of a mixture of 80% A particles and 20% B particles. The two species have equal masses. This potential is highly non-additive, that is $\sigma_{AB} < (\sigma_{AA} + \sigma_{BB})/2$ and $\epsilon_{AB} > (\epsilon_{AA} + \epsilon_{BB})/2$. The choice of the parameters was based on the observation that for such system composition, an additive potential leads to crystallization at low temperatures. After adjusting the parameters in Lennard-Jones potential, the resulting model described the properties of amorphous $Ni_{80}P_{20}$ [191].

Figure 2.2 depicts the interactions between the two species of the binary mixture used in this study. The potential function was not shifted to go to zero at the cut-off radius as is often the case in the literature.

This is the most popular potential used in computer simulations of metallic glasses to study, for instance, the glass transition, cooling rate influence, dynamical regimes in the energy landscape or ageing [141, 171, 186, 197]. The mode-coupling temperature for this model is equal to $T_C = 0.43\epsilon_{AA}/k_B$ and the simulations mostly involve systems of density $\rho = 1.2\sigma_{AA}^{-3}$. The parameters specific for Kob-Andersen potential are summarized in the table below.

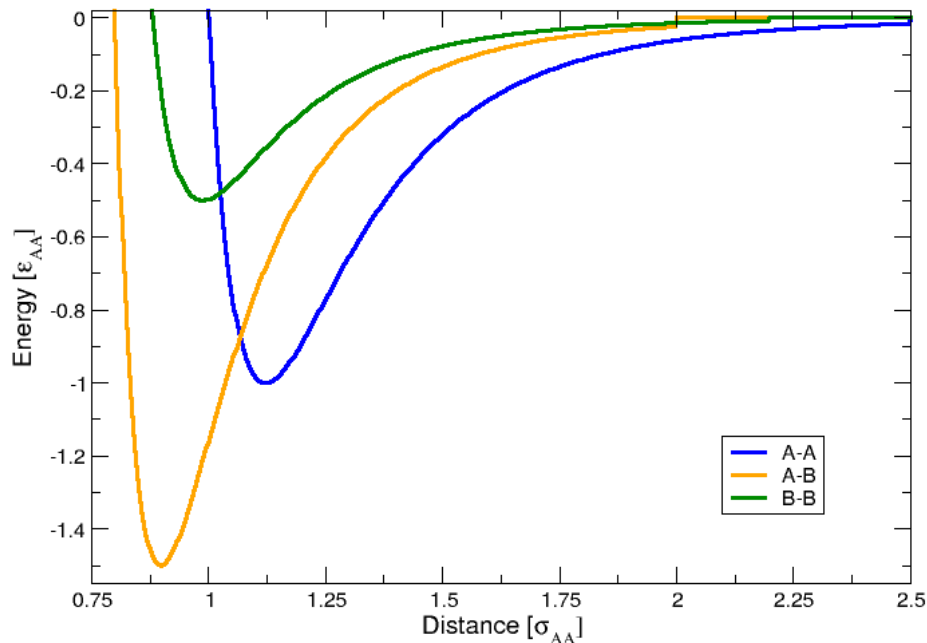


FIGURE 2.2: Interactions between different types of particles for the Kob-Andersen potential

ϵ_{AA}	ϵ_{BB}	ϵ_{AB}	σ_{AA}	σ_{BB}	σ_{AB}	R_C	C_A	C_B	m_A/m_B
1	0.5	1.5	1	0.88	0.8	2.5	0.8	0.2	1.0

TABLE 2.2: Parameters of the Kob potential. The cut-off radius is expressed in units of the corresponding σ_{ij} . C_A and C_B meaning as in Table 2.1.

2.1.3 BKS potential

The BKS pair potential [192, 198] was introduced by B.W.H. van Beest, G.J. Kramer and R.A. Santen to represent the interatomic interactions in silicates. For the purpose of this dissertation, its implementation was taken from B. Mantisi's paper (see Ref. [198]). The BKS potential is expressed as a sum of different kinds of interactions:

$$V_{BKS}(r_{ij}) = V_{Coul}(r_{ij}) + V_{Buck}(r_{ij}) \quad (2.6)$$

First term in the sum above is the Coulombic part, describing electrostatic interactions between partial charges with a $1/r$ spatial dependence. It is given by

$$V_{Coul}(r_{ij}) = \frac{q_i q_j e^2}{r_{ij}}, \quad (2.7)$$

where e is the charge of an electron and the partial charges are $q_{Si} = 2.4$ and $q_O = -1.2$. The Coulomb's constant is included in e^2 , which is finally given by $1602.19/(4\pi \cdot 8.8542) eV \text{ \AA}$.

The second part usually describes repulsion at short range and dispersion. This term can take different forms. In this study the Buckingham [199] potential was applied and is expressed as:

$$V_{Buck}(r_{ij}) = A_{ij} e^{-\frac{r_{ij}}{\rho_{ij}}} - \frac{C_{ij}}{r_{ij}^6} \quad (2.8)$$

We recognize a van der Waals attraction term as in Lennard-Jones potential and the repulsion term (still phenomenological), which is now expressed as an exponential. The parameters A_{ij} , ρ_{ij} and C_{ij} were adjusted on *ab initio* data [192].

For the sake of computational efficiency the short-range part of the potential was truncated and shifted at $R_C^{Buck} = 5.5 \text{ \AA}$. To deal with the long-range interactions the Wolf truncation method was employed [200] instead of the time-consuming Ewald summation. It considers that for a certain distance, the charges will neutralize. The cut-off radius for the Coulombic interactions was set to $R_C^{Coul} = 10.17 \text{ \AA}$.

The truncated and smoothed elements of Eq. 2.6, applied in this thesis are described as:

$$V_{Coul}(r_{ij}) = q_i q_j e^2 V_W(r_{ij}), \quad (2.9)$$

with:

$$V_W(r_{ij}) = \left(\left(\frac{1}{r_{ij}} - \frac{1}{R_C^{Coul}} \right) + \frac{1}{(R_C^{Coul})^2} (r - R_C^{Coul}) \right) \quad (2.10)$$

And for the Buckingham potential:

$$V_{Buck}(r_{ij}) = \left\{ A_{ij} e^{-\frac{r_{ij}}{\rho_{ij}}} - \frac{C_{ij}}{r_{ij}^6} - \left[A_{ij} e^{-\frac{R_C^{Buck}}{\rho_{ij}}} - \frac{C_{ij}}{(R_C^{Buck})^6} \right] \right\} \quad (2.11)$$

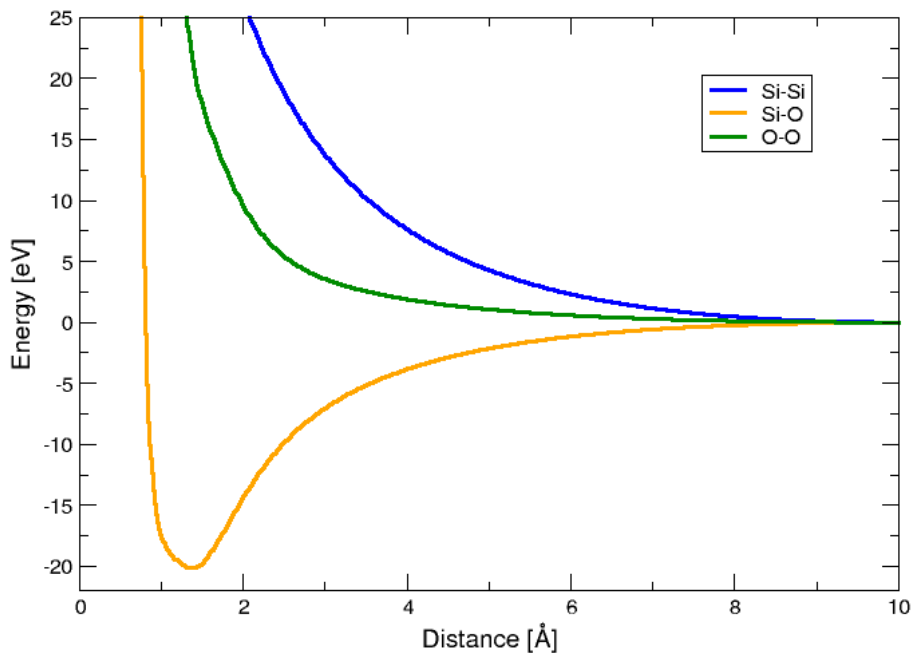


FIGURE 2.3: Interactions between different types of particles for the BKS potential

A strong and regular repulsive part at short range is added to avoid the collapse of atoms at high pressures or high temperatures (see Ref. [198]). The values of the cut-off radii for such O-O, Si-O and Si-Si interactions along with the rest of the parameters of the BKS potential used to model the silica glass for the purpose of this thesis are presented in Table 2.3. The added repulsive part has the following form:

$$V_{Rep}(r_{ij}) = \left\{ \frac{D_{ij}}{r_{ij}} \right\}^{12} + E_{ij}r_{ij} + F_{ij} \quad (2.12)$$

D_{ij} , E_{ij} and F_{ij} have been adjusted in order to have the first and second derivatives of the potential continuous. The interactions between different species are shown in Figure 2.3.

The BKS potential is non-additive. This feature, in connection with the Coulomb interactions, is sufficient to build the tetrahedral structure of SiO_2 , without introducing three-body terms.

	$A_{ij}(eV)$	$\rho_{ij}(\text{\AA})$	$C_{ij}(eV\text{\AA})$	$D_{ij}(\text{\AA}eV^{-12})$
O-O	1388.773	0.3623	175.0	1.5097531478
Si-O	18003.7572	0.2052	133.5381	1.0318846604
Si-Si	872360308.1	0.0657	23.299907	0.0
	$E_{ij}(eV\text{\AA}^{-1})$	$F_{ij}(eV)$	$R_C^{Rep}(\text{\AA})$	
O-O	-15.1217568459	39.4169471782	1.75	
Si-O	-3.5591468116	-15.4534580635	1.27	
Si-Si	0.0	0.0	0.0	

TABLE 2.3: Parameters of the BKS potential.

A small Coulomb interaction is necessary in order to stabilize this system, because of the presence of the weak attractive $O - O$ interaction in the short-range part of the BKS potential. It was shown [201], that for the oxygen charge of $1.2C$, the coordination number of Si atoms is 4 and it increases with q_O going to zero.

Thanks to the Wolf truncation, the calculations are much faster than if the full Coulombic interaction was calculated (for instance using Ewald summation [202]). Nevertheless it remains much slower than with a Lennard-Jones potential because with a cut-off radius of 10.17\AA , there are many neighbors, usually over 500, in the neighbourlists compared to a LJ potential with a cut-off at 2.5σ (around 200 neighbors).

2.1.4 Periodic boundary conditions

Computer simulations are usually performed on a small number of particles. Results presented in this dissertation have been obtained for the systems not exceeding $N = 4000$ atoms. These particles are confined in a finite simulation cell, which for geometrical simplicity has a cubic shape. A major problem arising from this kind of system representation is the large fraction of particles which appear on the cube faces. Particles on the surface will experience different forces from those in the bulk, which will make the results geometry and size dependent.

To overcome the problem of surface effects one implements *periodic boundary conditions*. The cubic box is replicated throughout space to form an infinite lattice. During the simulation, as a particle moves in the original cell, its periodic image

in each of the neighboring cells moves in exactly the same way. When a particle leaves the central box, one of its images will enter through the opposite face.

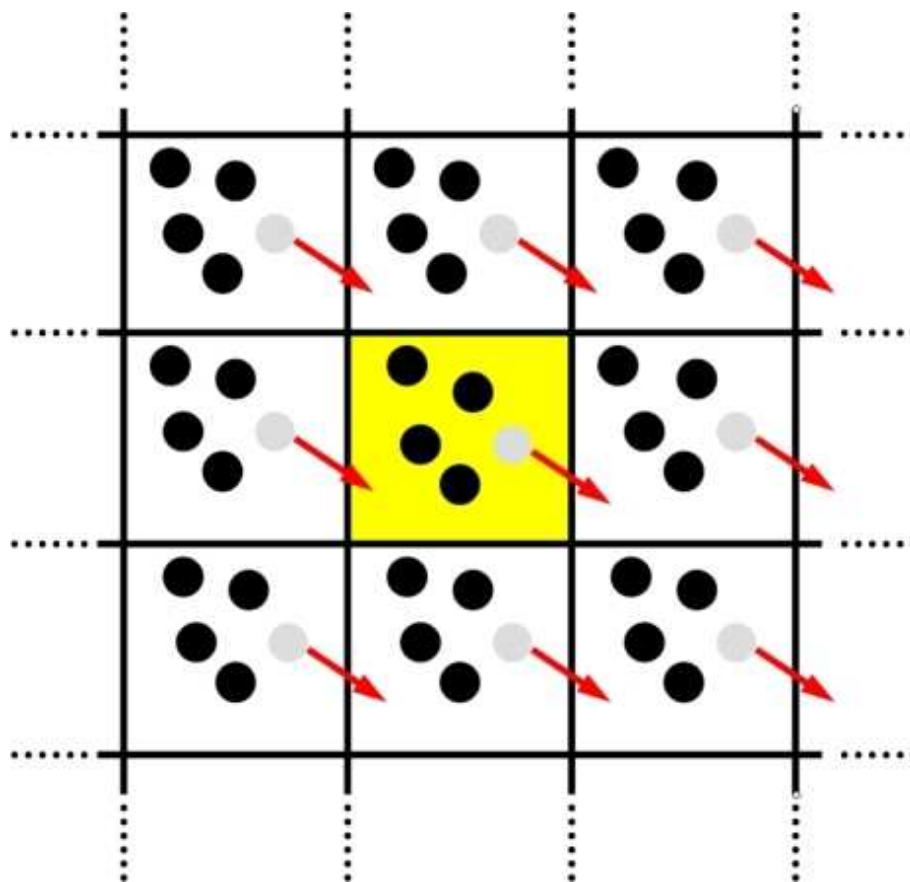


FIGURE 2.4: A two-dimensional periodic system. Figure reproduced from Ref. [14].

The concentration of particles in the central cell (and hence in the entire system) is conserved. Applying periodic boundary conditions doesn't prevent finite size effects. A two-dimensional version of such a periodic system is shown in Fig. 2.4. In a three-dimensional example, molecules would be free to cross any of the six cube faces.

2.2 Potential Energy Landscape exploration

2.2.1 Molecular Dynamics

Molecular dynamics (MD) is a very powerful method to describe the dynamics of a system of interacting atoms at finite temperature by integrating numerically Newton's equations of motion:

$$m_i \frac{\partial^2 \mathbf{r}_i}{\partial t^2} = \mathbf{F}_i(\mathbf{r}_1, \mathbf{r}_2, \dots, \mathbf{r}_N) \quad i = 1, 2, \dots, N, \quad (2.13)$$

where m_i is the mass of atom i , \mathbf{r}_i its position vector and \mathbf{F}_i the force on that atom. This force is given by the negative gradient of the potential energy V :

$$\mathbf{F}_i = -\nabla_{\mathbf{r}_i} V(\mathbf{r}_1, \mathbf{r}_2, \dots, \mathbf{r}_N) \quad i = 1, 2, \dots, N, \quad (2.14)$$

In this study, depending on the system considered, the potential energy was expressed by the formulas presented in Section 2.1. The trajectory of the system in phase space was obtained using the *velocity Verlet algorithm* [203], which at $t = 0$ needs only the positions and the velocities of the particles. After one step new positions/velocities are computed and the observables of interest can be measured. This algorithm is given by:

$$\mathbf{r}_i(t+h) = \mathbf{r}_i(t) + h\mathbf{v}_i(t) + \frac{h^2}{2} \frac{\mathbf{F}_i(t)}{m} \quad i = 1, 2, \dots, N, \quad (2.15)$$

$$\mathbf{v}_i(t+h) = \mathbf{v}_i(t) + \frac{h}{2m} [\mathbf{F}_i(t) + \mathbf{F}_i(t+h)] \quad i = 1, 2, \dots, N, \quad (2.16)$$

where h is a small time increment on the order of 10^{-15} s, which corresponds to atomic vibrations.

In MD simulations a measurable quantity A of the system under consideration is calculated as a time average of the actual values of interest $A(t)$:

$$\langle A \rangle = \lim_{\tau_{sim} \rightarrow \infty} \frac{1}{\tau_{sim}} \int_{\tau=0}^{\tau_{sim}} A(t) dt, \quad (2.17)$$

where $\langle \dots \rangle$ indicates the time average and τ_{sim} is the simulation time.

The MD simulations performed within this thesis were done in the canonical ensemble (NVT). For this ensemble the number of particles (N), volume(V) and temperature (T) are constant, and the energy of the simulated system will fluctuate. In order to keep the temperature constant a variety of thermostat methods are available. One of the popular techniques applied in this study is the Andersen thermostat [204]. This thermostat introduces a stochastic element to the temperature by having random collisions of molecules with an imaginary heat bath at the desired temperature. A random particle and a random direction are chosen

and the velocity in this direction is reset within a 1D Gaussian distribution at the desired temperature:

$$\wp(v_x) = \left(\frac{m}{2\pi k_B T} \right)^{1/2} \exp \left(-\frac{mv_x^2}{2k_B T} \right). \quad (2.18)$$

In this thesis the Andersen thermostat was applied by defining the fraction of velocities of atoms to be rescaled with a gaussian function. At each MD step a random number between 0 and 1 was generated and one direction of a given atom's velocity was reset if the generated number was smaller than the arbitrary variable. Usually, the variable value was set to 0.001 or 0.01.

In molecular simulations one is interested in configurations of minimum energy on the potential energy landscape. As pointed out in Section 1.3, various techniques can be used for the minimization. We have applied a method called quenched velocity Verlet algorithm, or more simply quenched dynamics [205]. At each time step the coordinates and velocities were updated and the product $\mathbf{v} \cdot \mathbf{f}$ was calculated. If the product, i.e. the system was moving towards a minimum, a normal velocity Verlet step was taken in order to benefit from inertia and not to suffer from the convergence slow-down typical of the steepest-descent algorithm. On the other hand, if $\mathbf{v} \cdot \mathbf{f} < 0$, i.e. the system overshoot a minimum and was moving away from it, velocities were reset to zero in order to start over a descent towards the minimum. The minimization proceeded until the force decreases below a required limit, usually $10^{-4}\epsilon_{AA}/\sigma_{AA}$ for metallic glasses and $10^{-3}eV/\text{\AA}$ in case of silica glasses.

One of the objectives of this dissertation was to investigate thermally-activated processes in glasses. These processes dominate the dynamics of the system when the temperature decreases below the mode-coupling temperature T_C . In this regime, MD simulations become inefficient because the waiting time between transitions increases exponentially with decreasing temperature and rapidly exceeds the MD time scale. In the previous chapter a few ways of dealing with the problem of MD time scales have been outlined, but for the purpose of this thesis the Transition State Theory [206] has been employed.

2.2.2 Transition State Theory

The transition State Theory (TST) is the formalism used to describe rare events, that are much slower than atomic vibrations. In the TST approximation, the classical one-way rate constant for escape from state A to some adjacent state B is taken to be the equilibrium flux through the dividing surface (transition state) between A and B (see Fig. 2.5 below) [152].

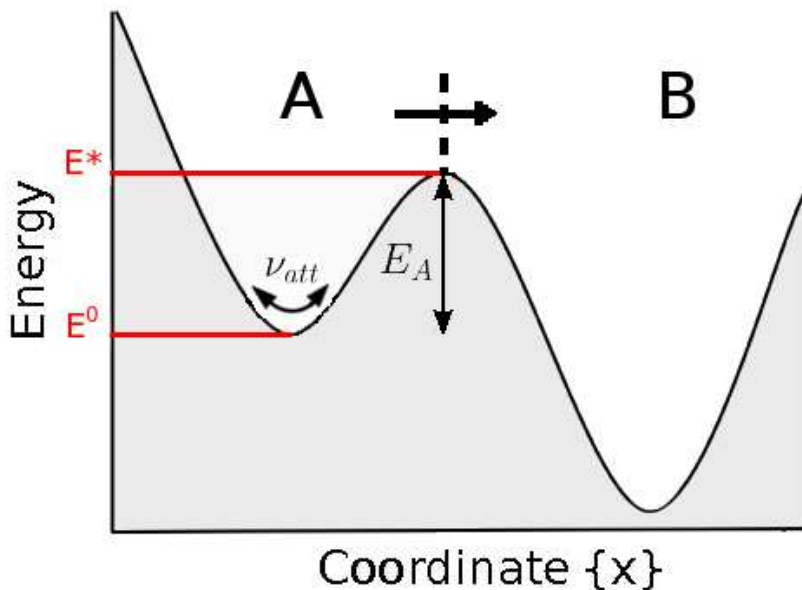


FIGURE 2.5: A two-state system illustrating the definition of the TST escape rate as the outgoing flux through the dividing surface between adjacent equilibrium states.

Since this flux is an equilibrium property of the system, there is no need to run a long classical trajectory to accurately determine the fraction of time the system spends in state A and the number of crossings through the dividing surface. The TST rate constant for escape from A is given by:

$$k_{A \rightarrow}^{TST} = \langle |dx/dt| \delta(x - q) \rangle_A \quad (2.19)$$

The angular brackets indicate the ratio of Boltzmann-weighted integrals over $6N$ -dimensional phase space (configuration space \mathbf{r} and momentum space \mathbf{p}), that is, for some property $P(\mathbf{r}, \mathbf{p})$:

$$\langle P \rangle = \frac{\int \int P(\mathbf{r}, \mathbf{p}) \exp[-H(\mathbf{r}, \mathbf{p})/k_B T] d\mathbf{r} d\mathbf{p}}{\int \int \exp[-H(\mathbf{r}, \mathbf{p})/k_B T] d\mathbf{r} d\mathbf{p}}, \quad (2.20)$$

where k_B is the Boltzmann constant and H is the Hamiltonian. The subscript A in Eq. 2.19 indicates that the configuration space integrals are restricted to the space belonging to state A and transition state (dividing surface) is at $x = q$ [152]. If the effective mass m of the reaction coordinate is constant over the dividing surface, Eq. 2.19 reduces to a simpler ensemble average over configuration space only [207]:

$$k_{A \rightarrow}^{TST} = \sqrt{2k_B T / \pi m} \langle \delta(x - q) \rangle_A \quad (2.21)$$

The essence of the expression above (and of TST), is that the Dirac delta function picks out the probability of the system being at the dividing surface, relative to everywhere it can be in state A .

Harmonic Transition State Theory

If the activated states (the minimum energy states along the dividing surface between the basins of attraction of the initial and final states) on the potential energy surface for the transition pathways have been identified, a classical harmonic approximation of the Transition State Theory (hTST) [208] can be applied. The methods used in this study to sample the Potential Energy Landscape in the search of first-order saddle points are presented in the next sections of this Chapter. Within the harmonic approximation the rate of escape given in Eq. 2.22 can be simplified and expressed as:

$$k^{hTST} = \nu_{att} \exp\left(-\frac{E^* - E^0}{k_B T}\right), \quad (2.22)$$

where $E_A = E^* - E^0$ is the activation energy, E^0 the energy of the initial state and E^* the energy of the saddle point (see Fig. 2.5). The attempt frequency is given by:

$$\nu_{att} = \frac{\prod_{i=1}^{3N-3} \nu_i^0}{\prod_{i=1}^{3N-4} \nu_i^*}, \quad (2.23)$$

where $\{\nu_i^0\}$ and $\{\nu_i^*\}$ are the real nonzero eigenfrequencies of the equilibrium and activated states, respectively, computed by diagonalizing the mass-weighted Hessian matrix of the system in both states. The scaled Hessian matrix is given by:

$$H = \frac{1}{\sqrt{m_i m_j}} \frac{\partial^2 V}{\partial r_{i,\alpha} \partial r_{j,\beta}},$$

where i and j are particle indices and α and β are the Cartesian components x , y , and z . The three degrees of translational invariance are then omitted in Eq. 2.23 if the 3D periodic boundary conditions are used and there is one less frequency in the activated state because of the imaginary frequency associated with the unstable mode.

All the methods that have been used in this thesis to identify the activated states are presented in the next three sections.

2.2.3 Activation-Relaxation Technique

The dynamics of a system can be described as a sequence of metastable states separated by energy barriers that are high compared to $k_B T$ (the typical energy scale at the atomic level). For the simplest characterization of such dynamics, it is sufficient to explore the Potential Energy Landscape through hops from one local minimum to another, with the trajectories going through first-order saddle points. The *Activation-Relaxation Technique (ART)* is a method, that provides a way identify such points. It was initially proposed by Mousseau and co-workers [209] to study diffusion processes in amorphous silicon and the structure of $Ni_{80}P_{20}$. Apart from metallic glasses, ART has been applied with success to amorphous semiconductors [12, 163, 210–214]. It is an eigenvector-following method that allows sampling of the saddle points on a potential energy surface, connected to an initial equilibrium configuration. Saddle points have zero force and a Hessian matrix with exactly one negative eigenvalue. ART only requires computation of the lowest eigenvalue and associated eigenvector of the Hessian matrix, which are determined using the Lanczos algorithm, an iterative method based only on force evaluations [210, 215]. In this study, 20 force evaluations were usually enough to extract the very lowest eigenvalue and its eigenvector.

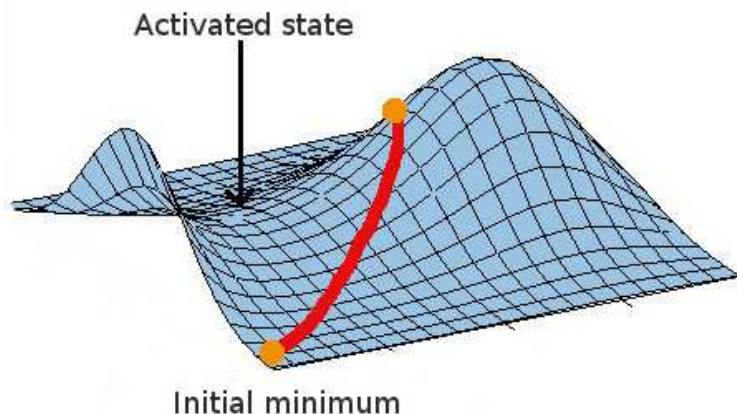


FIGURE 2.6: Pushing the system along a random direction until a negative eigenvalue appears.

ART steps

ART is an iterative method. The calculation starts from an initial equilibrium configuration \mathbf{x}_0 . An initial direction in phase space, \mathbf{T}_0 , is chosen at random. ART is then composed of three stages. In the first stage, the destabilization phase, the system is moved away from the initial minimum along \mathbf{T}_0 using a step of fixed length, α_0 :

$$\mathbf{x}'_{n+1} = \mathbf{x}_n + \alpha_0 \mathbf{T}_0 \quad (2.24)$$

The configuration \mathbf{x}'_{n+1} is then partially relaxed perpendicularly to \mathbf{T}_0 using quenched dynamics. The relaxation leads to the configuration \mathbf{x}_{n+1} . The minimum eigenvalue of the Hessian matrix and corresponding eigenvector are then computed using the Lanczos algorithm. This procedure is repeated along \mathbf{T}_0 until the minimum eigenvalue is smaller than a set negative value to avoid falling back in the initial basin of attraction and can be pictured as the red path in the Fig. 2.6. The algorithm then enters its second phase, the convergence phase, during which the system is pushed towards a saddle point along the eigenvector corresponding to the negative eigenvalue. This stage is very challenging numerically and the step size is smaller because the system is higher in energy when it enters the convergence phase and thus has to go down a ridge as it converges to the saddle with the risk of losing the ridge, which results in falling back into the basin of attraction of \mathbf{x}_0 (the curvature becomes positive again). If this happens, the procedure is stopped and another search is started from the same initial configuration.

Once a saddle point is found (the maximum atomic force component becomes less

than a set threshold), its activation energy is given by the difference in internal potential energy between initial and activated states. ART then enters the third phase, the relaxation phase. The system is perturbed towards \mathbf{x}_0 and relaxed to check if the saddle point is connected with \mathbf{x}_0 . If not, the saddle point is rejected and a new search is started. If the saddle is connected, the system is perturbed away from \mathbf{x}_0 and relaxed in order to determine the final configuration and obtain the full transition path.

Parameter	Definition	Value
N_P	Number of perpendicular relaxation steps after moving a system along \mathbf{T}_0 .	5
N_L	Number of Lanczos force evaluations in order to find the lowest eigenvalue and corresponding eigenvector.	20
α^0	Step size to move the system along \mathbf{T}_0 .	0.125
α^1	Step size to converge to a saddle.	0.025
C_{max}	Minimum (negative) eigenvalue, below which convergence to a saddle begins	-3.0
X_{range}	Cut-off distance to construct \mathbf{T}_0 . It controls the number of atoms to be displaced at each step.	$1.0(MG)/4.0(SiO_2)$
ΔE_{max}	Maximum relative energy decrease during perpendicular relaxation	0.1
D_{max}	Threshold distance in configuration space to declare two configurations equal.	0.5

TABLE 2.4: Parameters used to search for saddle points with ART.

In order to run an ART attempt, a set of parameters controlling the stages described above is defined. They are listed in Table 2.4. Their values are expressed in reduced units for metallic and in real units for silica glasses. These values of ART parameters allowed to reach the highest acceptance rate for both simulated types of glasses.

During the process of optimizing ART, the parameters from Table 2.4 were adjusted to provide maximum number of found saddle points within minimum number of iterations. Small step size α^0 increased the total time of each iteration, whereas α^0 bigger than 0.125 increased the number of failed searches (the curvature became positive again during the convergence phase much more often). Changes in α^1 decreased the efficiency (the ridge along which the system converged to a saddle was lost more often) when it was bigger than the value presented in Table 2.4. C_{max} was changed between -5.0 and -2.0 , but with no significant influence on the acceptance rate. The X_{range} parameter determines how many atoms are displaced at each step α^0 along \mathbf{T}_0 . In case of metallic glasses usually one atom was moved (ART was then most efficient), but for SiO_2 it turned out that when the system was moved out of the initial equilibrium by displacing a single Si atom, the attempts to reach a saddle point were unsuccessful. Therefore the value of X_{range} had to be increased (\mathbf{T}_0 contained 5-6 atoms). Other parameters from Table 2.4, namely ΔE_{max} and D_{max} have not been changed during the ART optimization.

In every iteration the most time consuming are force evaluations. For each search that led or not to a saddle point, the number of force calls varied from 200 up to 500 in case of silica glasses.

For disordered solids, an exhaustive search is unfeasible because of the exponential number of saddle points. Besides, only around 25% of searches resulted in reaching saddle points connected to the initial minimum. However, it has been shown that ART can identify enough saddles to build statistically relevant samples, from which stationary distributions can be computed [210]. The most important upside of this method is that it doesn't require final states to find saddle points. This is not the case for other methods presented later in this chapter. Even though the acceptance rate on the order of 25% may not be satisfying, it is not much different from efficiencies of other methods used for the purpose of this dissertation. Identifying 1000 distinct saddle points with ART is faster than with other techniques used here. As will be shown in the next chapter, a direct MD trajectory was found to visit saddle points on the potential energy surface that all lie within the range sampled by the ART calculation. Nevertheless, the density of low energy saddle points is very low and ART is biased towards saddles of high energy compared to those visited in the actual dynamics.

The efficiency of ART became less important when it was implemented to work

within OpenMP parallel computing method. Dividing most time consuming operations in each search among many threads allowed to perform more ART attempts and find more than 1000 distinct saddle points for 4000-atom metallic glass system and 3000-atom silica glass system in less than 72 hours.

2.2.4 Nudged Elastic Band

The *Nudged Elastic Band (NEB)* method is a chain-of-states approach for finding the minimum energy path (MEP) on the potential energy landscape. In configuration space, each point on this path represents one configuration of atoms in the system. The MEP is the lowest energy path for a rearrangement of a group of atoms from one stable configuration to another, that is, from one local energy minimum to another. The potential energy maximum along the MEP is the saddle-point energy which gives the activation energy barrier [216].

NEB has become widely used for estimating transition rates within the hTST approximation. The MEP is found by constructing a set of images of the system, typically on the order of 10–30, between the initial and final state. These images can be generated by linear interpolation between the two end states. A spring interaction between adjacent images is added to ensure continuity of the path, thus mimicking an elastic band made up of beads and springs. An optimization of the band, involving the minimization of the force acting on the images, brings the band to the MEP.

An essential feature of the NEB method is a force projection which ensures that the spring forces do not interfere with the convergence of the elastic band to the MEP, as well as ensuring that the true force does not affect the distribution of images along the MEP. It is necessary to estimate the tangent to the path at each image and every iteration during the minimization, in order to decompose the true force and the spring force into components parallel and perpendicular to the path. Only the perpendicular component of the true force is included, and only the parallel component of the spring force. This force projection is referred to as "nudging" [15, 216].

The spring forces then only control the spacing of the images along the band. When this projection scheme is not used, the spring forces tend to prevent the band from following the MEP and the true force along the path causes the images to slide away from the high energy regions towards the minima, reducing the density of

images where they are most needed [15]. In the NEB method the strength of the spring forces can be varied by several orders of magnitude without affecting the equilibrium position of the band. The illustration of NEB method showing an elastic band before and after relaxation is presented in Fig. 2.7.

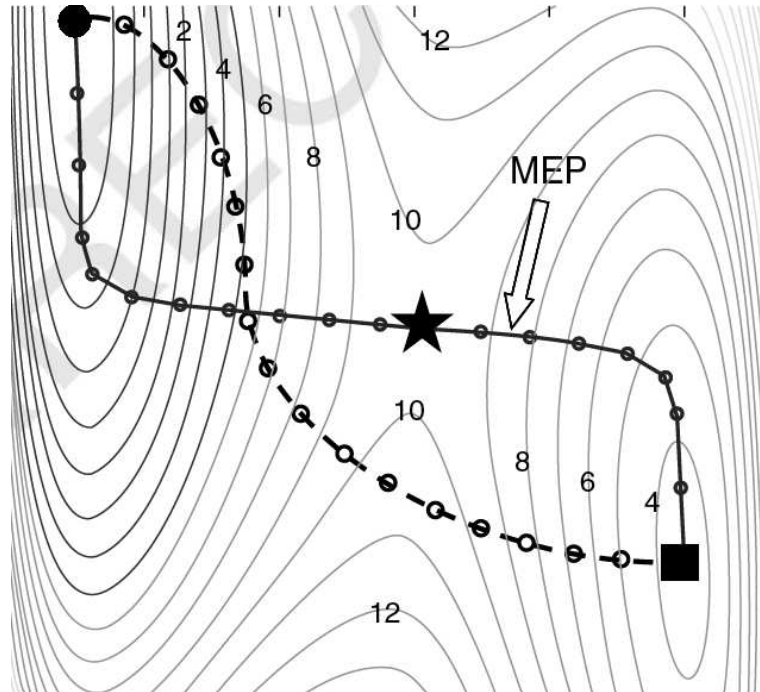


FIGURE 2.7: An illustration of the NEB method by using the energy contour of a model system with two degrees of freedom. The dashed line represents an initially guessed MEP that links the initial (circle) and final (square) states of local energy minima. The solid curve is the converged MEP passing through the saddle point (star). Figure reproduced from Ref. [15].

The algorithm of the NEB method involves the following basic steps: an elastic band with $N + 1$ images can be denoted by $[\mathbf{R}_0, \mathbf{R}_1, \mathbf{R}_2, \dots, \mathbf{R}_N]$, where the end points \mathbf{R}_0 and \mathbf{R}_N are fixed and given by the energy minima corresponding to the initial and final states. The $N - 1$ intermediate images are adjusted by the optimization algorithm.

In the NEB method, the total force acting on an image is the sum of the spring force along the local tangent and the true force perpendicular to the local tangent:

$$\mathbf{F}_i = \mathbf{F}_i^s|_{\parallel} - \nabla V(\mathbf{R}_i)|_{\perp}, \quad (2.25)$$

where the projected true force is given by:

$$\nabla V(\mathbf{R}_i)|_{\perp} = \nabla V(\mathbf{R}_i) - \nabla V(\mathbf{R}_i) \cdot \hat{\tau}_i. \quad (2.26)$$

Here, V is the energy of the system, a function of all the atomic coordinates, and $\hat{\tau}_i$ is the normalized local tangent at image i . The spring force is:

$$\mathbf{F}_i^s|_{\parallel} = k(|\mathbf{R}_{i+1} - \mathbf{R}_i| - |\mathbf{R}_i - \mathbf{R}_{i-1}|)\hat{\tau}_i, \quad (2.27)$$

where k is the spring constant. An optimization algorithm is then used to move the images according to the force in Eq. 2.25. In this study, the quenched velocity Verlet algorithm (presented earlier in this chapter) has been used. This minimization procedure was carried out until the force along the path was lower than a prescribed set threshold. Here this threshold was equal to $F_{max} = 0.01\epsilon_{AA}/\sigma_{AA}$.

In this study, NEB calculations were performed on a set of a few hundred MD trajectories of metallic glasses in order to investigate the system escape from initial metabasin and to find activated states of low energy using the method described in the next section. It was also done to be compared with the results obtained with ART. In many calculations the convergence to the MEP was successfully reached within 100 – 400 steps, which needed more than 1000 force calls. Nevertheless, there were still situations when the algorithm failed. If the force parallel to the MEP was large compared to the force perpendicular to the MEP and many images were used (here usually 20 – 22), kinks formed on the elastic band (the images tended to slide off the MEP). After applying the minimization algorithm, the kinks oscillated back and forth preventing the band from converging to the MEP. For around 300 initial-final configuration pairs obtained with molecular dynamics, less than 100 converged well, giving a smooth transition path with the image of highest energy treated as an activated state. But even for these transitions, it was necessary to adjust the number of images or the spring constant in order to make the NEB work. In most of the cases, the spring constant was set to $k = 1.0\epsilon_{AA}/\sigma_{AA}^2$ which is rather stiff, but allows to keep the separation between images close to equal. The problem is that with a stiff band the obtained path can miss the saddle point region. Typically none of the images lands at or even near the saddle point and the saddle point energy needs to be estimated by interpolation. On the other hand, if k is small, more kinks from the MEP are present. The number of images for the successful attempts varied between 12 and 22. Since the

NEB needs both initial and final configurations in order to find activated states, and each convergence has to be treated individually by adjusting the parameters mentioned above, the time spent on getting representative results is incomparably longer than with Activation-Relaxation Technique.

2.2.5 Autonomous Basin Climbing

As stated before, ART tends to give high energy barriers and another method has to be employed to give in principle the lowest activation energy. In this thesis we employed the *Autonomous Basin Climbing (ABC)* method. ABC is an approach for sampling and reconstructing the system potential energy surface. It was developed as a modification of the algorithm introduced for escaping from energy minima and referred to as metadynamics [16, 167].

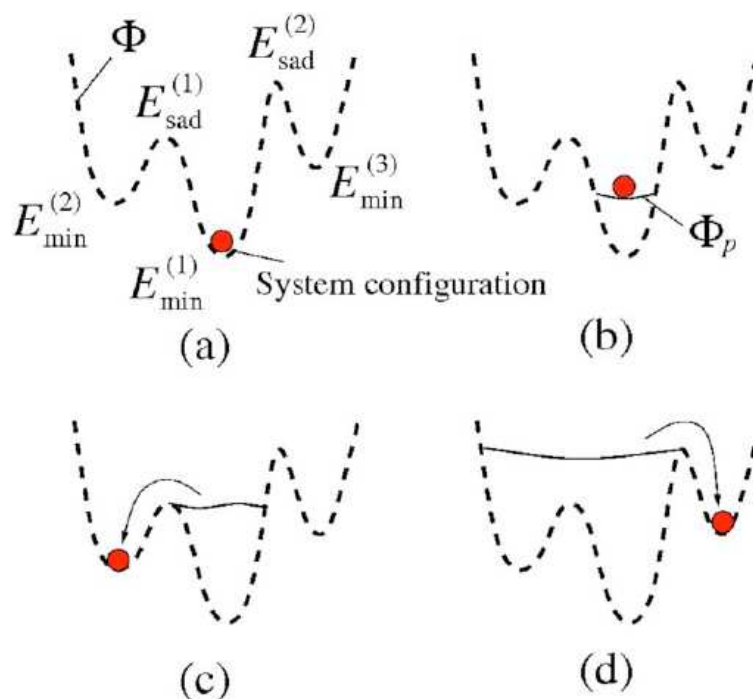


FIGURE 2.8: Schematic illustration explaining the ABC method. Dashed and solid lines indicate original PEL and penalty potential, respectively. Figure reproduced from Ref. [16].

The process starts with the system in a selected local minimum V_{min} with the corresponding atomic configuration of N atoms at $\mathbf{r}_{min}^{(1)}$. From this initial state the

activation step drives the system away from its current configuration by adding a 3N-dimensional Gaussian energy penalty function:

$$\phi_1(\mathbf{r}) = W \exp\left(\frac{-(\mathbf{r} - \mathbf{r}_{min}^{(1)})^2}{2\sigma^2}\right), \quad (2.28)$$

where W and σ are prescribed constants which determine the strength and spatial extent of the penalty function, respectively. This process enables the system to start climbing out of its initial local minimum state E_{min} . After adding the penalty function the system energy becomes:

$$\Phi_P^1 = \Phi + \phi_1 \quad (2.29)$$

The activation step is followed by a relaxation step to allow the system to settle into a new minimum energy configuration in the presence of the penalty function. At the end of each activation-relaxation sequence, the system will find itself in a new relaxed configuration with a new energy Φ_P (Fig 2.8b). The cycle is repeated until the system crosses a saddle point during a relaxation step and enters into an adjacent potential energy well (Fig 2.8c and d). The sampling of a new local minimum is confirmed by checking if the conditions:

$$\frac{\partial \Phi}{\partial \mathbf{r}_{min}^{(2)}} = 0 \quad (2.30)$$

and

$$\phi_P(\mathbf{r}_{min}^{(2)}) = 0 \quad (2.31)$$

are satisfied. The condition 2.31 means vanishing difference between Φ_P and Φ at $\mathbf{r}_{min}^{(2)}$. With this new local minimum and the corresponding system configuration one can backtrack along the minimization path to deduce the saddle point and its configuration.

The basic algorithm presented above does not work so well (for instance condition 2.31) and thus for the purpose of this dissertation the ABC method was implemented as follows:

- a random atom was chosen to be fixed in the configuration space

- all particles but that fixed one were displaced by random distances up to $0.09\sigma_{AA}$
- after the displacement, the gaussian penalty functions were added to $N - 1$ atoms, with $W = 1$ and $\sigma = 0.45$
- the system was then relaxed in the presence of the penalty functions using quenched velocity Verlet algorithm until the force was smaller than $0.0001\epsilon_{AA}/\sigma_{AA}$
- the penalty functions were removed and the configuration was quenched again in order to reach the bottom of a visited inherent structure
- the new IS was compared to the initial one and the distance between them was computed. If the distance in the configuration space was larger than $0.2\sigma_{AA}$, the new state was accepted. If the system relaxed back to the initial minimum, another penalty functions were added to $N - 1$ atoms until a new minimum was found
- when the new minimum was detected, the NEB method was used to identify the barriers between the neighboring energy minima
- the next ABC search was started from the same initial minimum with a different atom fixed.

By keeping all the Gaussian penalty functions imposed during the simulation, one eliminates frequent recrossing of small barriers, which is a significant advantage of the history-penalized basin-filling methods.

Unfortunately the efficiency of the ABC method turned out to be even lower than ART. For 1000 searches only around 40 could be accepted. The reason this method was applied to the metallic glasses was that it is difficult to find transitions below $2.0\epsilon_{AA}$ with ART. During the ABC procedure more than 80% attempts concerned the same barrier crossings and one needed many searches to sample the configuration space effectively. Luckily one ABC search was quite fast for the 100-atom system and reached a new minimum after 5 – 7 iterations of adding penalty functions.

Another difficulty concerned the NEB method. As mentioned in section 2.2.4, finding a smooth transition path requires a continuous adjustment of the NEB

parameters. This is very time consuming and does not guarantee a successful result.

Out of the three methods employed in this study, the most effective was the Activation-Relaxation Technique. It can identify enough saddles to build statistically relevant samples, from which stationary distributions can be computed. As it will be shown in the next chapter, the activated states found by ART all lie within a region sampled by MD simulations, which was proved using NEB, although the density of these low energy states was low. Most of the saddles found by ART are too high in energy to be sampled with MD. In this study we made attempts to improve the ART parameters in order to force this method to sample low energy activated states, but these attempts were unsuccessful. Nonetheless it is safe to conclude that thermally-activated transitions can be sampled with ART efficiently enough and other methods presented in this chapter may be used to confirm trends found by ART.

2.3 Structural analysis of glasses

2.3.1 Voronoi tessellation

One of the most frequently used techniques for characterizing the structure of liquids and glasses is the Voronoi tessellation method [217]. By means of this method the amorphous sample is divided into Voronoi polyhedra (VPs) around each atom. The probability of certain topological VPs is then taken as a fingerprint of the short-range order (SRO) of the amorphous alloy.

By taking an array of points and the perpendicular bisect of the vector between them, a large number of intersecting planes can be obtained. For defining the polyhedron associated with a particular point, the smallest polyhedron created around that point is selected. This polyhedron contains all the points that lie closer to the considered center than to any other, and hence a network of such polyhedra completely fills the space. The two dimensional illustration of this method is presented in Fig. 2.9. Each polyhedron contains information sufficient to completely describe the neighborhood of the associated central point. The array of points is thus replaced by an equivalent array of polyhedra and the problem of packing spheres can now be considered in terms of packing polyhedra.

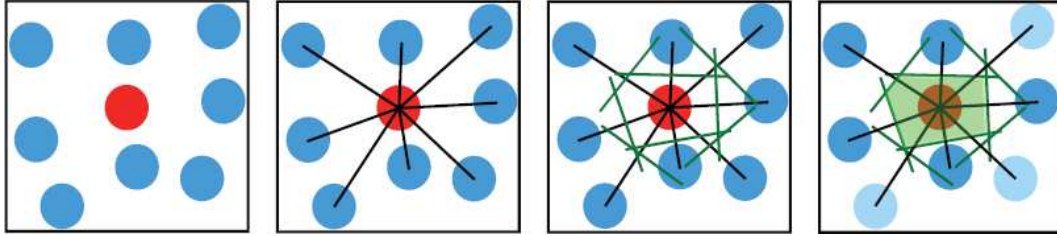


FIGURE 2.9: Construction of a two dimensional Voronoi polygon. Figure reproduced from Ref. [17].

To differentiate the types of constructed polyhedra, the Voronoi indices $\langle n_3, n_4, n_5, n_6, \dots \rangle$ are used, where n_i denotes the number of i -edged faces of the Voronoi polyhedron. The total coordination number (CN) is then:

$$CN = \sum_i n_i \quad (2.32)$$

For example, the well relaxed metallic glasses are characterized by a significant presence of icosahedra, which have a Voronoi index of $\langle 0, 0, 12, 0 \rangle$. The most popular Voronoi polyhedra corresponding to different coordination numbers in several representative metallic glasses are shown in Fig. 2.10 below.

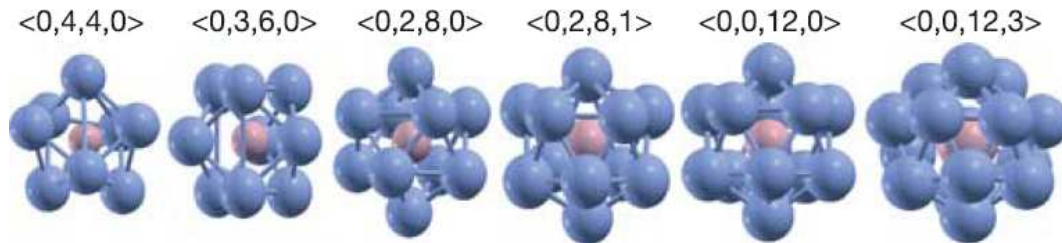


FIGURE 2.10: The atomic packing configurations of different Voronoi polyhedra corresponding to the different CNs. Results taken from Ref. [18].

In this study, a structure of Wahnström metallic glasses has been investigated. The Voronoi tessellation was performed using the *Voro++* software package [218]. The relation between ico-centered atoms and their level of relaxation along with the occurrences of different Voronoi polyhedra (with different Voronoi indices) will be presented in Chapter 3. The structure of Kob-Andersen glass doesn't show an increasing fraction of full icosahedra with decreasing cooling rate. The short range order in case of the latter glass has not been examined here.

2.3.2 Rings statistics in silica glasses

In the analysis of topological networks of liquid, crystalline or amorphous systems, the atoms are often treated as nodes and the bonds between them as links. In such a network, series of nodes and links connected sequentially form a path. If the path is closed, it is called a ring [19].

There are two possibilities for the numbering of rings. On the one hand, one can use the total number of nodes of the ring. This way a N -membered ring is a ring containing N nodes. On the other hand, one can use the number of network forming nodes, for example the number of Si atoms in SiO_2 . Then, an N -membered ring contains $2 \times N$ nodes. In other words, the SiO_2 rings are composed of succession of $Si-O-Si-O-Si-O-\dots$ bonds, but only the number of Si atoms are counted when defining a N -membered ring. This approach was used in this thesis.

Amongst the ways to define a ring [19] one that was used here has been given by King [219], who proposed to consider the rings which are formed of the close neighbors of each node. There are a variety of ways in which this could be effected. In this dissertation, each of the pairs of nearest neighbors of the SiO_4 tetrahedra were considered in turn and the counts of rings were limited to the shortest paths connecting the atoms in each of the pairs (Fig. 2.11). The nearest neighbors were determined using the Voronoi tessellation.

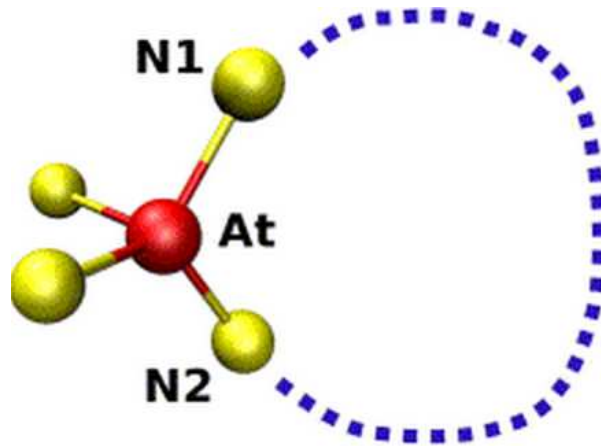


FIGURE 2.11: King's criterion in the rings statistics [19].

With this criterion one can calculate the maximum number of different ring sizes N_{max} , that can be found using the atom At to initiate the search [19]:

$$N_{max} = \frac{N_c(At) \times (N_c(At) - 1)}{2}, \quad (2.33)$$

where $N_c(At)$ is the number of neighbors of atom At . N_{max} represents the number of ring sizes found if all couples of neighbors of atom At are connected together

with paths of different sizes. The maximum number of the shortest paths between two of the nearest neighbors of Si atoms was found to be 6 for most of the nodes, due to the tetrahedral short range order in silica glasses.

In this thesis, the rings were found by recursive searches within a 3000-atom system. For each of 1000 Si atoms the nearest neighbors were determined using aforementioned Voro++ software. Then, two of those neighbors were picked and the search began. To make the program start searching for the shortest rings first, a variable indicating a desired ring size, R_S , was introduced. If the path closed for $R_S = 3$ the next pair of nearest neighbors was chosen. If it did not, R_S was incremented and the search continued until the explored path closed. With this method, rings of sizes between 3 and 9 were found. For the simulated system, the time consumed to find $6N$ rings wasn't longer than 2 – 3 minutes. The obtained results are presented in Chapter 4.

METALLIC GLASSES

The main objective of the study presented in this chapter was to investigate thermally activated processes, which dominate glass dynamics at low temperatures and are preliminary events leading to plastic deformations. Relying on the harmonic approximation of the transition state theory we wanted to check if there was a relation between two quantities characterizing these processes, i.e, between activation energy and attempt frequency. Such relation was observed before and is referred to as Meyer-Neldel compensation rule. The activated states are searched using mainly the Activation-Relaxation Technique method, but, accounting for the downsides of this method, we applied other ways to identify saddle points of low energy (as indicated in the previous chapter). One of these ways involved thermal MD simulations combined with the Nudged Elastic Band method. We found that a system escape from an initial equilibrium state does not occur by a single barrier crossing, but consists of many short-lived intermediate states. We followed the concept of Doliwa and Heuer [184, 185] testing the validity of their picture of the potential energy landscape consisting of connected metabasins, but for temperatures below T_C .

Apart from thermally-activated events, we present an analysis of the short-range order in metallic glasses and the influence of atomic composition and density on the simulated systems.

The amorphous systems considered in this chapter consist of binary mixtures of Lennard-Jones particles interacting via the Wahnström and Kob-Andersen potentials. Two systems modeled with Wahnström potential are composed of 100 and

4000 atoms and contain equal numbers of each type of particles, with the mass ratio $m_A/m_B = 2.0$. They are placed in cubic cells of lengths $4.26\epsilon_{AA}$ and $14.54\epsilon_{AA}$, respectively, to have the same density of $1.2\sigma^{-3}$. The corresponding Lennard-Jones parameters are summarized in Table 2.1. All quantities in this chapter are presented in reduced units: length in units of σ_{AA} , energy in units of ϵ_{AA} , temperature in ϵ_{AA}/k_B and time τ_{AA} in units of $(\sigma_{AA}^2 m_A / \epsilon_{AA})^{1/2}$. The Wahnström potential was cut off and shifted at $R_c^{\alpha\beta} = 2.5\sigma_{\alpha\beta}$, with $\alpha, \beta \in A, B$. A time step of $dt = 0.005$ is used for all molecular dynamics simulations of 100-atom system and of $dt = 0.002$ in case of 4000-atom system.

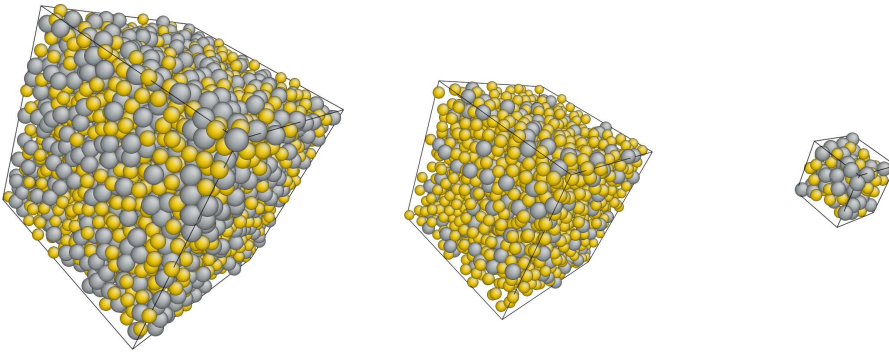


FIGURE 3.1: Metallic glass systems investigated in this dissertation. The cells on the left and on the right present Wahnström systems, the central cell visualizes a Kob-Andersen model glass.

The system modeled with Kob-Andersen potential consists of 2000 atoms - 80% of the particles are of type A, 20% are of type B. They have equal masses and were placed in a cubic cell of length $11.85\epsilon_{AA}$. The Lennard-Jones parameters for this interaction potential are listed in Table 2.2. A time step used in MD simulations in case of Kob-Andersen glass was set to $dt = 0.004$.

Each quench was initialized by equilibration at $T = 1.2$ for 5000 MD steps, followed by runs at a series of temperatures. The total length of the cooling, together with the temperature range chosen, determines the quench rate. Although most experimental studies of glass formation occur at constant pressure, here the runs were performed at fixed volume with periodic boundary conditions. The initial equilibration at constant temperature was done by periodic rescaling of velocities and the succession of energy minimizations at each temperature by quenched dynamics.

Figures 3.2 and 3.3 show the influence of quench rate on the cooling of glasses. In this study, these rates ranged from 6×10^{-2} to $6 \times 10^{-5}\tau_{AA}^{-1}$ for the systems

interacting through Wahnström potential and from 3×10^{-2} to $3 \times 10^{-5} \tau_{AA}^{-1}$ in case of Kob-Andersen glasses.

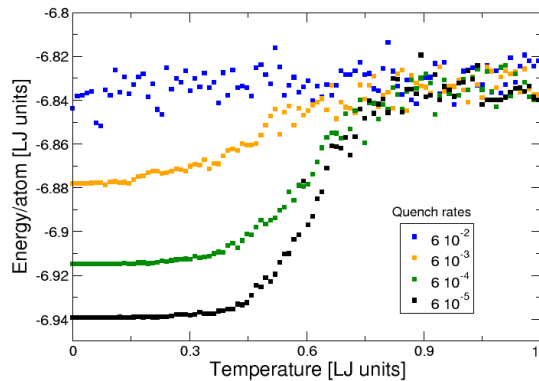


FIGURE 3.2: Influence of quench rate on the cooling of Wahnström glasses.

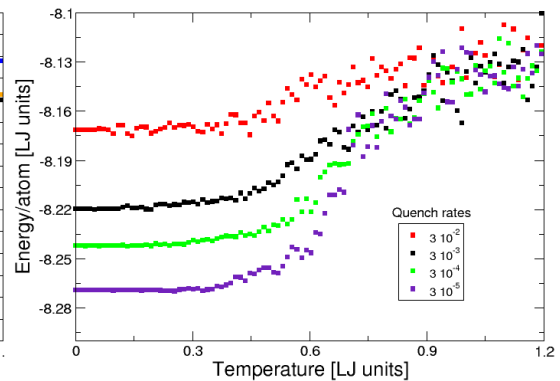


FIGURE 3.3: Influence of quench rate on the cooling of Kob-Andersen glasses.

At high temperatures the systems are fully liquid and due to their high kinetic energy they do not feel the underlying potential energy landscape. A qualitative difference is apparent at lower temperatures, when the systems enter the landscape influenced and landscape dominated regimes (the latter corresponds to temperatures below the mode-coupling temperature, T_C , equal 0.59 for Wahnström and 0.43 for Kob-Andersen systems [12, 220]). Glasses cooled down more slowly are better relaxed with significant differences in energy per atom for different cooling rates. Most of the analysis of metallic glasses in this dissertation were performed on Wahnström systems prepared at the lowest quench rate. The systems quenched more rapidly were used to indicate the trends of changes for a given phenomenon under study.

3.1 Atomic structure of metallic glasses

3.1.1 Short range order

Metallic glasses are materials that lack the long-range atomic order. However, the attractive interactions and differences in size of atoms of different types lead to an order at short and medium length scales. The short range order (SRO) is

characterized by clusters of atoms of one species surrounded by atoms of the other species.

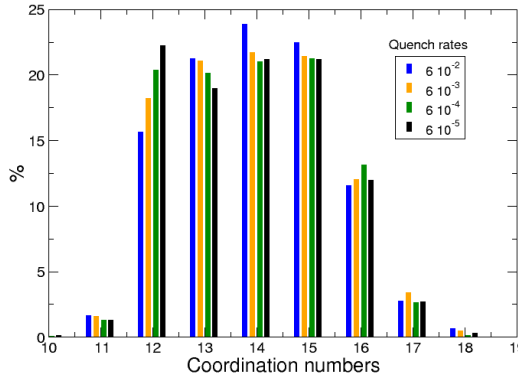


FIGURE 3.4: The fraction of different coordination numbers in Wahnström glasses as a function of a cooling rate.

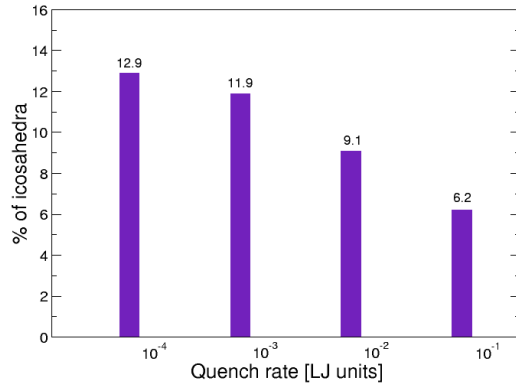


FIGURE 3.5: The cooling rate dependence of the abundance of icosahedra in Wahnström glasses.

Knowing the three-dimensional positioning of the atoms in the studied systems allows the short range order details of its structure to be investigated. The structural analyses were performed on the Wahnström glasses containing 4000 atoms. First, the number of nearest neighbors was obtained for the samples quenched at four different rates. These coordination numbers of each atomic cluster were determined using Voronoi tessellation implemented in Voro++ software package [218].

The image of the short range order that emerges from the results shown in Fig. 3.4 indicates that the SRO consists of various polyhedra of about 11 to 17 atoms. The most abundant type of clusters is cooling rate dependent and varies from 14-faced polyhedra in glasses quenched most rapidly, to 12-faced ones in the best relaxed samples. The number of the latter increases with decreasing cooling rate and one can also notice a clear decrease in the number of 13-neighbored atoms when a glass is quenched more rapidly. For the other coordination numbers, the trends are less clear. In order to find the differences in the clusters of equal numbers of particles, the obtained polyhedra were labeled using the Voronoi indices $\langle n_3, n_4, n_5, n_6 \rangle$.

Figure 3.6 presents the population of the most abundant polyhedra in the metallic glass prepared at the slowest cooling rate. The indices in the figure are arranged in order of increasing coordination number of the central atoms. The figure shows the dependence of the fraction of each type of polyhedra on the type of a surrounded

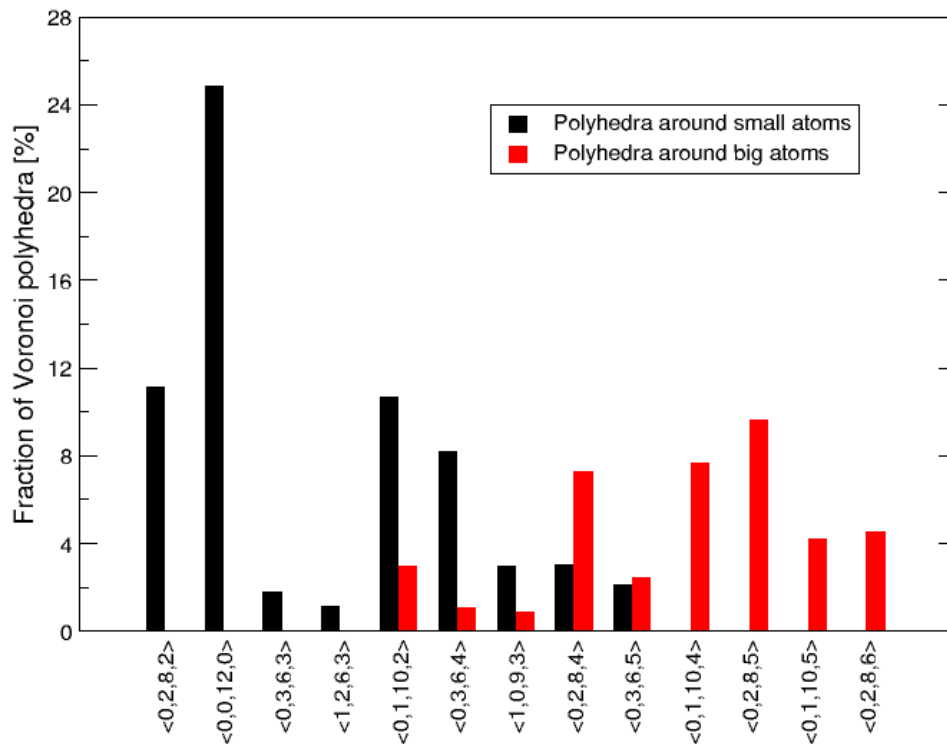


FIGURE 3.6: Population of the Voronoi polyhedra according to the type of atom in the centre.

atom. Most clusters with coordination numbers lower than 14 are centered on small atoms in the system. The ones with the total of nearest neighbors larger than 14 tend to surround bigger atoms. The analysis of the type of atoms forming the clusters does not show any dependence on the type of the atom in the center. From Fig. 3.6 one may note a very high population of icosahedral polyhedra, denoted as $\langle 0, 0, 12, 0 \rangle$ (12 faces, each consisting of 5 edges). Out of 4000 clusters in the system, 517 were found to have this geometry and 497 of them were centered on a small atom (which makes up 24.85% of all polyhedra around small atoms). The figure shows only polyhedra which number exceeds 1% of the total population of polyhedra in the structure. The abundance of icosahedra is a structural measure of the level of glass relaxation for glasses modeled with the Wahnström potential. For Kob-Andersen systems they are not the most abundant. Fig. 3.5 shows the changes in the fraction of full icosahedra for the systems quenched at different rates. Higher population of icosahedra in better relaxed systems indicates (from the local potential energy landscape perspective) that this kind of atomic packing

corresponds to higher transition barriers (deeper local minimum).

Further analysis of the full icosahedra and their neighborhood revealed that they prefer being nearest neighbors with other clusters having many pentagonal faces, for instance $\langle 1, 0, 9, 3 \rangle$ and $\langle 0, 1, 10, 2 \rangle$. This can be explained by the fact that $\langle 1, 0, 9, 3 \rangle$ polyhedra are formed from full icosahedra when another atom is approaching due to fluctuations to the $\langle 0, 0, 12, 0 \rangle$ cluster, introducing a small triangular face. On the other hand, the $\langle 0, 1, 10, 2 \rangle$ polyhedra are also formed from $\langle 0, 0, 12, 0 \rangle$, but they are very stable and cannot be transformed back to icosahedral clusters as easily as in case of $\langle 1, 0, 9, 3 \rangle$ [196].

3.1.2 Influence of density and concentration of the atomic species

Apart from the short range order, the influence of density and composition of the systems on the energy of atomic interactions have been investigated. Five systems modeled with Wahnström potential were prepared with the ratios of A to B atoms equal to 70 : 30, 60 : 40, 50 : 50, 40 : 60 and 30 : 70. All these systems consisted of 2000 atoms, quenched at the rate of $6 \times 10^{-5} \tau_{AA}^{-1}$ and density $\rho = 1.27$. Both the influence of concentration of the atomic species and density have been probed in case of glasses modeled with Kob-Andersen potential. To study the changes in atomic composition twelve samples of 2000 particles were quenched at the rate of $6 \times 10^{-5} \tau_{AA}^{-1}$ and density $\rho = 1.27$. The ratios of A to B atoms were equal to 83 : 17, 82 : 18, 80 : 20, 79 : 21, 76 : 24, 70 : 30, 65 : 35, 60 : 40, 50 : 50, 40 : 60, 30 : 70 and 20 : 80. For investigating the influence of density the 2000-atom systems of seven densities were prepared, with concentrations in B atoms ranging from 17 to 30% for each density, with the nominal concentration being 20%. The idea came after the publication of Juan de Pablo group from the University of Chicago [220]. They claimed that glasses prepared by vapour deposition onto a substrate can exhibit remarkable stability, and might correspond to equilibrium states that could be reached only by glasses aged for thousands of years. We found that, to some extent, it may be due to the influence of atomic composition, which is more pronounced for Kob-Andersen systems.

Figure 3.7 presents the changes in energy per atom with varying concentration in B atoms for Wahnström and Kob-Andersen metallic glasses. The systems modeled

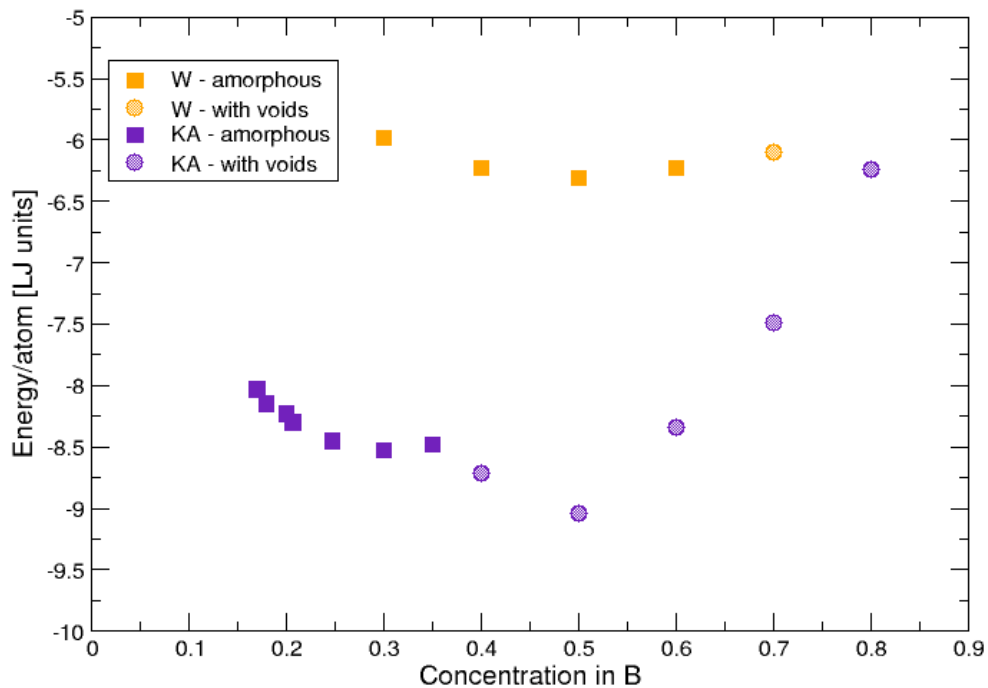


FIGURE 3.7: Influence of atomic composition on the system energy.

with Kob-Andersen potential show a bigger susceptibility to the atomic composition, especially around the nominal composition ratio 80 : 20. Even 1% change in the quantity of B particles, from 20 to 21%, leads to a significant decrease in energy from -8.25 to -8.30 . Increasing the fraction of B atoms in a sample to 30% causes the energy drop to -8.55 , indicating that the nominal composition for Kob-Andersen systems is not the minimum energy one. Interestingly, when decreasing the cooling rate by one order of magnitude, the energy decreases by only 0.03. This behaviour can be understood by accounting for the non-additivity of the Kob-Andersen potential, which favors interactions between A and B atoms. Starting from 40% of B atoms the samples contain voids. One of the tested configurations, consisting of equal number of atoms of each type, crystallized during the quenching process. The rest of investigated Kob-Andersen compositions, with a surplus of B atoms, reached higher energies and had voids.

The systems modeled with the additive Wahnström potential were less prone to changes in the concentration in A and B atoms. The difference between the highest and the lowest energy value was on the order of 5%. Only for the configuration

consisting of 70% of B atoms the voids could be observed. None of the samples crystallized during the preparation. In this case, though, the nominal composition of 50% is the minimum energy composition.

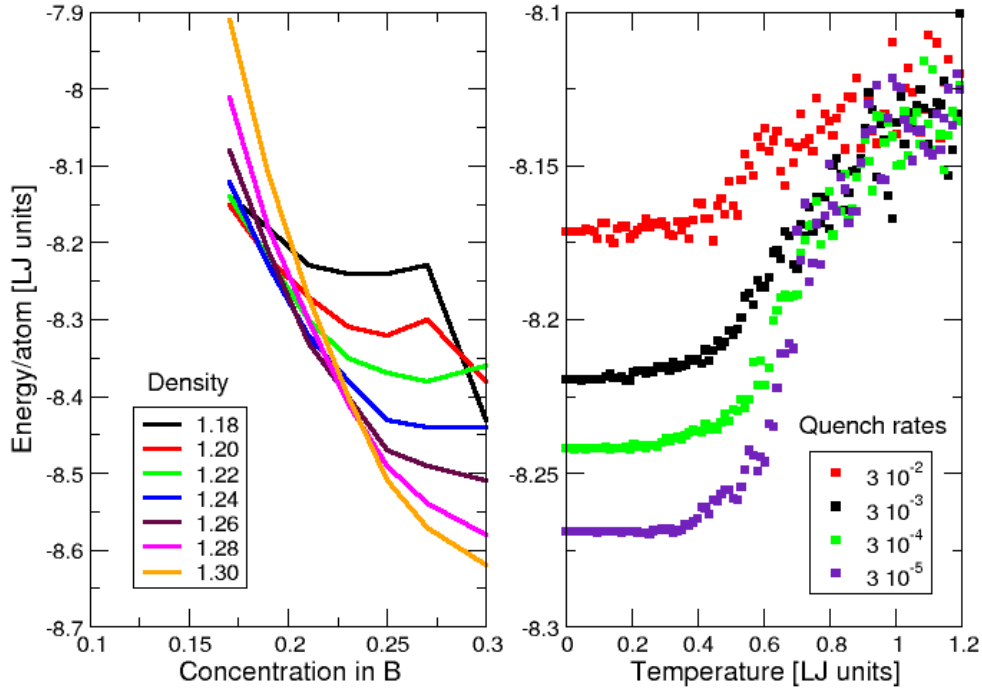


FIGURE 3.8: Influence of density on the system energy (Kob-Andersen potential).

The left plot in Fig. 3.8 depicts the effect of system density on the potential energy as a function of atomic composition. All seven curves show similar trend with increasing number of B atoms in a sample. The sudden drop in case of densities $\rho = 1.18$ and $\rho = 1.20$ at the concentration rate of 0.3 is due to the voids present in these configurations. In the right graph of the figure once again the quench curves of Kob-Andersen glasses are presented. From Fig. 3.8 one may note the large spread of energy values for different densities when compared to the energies of the systems prepared at four different cooling rates. The energies vary from -8.11 to -8.28 for the nominal composition of 80 : 20, which is more than the difference in energies between the highest and the lowest quench rates. In the steep part of the left graph, going from 0.2 to 0.21 in concentration decreases the energy by approximately 0.05 to 0.1 for higher densities. This corresponds to about three orders of magnitude in quench rate. The energy is the most sensitive to changes

in the composition but the density has also an influence. At the concentration in B atoms of 0.2, the change in the density from 1.2 to 1.3 increases the energy by around 0.1, which is a big difference. The influence of density and composition is expected but not as much as seen here, in particular for the composition.

3.2 MD trajectories of metallic glasses

3.2.1 Return probabilities

From the hierarchical structure of the potential energy landscape one can distinguish local minima, connected by low-energy saddle points, that form clusters called metabasins (MBs). For temperatures below the mode-coupling temperature, the thermally-activated transitions between these structures govern the structural relaxation of glasses. It turns out that escapes from metabasins do not occur by single hops between PEL minima, but correspond to complicated sequences of metastable, short-lived states. Their lifetime ranges from 1 to more than 10000 MD steps.

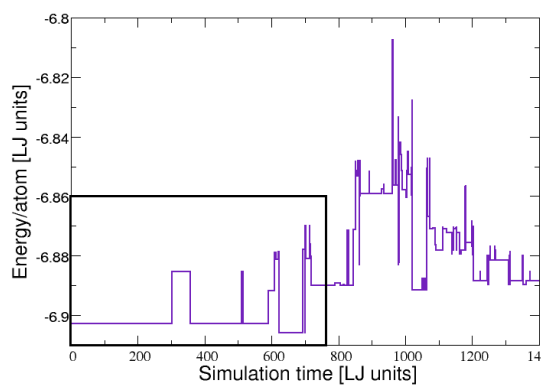


FIGURE 3.9: Molecular dynamics trajectory of a 100-atom Wahnström glass at $T = 0.43$. The magnified area is presented in the figure on the right.

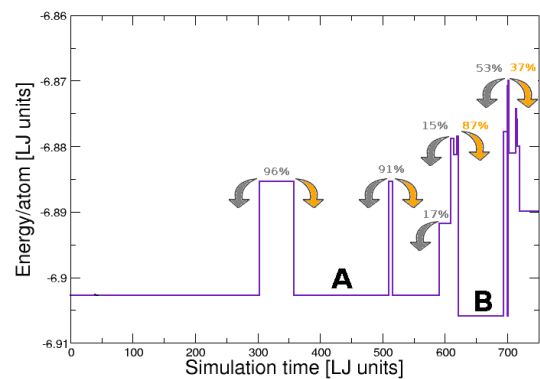


FIGURE 3.10: A slice of the MD trajectory with probability of returning to a given metabasin.

Figure 3.9 presents a molecular dynamics trajectory of the 100-atom Wahnström system at $T = 0.43$. This trajectory was obtained using an interval bisection

method, which locates transitions to an accuracy of 1 MD step [183], which allowed to determine those short-lived, intermediate states on the escape way from the initial metabasin. Since it is computationally very expensive to quench the simulated system every time step, it is minimized every fixed number of steps. In this case the quenching frequency was set to $\Delta t = 1024$ MD steps. If the same minimum is found at t_0 and $t_1 = t_0 + \Delta t$, the transitions in the meantime (if any) were not accounted for, since no relaxation occurred. If the minima at t_0 and t_1 differed, it did not mean that the one at t_1 was a direct successor of that at t_0 and further minimizations in this time interval were necessary. In order to achieve this, the quenching frequency was divided by 2 and the configuration was minimized at $t_2 = (t_0 + t_1)/2$. Then, if the minimum at t_2 was the same as at t_0 , it meant that the transition occurred between t_2 and t_1 and this range was further bisected to localize the transition. If the minimum at t_2 was different from that at t_0 , the above operation was performed on $t_0 + t_2$ interval. These steps were repeated until the quenching frequency was equal to 1 MD step and such procedure finally gives all relevant transitions. In case of the trajectory presented in Fig. 3.9, the distance in the configuration space between two successive minima had to be larger than $d = 0.2$ in order to accept the transition. The time step of MD simulation was set to $\delta t = 0.005$.

Having the intermediate, short-lived states determined during the escape from a metabasin, one can assess when the system leaves the range of attraction of the metabasin. The idea is to define a return probability p_{back} , that would tell if a considered metastable minimum belongs to a particular metabasin. In order to calculate this quantity, 100 MD runs at $T = 0.43$ were performed starting from a selected short-lived state. Each realization, preceded by a randomization of the atomic velocities, was expected to reach a given metabasin within 100000 MD steps (time step as before). The trajectory from initial to final states was obtained using the interval bisection method. According to the criterion from Ref. [183], intermediate minima are said to belong to the initial metabasin if $p_{back} > 50\%$, i.e. if more than 50% of the trajectories returned back to the initial metabasin. Otherwise, the system escape is regarded as complete.

Figure 3.10 shows the examples of computed probabilities of returning to one of the long-lived minima (denoted as A and B) from several selected metastable minima. First two short-lived states correspond to back and forth hopping between the basins forming the long-lived state. The successful escape from state A to B starts after around 600 time steps, leading through an intermediate state with probability

$p_{back} = 17\%$, which indicates that this state already does not belong to long-lived state A. The next metastable state on the way also suggests that the system at this point has left the range of attraction of state A. The assumptions behind the idea of p_{back} say, that its value depends, inter alia, on the distance in configuration space between the initial metabasin and a short-lived minimum visited during the escape. It is expected to decrease with increasing spatial separation of the states. In case of this study, the correlation between p_{back} and the distance in configuration space could be observed only for a particular metastable minimum, i.e. the state from Fig. 3.10 with $p_{back} = 15\%$ towards A is away from this state by 2.65, whereas its distance to B is equal to 1.84, which results in $p_{back} = 87\%$ for this minimum. On the other hand, the separation between the state of $p_{back} = 53\%$ towards state B and state B is 1.79. This suggests other quantities/mechanisms influencing p_{back} , but this has not been looked at within this dissertation. For around 100 escapes investigated, the trend described above was observed for more than 80% of them (in some cases the state with lower p_{back} towards one long-lived state was found to be more distant from a state towards which it has larger p_{back}). The observation that even for the first intermediate states on the escape way from the initial long-lived state, the returning probability may be lower than 50%, suggesting that they already don't belong to the initial state is connected to the configuration entropy of the system. The first jump opens many ways of arranging the particles, many new transitions and thus, the probability to return is small, even if the distances are also small.

As one can see from Fig. 3.10, it is possible to find short-lived states with the sum of p_{back} 's towards two different metabasins crossing 100%. The analysis of MD trajectories between these states revealed that in such cases the trajectory to a long-lived state with lower p_{back} leads through the MB with higher p_{back} . This means that, for example, one can expect a nonzero probability of reaching state A from B during these 100 MD runs described above (what was checked and for this particular case $p_{back} = 13\%$). From the work presented in this section one may conclude that the notion of returning probability is less interesting below T_C , although it was fruitful near the mode coupling temperature as presented by Doliwa and Heuer [184, 185]. At low temperatures metabasins appear to be composed only a single long-lived state, with possibly a few short-lived states with which it undergoes back and forth motion.

The measured distances between the states from Fig. 3.10 along with the corresponding p_{back} 's are given in Table 3.1.

p_{back} into A	p_{back} into B	distance to A	distance to B
96%	–	1.86	–
91%	–	1.86	–
17%	–	1.63	–
15%	87%	2.65	1.84
–	53%	–	1.79

TABLE 3.1: p_{back} 's and distances to metabasins for examples from Fig. 3.10.

3.2.2 Angular characteristics of escapes

Since the escapes from metabasins do not happen by single barrier crossing between two long-lived minima, the spatial aspects of these complex jumps have been investigated. From MD trajectories described earlier in this section, around 60 sets of multim minima sequences were selected. To characterize the escape route from an initial to a final long-lived state, an angle θ between the $3N$ configurational vectors, \mathbf{x} and \mathbf{y} , from the highest intermediate state between the adjacent long-lived states was defined, as presented in Fig. 3.11. The obtained $\cos \theta$, defined as

$$\cos \theta = \frac{\sum_i^{3N} x_i y_i}{\sqrt{\sum_i^{3N} x_i^2} \sqrt{\sum_i^{3N} y_i^2}},$$

were compared with the distances between considered states. This dependence is plotted in Fig. 3.12. The angles range from 40 to more than 90° for the largest separations of long-lived minimum states. Larger distances in configuration space usually mean more short-lived states visited during the escape from the initial minimum. These kind of transitions are very complex and lead through around 100 intermediate states before entering the final state. From Fig. 3.12 it can be estimated that for distances larger than $5\sigma_{AA}$ the value of $\cos \theta$ reaches values between 0 and 0.2, which corresponds to angles between 80 and 90°. The angle θ may be regarded as an angle between exit points from the initial long-lived states and entry points to the final minima. Therefore, for large separations one can find transitions where the intermediate states are altogether so long-lasting, that the exit and entry points become uncorrelated and the system forgets how it escaped from the initial minimum when entering the final one. Nevertheless, these results should be treated as an introduction to a further, more detailed analysis, since the

aspect of short-lived minima has been looked at within this dissertation only for a small set of data at one temperature.

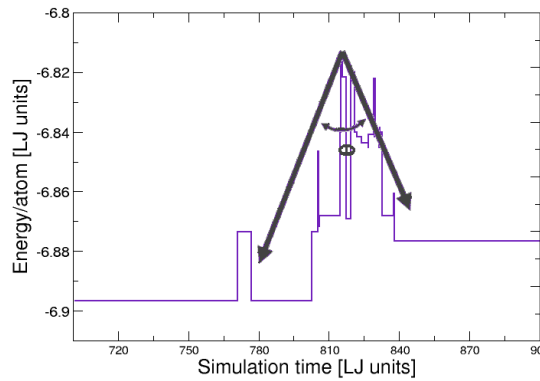


FIGURE 3.11: Definition of angle θ between initial and final metabasins.

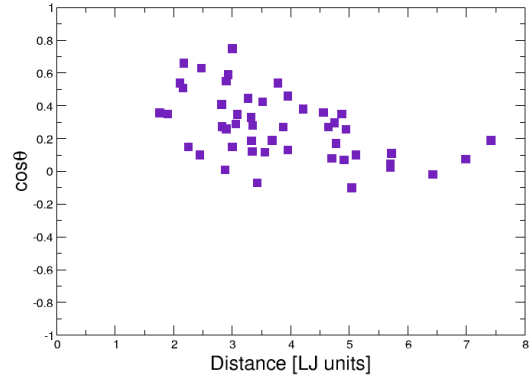


FIGURE 3.12: The dependence of $\cos \theta$ on the distance in configuration space between initial and final metabasins.

3.2.3 Broken bonds

The intermediate states visited by the system before entering the final minimum were also investigated in terms of the atomic bonds, broken during the transitions. The fraction of broken bonds was later compared with the distances between considered states. To obtain the nearest neighbors of each atom in the examined configurations, the Voro++ software package was used. Then, the lists of neighbors in the initial metabasin were compared with the corresponding list for the highest short-lived state, as well as with the neighbors in the final configuration. The comparison was performed as follows: first the coordination numbers of atoms with the same IDs in two configurations were checked. If they differed, the counter indicating the number of broken bonds was incremented. If they were equal, further analysis of the neighbor lists for such atoms was carried out. When any of the neighbors in the compared lists happened to be different, the counter was raised by 1 (regardless of the number of different atoms in the neighborhood). The obtained results in function of distance between compared states is presented in Fig. 3.13.

The left graph in the figure above depicts the fraction of broken bonds between the initial metabasin and the highest short-lived minimum, visited by the system on

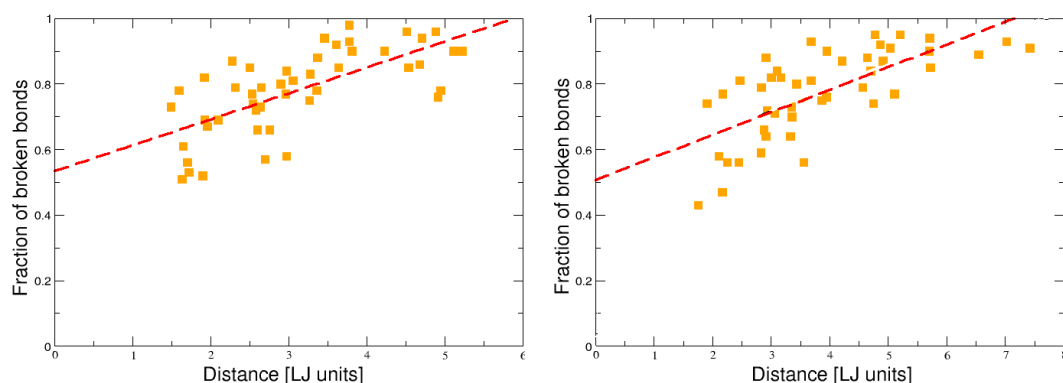


FIGURE 3.13: The fraction of broken bonds during the transitions to the highest intermediate state (left graph) and to the final minimum (right graph) as a function of distances between two states.

the way towards the final metabasin. Though dispersed, these data show a linear trend, with increasing fraction of particles that exchanged or removed atoms from the shell of nearest neighbors for larger distances. It shows that reaching states that are more distant in configuration space involves more atomic rearrangements. The right graph in Fig. 3.13 presents the fraction of broken bonds between the initial and the final minimum. The results show the same trend as those from the left graph and can be approximated by a linear function.

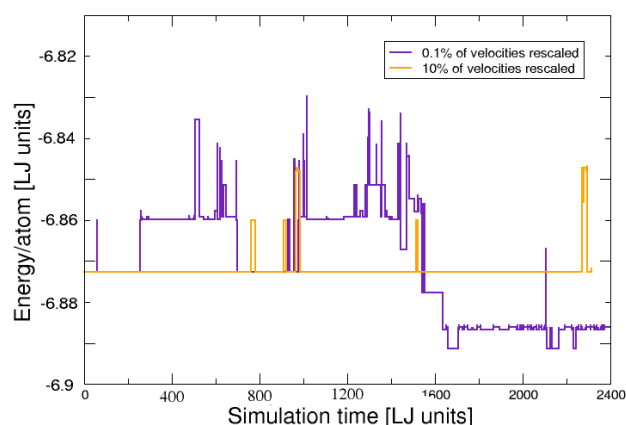


FIGURE 3.14: Influence of thermostat on system's dynamics.

between metabasins through many short-lived minima and need a more insightful investigation.

The comparison of the fraction of broken bonds at the highest intermediate and final states revealed, that for a given escape route, the fraction is usually lower at the final state, which suggests that the bonds tend to be restored on the way from intermediate towards final minimum.

As for the angles between configurations, these results should be treated as a very first approximation of the system behaviour during the transition be-

All the results presented in this Section come from thermal simulations at $T = 0.43$. The temperature was kept constant using Andersen thermostat (described in Chapter 2), rescaling 0.1% of atoms velocities every MD step. The importance of thermostat's strength and its influence on the system's dynamics is shown in Fig. 3.14. Apart from the MD trajectory with 0.1% of velocities being rescaled (in purple), it presents the trajectory of the same initial system when the thermostat was applied to 10% of atoms (in orange). For the 100-atom system used in this MD run, rescaling 10% of velocities was enough to limit the dynamics to back and forth jumps inside the initial metabasin. Since these jumps are localized and involve rearrangements of a few to a few tens of atoms, rescaling 10 randomly picked atoms every MD step prevents the system from performing transitions over higher energy barriers, which would require thermal activation of a cluster of more atoms not being affected by the thermostat. In case of a system consisting of bigger number of particles, the transitions between metabasins may be still present for a thermostat of this strength, but it hasn't been investigated in this study.

3.3 Thermally-activated processes

Thermally activated processes are ubiquitous in the structural relaxation and deformation of glasses at low temperatures. It was shown that the dynamics becomes dominated by thermally activated transitions between local inherent structures (ISs) when the temperature decreases below the mode coupling temperature T_C [156]. In this regime, MD simulations become inefficient because the waiting time between transitions increases exponentially with decreasing temperature and rapidly exceeds the MD time scale. An alternative approach, applied for the purpose of this thesis, is to use the transition state theory (TST). To identify the transitions mentioned above, the concept based on an exploration of the potential energy landscape was employed. Within the harmonic approximation of TST the rate of escape from an initial equilibrium state can be expressed as (Eq. 2.22)

$$k^{hTST} = \nu_{att} \exp\left(-\frac{E^* - E^0}{k_B T}\right),$$

where $E_A = E^* - E^0$ is the activation energy, E^0 the energy of the initial state and E^* the energy of the saddle point. The attempt frequency is given by Eq. 2.23:

$$\nu_{att}^{hTST} = \frac{\prod_{i=1}^{3N-3} \nu_i^0}{\prod_{i=1}^{3N-4} \nu_i^*},$$

where $\{\nu_i^0\}$ and $\{\nu_i^*\}$ are the real nonzero eigenfrequencies of the equilibrium and activated states, respectively, computed by diagonalizing the Hessian matrix of the system in both states. The three degrees of translational invariance and the imaginary frequency associated with the unstable mode were omitted in the above equation.

Activated states are identified here using mostly the activation-relaxation technique (ART), which allows one to explore the configuration space around equilibrium configurations in search of activated states, starting in random directions. As stated in Section 2.2.3, an exhaustive search in case of disordered solids is unfeasible because of the exponential number of saddle points. However, ART can identify enough saddles to build statistically relevant samples, from which stationary distributions can be computed.

3.3.1 Distributions of activation energies and attempt frequencies

The potential energy landscape of the quenched glasses was explored using ART until at least 1000 distinct saddle points were found. To obtain this quantity of activated states, around 10000 iterations were necessary, out of which approximately 2000 reached saddle points. Among these saddles, almost 1300 were distinct.

Figure 3.15 shows distributions of activation energies of four 4000-atom systems, quenched at different rates. These distributions have the usual shape with a systematic trend: glasses quenched more slowly have a smaller density of low activation energies, or, in other words, distributions of activation energies shift towards higher energies in better-relaxed glasses. This effect is expected from a simple picture of the potential energy landscape where deeper energy minima are surrounded by higher activation energies. All distributions span over wide range of activation energies and have a characteristic shape with a peak indicating the most probable energy value.

All information about thermally-activated transitions can be found in the initial and activated configurations. To characterize them, apart from identifying saddle points, one needs to determine the other quantity from 2.23, namely the attempt

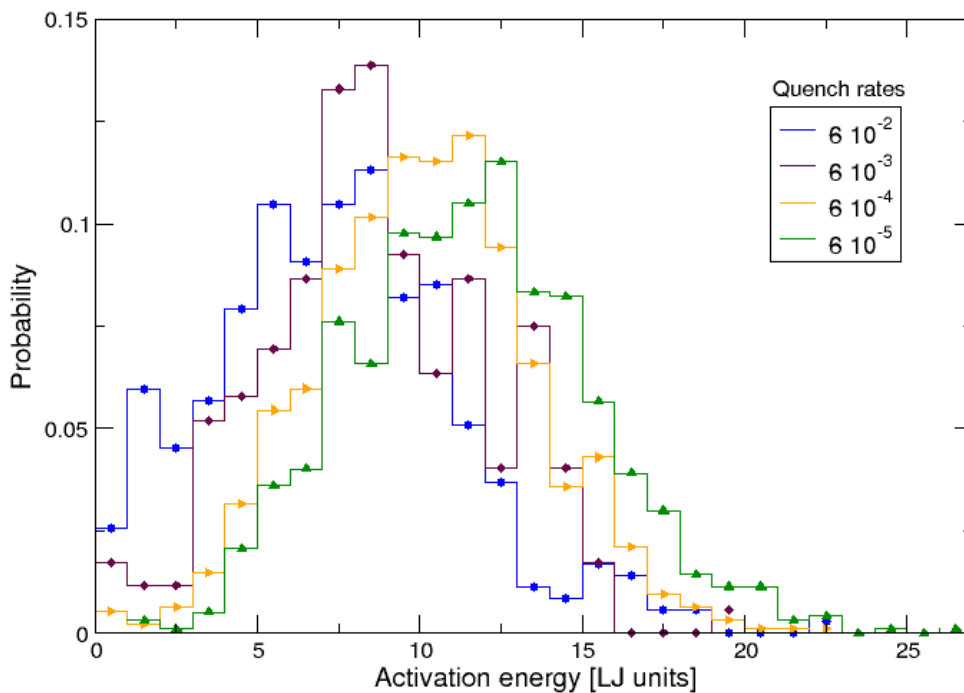


FIGURE 3.15: Distributions of activation energies in glasses quenched at different rates.

frequency. So far, attempt frequencies have received far less attention than activation energies and are usually taken as a constant independent of the process and on the order of 1×10^{12} to $1 \times 10^{13} s^{-1}$ (typical Debye frequency).

Figure 3.16 shows the distributions of attempt frequencies. The range of attempt frequencies is very large, spanning ten orders of magnitude, in contrast with the usual assumption of a constant attempt frequency. By comparison with the distributions of eigenfrequencies (vibrational densities of states) in the initial quenched glasses shown in the inset of the figure, attempt frequencies span a wider range than normal modes, in both the high- and low-frequency limits. Also, in contrast with the vibrational densities of states that are not strongly affected by the quench rate, the attempt frequencies show a clear trend: glasses quenched more slowly have lower attempt frequencies, or, in other words, distributions of attempt frequencies shift towards lower frequencies in better-relaxed glasses. As in case of activation energies, the distributions have a characteristic shape for which the most likely value can be pointed. For typical Lennard-Jones parameters, the time

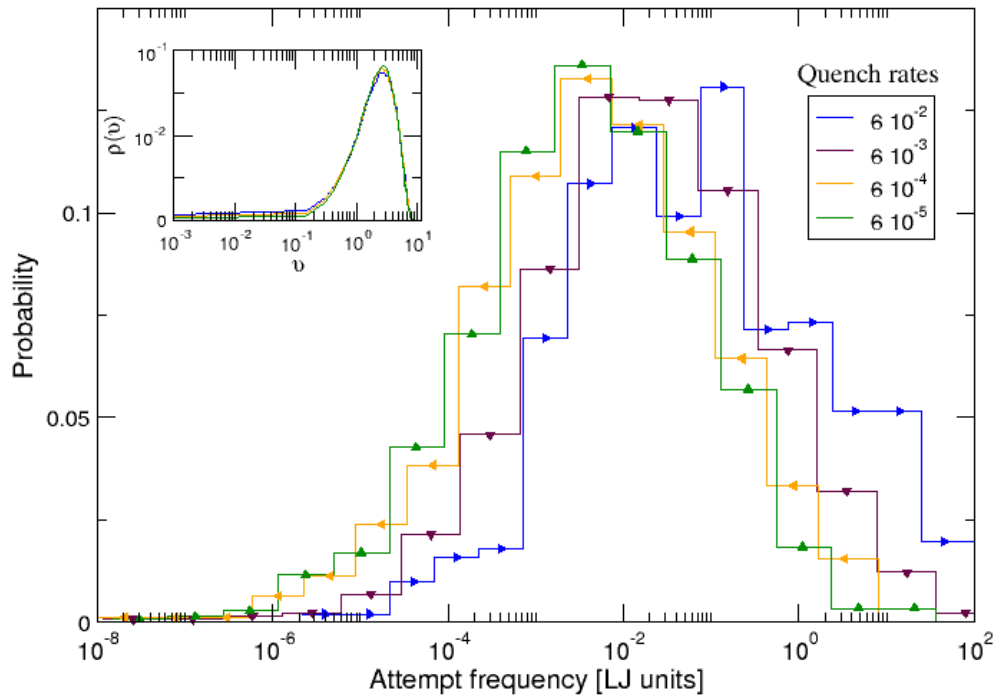


FIGURE 3.16: Distributions of attempt frequencies in glasses quenched at different rates. The inset shows the distribution of eigenfrequencies (vibrational density of states) in the initial quenched glasses.

unit τ_{AA} is on the order of 1×10^{-12} to 1×10^{-13} s. The higher frequencies in the distributions are therefore in the range of the usual estimate of attempt frequencies, but the rest of the distribution is much lower. In a related work, Kopsias and Theodorou [221] found activation entropies spanning $10k_B$, i.e., attempt frequencies spread over four orders of magnitude. The reason for this smaller range is presumably that the entropies were calculated on sequences of connected minima, rather than more exhaustive samplings from given configurations as done in this study.

3.3.2 Meyer-Neldel compensation rule

In nature, a number of phenomena have been shown to exhibit a dependence of the attempt frequency on activation energy, when some external parameter (e.g., composition, pressure, or annealing conditions) is varied. This correlation, observed for a wide range of phenomena, is referred to as the Meyer-Neldel compensation

rule [222]. It appears to be a fundamental property of many families of activated processes following an Arrhenius dependence on temperature:

$$X = X_0 \exp(-E_A/k_B T). \quad (3.1)$$

It is frequently found that, when the activation energy E_A is varied within a family of processes, then the prefactor X_0 obeys the empirical relation:

$$X_0 = X_{00} \exp(E_A/k_B T_0). \quad (3.2)$$

Here X_{00} is a constant (often called Meyer-Neldel pre-exponential factor) and $k_B T_0$ is a characteristic energy for the process in question. Thus the increase in the prefactor X_0 when E_A increases, Eq. 3.2 "compensates" for the decrease in the activation factor in Eq. 3.1, so that the processes take place at a rate larger than would be expected from a knowledge of E_A alone [223].

According to MN rule, Eq. 2.23 can be therefore expressed as

$$\nu_{att} = \nu_{att}^0 \exp(E_A/k_B T_0), \quad (3.3)$$

In this study the dependence between the attempt frequency and the activation energy within the classical hTST has been investigated for 4000 and 100-atom systems prepared at different cooling rates. Random searches for activated states were performed starting from the same minimum for each iteration.

Figure 3.17 shows the relation between the activation energy of an event and its attempt frequency. This plot confirms the large energy and frequency ranges as well as the trends mentioned above; that is, activation energies shift towards higher energies and attempt frequencies towards lower frequencies in glasses quenched more slowly.

Also, although scatters are large, we see that the logarithm of the attempt frequency tends to decrease linearly with increasing activation energy. To check the possible linear correlation, the Pearson product-moment coefficient was computed. For N data points it is given by:

$$r_{xy} = \frac{\sum_{i=1}^N (x_i - \bar{x})(y_i - \bar{y})}{\sqrt{\sum_{i=1}^N (x_i - \bar{x})^2} \sqrt{\sum_{i=1}^N (y_i - \bar{y})^2}}, \quad (3.4)$$

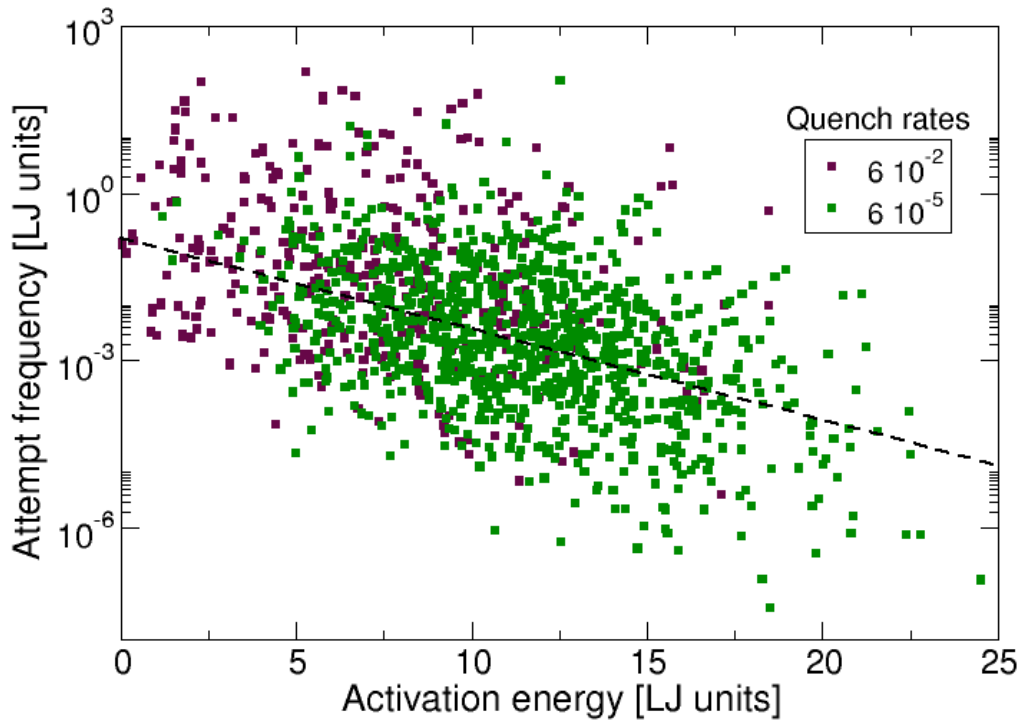


FIGURE 3.17: Relation between activation energy and attempt frequency within the hTST for thermally activated transitions in glasses consisting of 4000 atoms, quenched at different rates. For the sake of clarity, only two quench rates are shown.

where x_i and y_i are the data-sets and \bar{x} and \bar{y} are their respective arithmetic means. The value of r_{xy} ranges from -1 to 1 and these boundary values are obtainable when a perfect linear correlation is present. In case of $r_{xy} = 0$, there is no linear correlation. Pearson's product-moment correlation coefficient was found to increase (in absolute values) with decreasing quench rates, indicating an increasingly clear linear relation in glasses quenched more slowly. For the 4000-atom system, quenched at the rate of $6 \times 10^{-2} \tau_{AA}^{-1}$, its value was equal to -0.30 and for the system cooled down at the slowest rate $r_{xy} = -0.47$. The correlation coefficient wasn't computed for 100-atom systems.

Figure 3.18 presents the dependence of the activation energy on the attempt frequency for a system containing 100 atoms. As for the bigger system, the range of possible frequencies and activation energies is very large. The trend seen previously is reproduced, i.e., small activation energies tend to have high attempt frequencies, regardless of the level of glass relaxation. From the plot one can also

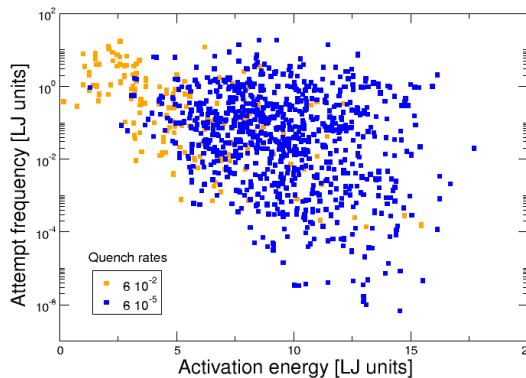


FIGURE 3.18: Relation between activation energy and attempt frequency in 100-atom glasses quenched at different rates.

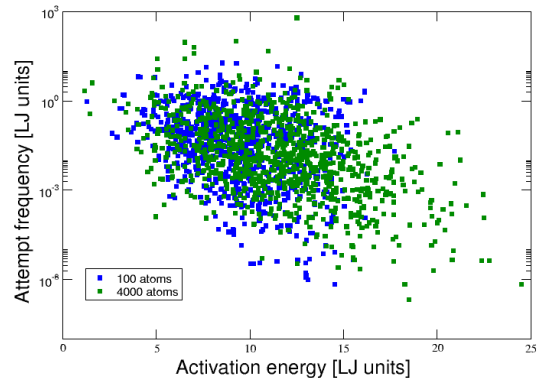


FIGURE 3.19: The comparison between 100 and 4000-atom systems quenched at the slowest rate.

see that, unlike for activation energies, there is no strong effect of the quench rate on attempt frequencies. Figure 3.19 compares the ν_{att} to E_A relations found for 100 and 4000-atom systems, quenched most slowly. The ranges of both investigated quantities are larger (especially activation energies), which is due to the exponential dependence of the number of stationary points on the number of particles in the system. No strong size effects have been observed though.

Sampling of the thermally-activated transitions was also performed for MD trajectories (obtained with the interval bisection method mentioned in the previous section) of the 100-atoms system. The MD simulations included 300 trajectories starting from the same minimum, and the saddle point analysis was carried out with the nudged elastic band method when a change of minimum was identified. Out of these 300 trajectories, NEB calculations were successful, leading to identification of an activated state, for about 100 of them. As shown in Fig. 3.20 in orange, this direct MD analysis was found to visit saddle points on the potential energy surface that all lie within the lower range sampled by the ART calculation.

The energies of the saddle points identified with ART or from MD trajectories were usually larger than $2.5\epsilon_{AA}$. Since the dynamics at low temperatures is controlled by low energy transitions, the third method of sampling the potential energy landscape was applied in order to find these activated states. The search using autonomous basing climbing (ABC) method was performed on the best relaxed 100-atoms system. As in case of MD simulations, the analysis of a saddle point

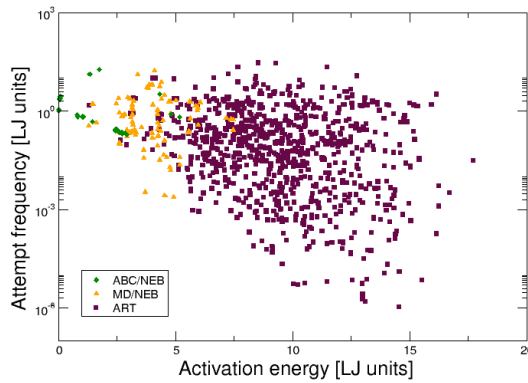


FIGURE 3.20: Relation between activation energy and attempt frequency in 100-atom glass obtained with three different methods for identifying saddle points.

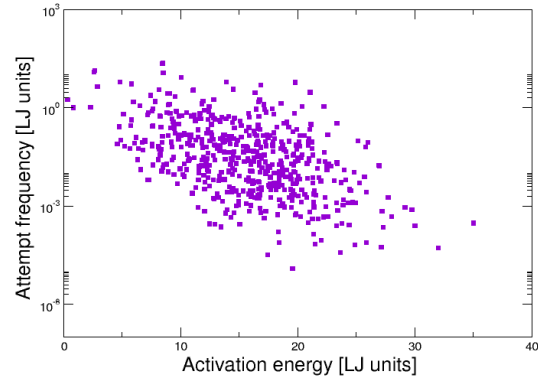


FIGURE 3.21: Attempt frequency in function of activation energy for 2000-atom Kob-Andersen system.

after the system has settled into an adjacent minimum, was carried out using NEB calculations. As stated in the previous chapter, for 1000 saddle points identified, around 40 could be regarded as distinct. The results obtained with ABC are presented in Fig. 3.20 in green. Whatever method was used, the trend reported earlier was confirmed: attempt frequencies tend to increase with decreasing activation energies and their range gets narrower.

This dependence is opposed to the usual Meyer-Neldel rule, where the attempt frequency increases exponentially with the activation energy. A best fit of the data in Fig. 3.17 using an exponential function yields

$$\nu_{att}^{hTST} \propto \exp(-E_A/k_B T_1),$$

with $k_B T_1 \sim 2.50$. Because of the large scatters, the uncertainty on T_1 is large, but, as an order of magnitude, $k_B T_1$ is systematically larger than 1. Theoretical models interpret the MN rule based on two different processes depending on the situation:

- thermal activation into exponentially distributed energy traps for diffusion in disordered systems [224]
- entropy of combining multiple thermal excitations to overcome high-energy barriers [223, 225].

Neither of the above processes is accounted for in the harmonic approximation of Transition State Theory employed in this dissertation, since it applies to a given transition (and not to a distribution of transitions) and it is a harmonic theory, therefore neglecting multiphonon processes. From Eq. 2.23, the attempt frequency is rather interpreted as a topographic property of the potential energy surface related through the eigenfrequencies to the local curvature in the immediate vicinity of the initial and activated states. The Meyer-Neldel rule may therefore not apply within the hTST and, if it does, one may expect that it would appear as an additional process appearing in Eq. 3.3 as a dependence of ν_{att}^0 on E_A .

The relation between activation energy and attempt frequency obtained for metallic glasses is distinct from the effect of multiple particle hops and/or multiple thermal excitations, which yields an effective attempt frequency expected to be proportional to

$$\nu_{att}^{hTST} \propto \exp(E_A(1/k_B T_0 - 1/k_B T_1)).$$

The characteristic temperature T_0 has been related to the glass transition temperature in the case of multiple hops model), i.e., close to the mode-coupling temperature (here $T_C = 0.59$), and to two to three times the Debye temperature in case of multiphonon excitations, which can be estimated from the maximum normal mode frequency, $T_D \sim 0.05$, with $\nu_{max} = 10$ and $\tau_{AA} = 10^{-12}s$. In both cases $T_1 > T_0$, yielding a globally positive Meyer-Neldel rule, with a corrected prefactor.

As pointed before, all the simulations in order to find activated states start from the same minimum. Therefore, the curvature term in Eq. 2.23 from the initial configuration (numerator) is constant for a given quench rate and the variations of the attempt frequencies reflect only variations of the curvature at the activated state. A decrease of the attempt frequency with increasing activation energy thus implies that saddles with a higher activation energy have a larger average curvature. The generality of the very large scatters in attempt frequencies and of the inverse Meyer-Neldel rule was checked by performing the same analysis for several glasses at each quench rate as well as for glasses modeled with the Kob-Andersen potential (see Fig. 3.21).

The dependence of the attempt frequency on the activation energy and the apparent opposition to the Meyer-Neldel rule reported above depend on the process

studied. In Fig. 3.22 a glass approaching a plastic instability, a classical situation encountered in athermal quasistatic plasticity is considered [226]. The 100-atom

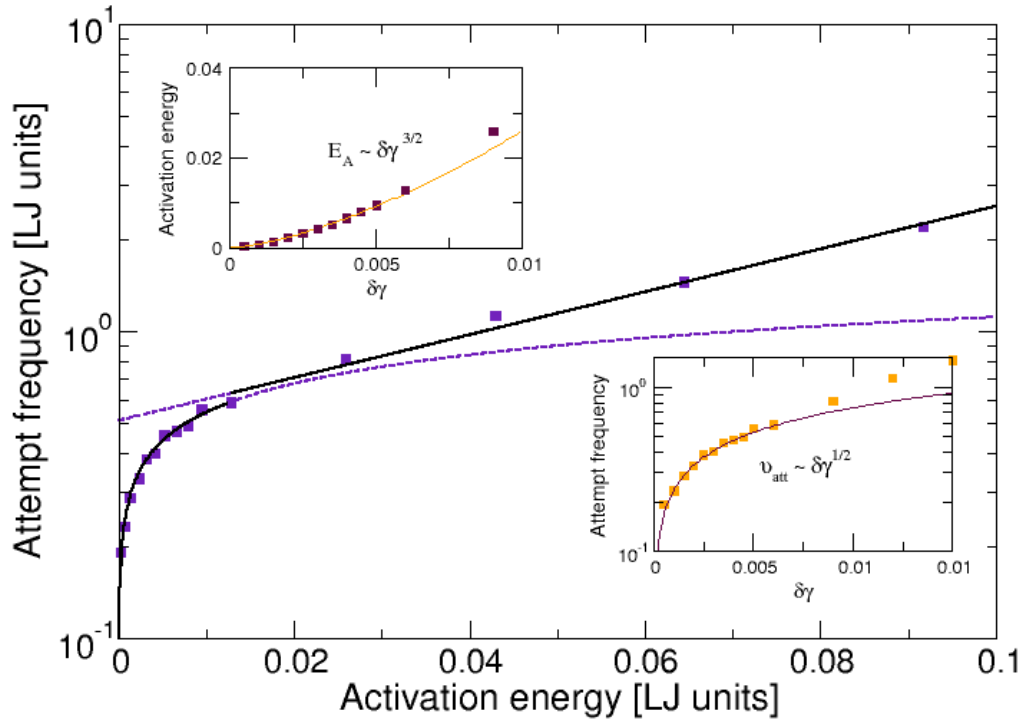


FIGURE 3.22: Relation between activation energy and attempt frequency near a plastic instability in a sheared glass (which corresponds to $E_A = 0$). The insets show the dependence of the activation energy and attempt frequency on the distance to instability.

glass was deformed in an initial IS through increments of simple shear γ separated by energy quenches until an instability to a new IS was reached. It was unloaded to generate a succession of matching configurations in the initial and final ISs at different applied strains. The NEB method was then used to determine the activated states, from which activation energies and attempt frequencies were computed as a function of the distance to the critical strain, $\delta\gamma = \gamma_C - \gamma$. As depicted in the figure above, the attempt frequency decreases as the activation energy decreases near the instability with an exponential dependence for activation energies above about 0.02, in accordance with the usual Meyer-Neldel rule. The attempt frequency decreases partly because of a slow increase of the curvature at the saddle point (in contrast with the trend mentioned earlier) but mostly because, the instability being a fold bifurcation, an eigenvalue in the initial configuration

goes to zero as $\delta\gamma^{1/2}$. The insets in Fig. 3.22 show separately the dependence of the activation energy and attempt frequency on the distance to instability. The expected scaling law for the activation energy is recovered, $E_A \propto \delta\gamma^{3/2}$ [227]. For the attempt frequency, if the decrease was solely dominated by the lowest eigenvalue in the initial configuration, an exponent of 1/4 would be obtained since eigenfrequencies are square roots of eigenvalues. The effective exponent of 1/2 found here (see the inset) is caused by several eigenfrequencies varying near the instability. Interestingly, the same exponent of 1/2, predicted by Kramer's theory is recovered [227], although in this case, half of the exponent comes from the decay of the negative curvature at the saddle point, which is not accounted for in the hTST.

3.3.3 Kinetics of metallic glasses

The large scatters reported above do not rule out the possibility to describe the kinetics of glasses with a single activation energy and attempt frequency, at least at low temperature. In Fig. 3.23 the hTST estimate of the total escape rate, k_{total} , for the four configurations quenched at different rates is presented. It is expressed as

$$k_{total} = \sum_{sampling} \nu_{att}^{hTST} \exp(-E_A/k_B T) \quad (3.5)$$

There is an Arrhenius regime at low temperature, starting at a temperature which increases in better-relaxed glasses. Two fits were added: the dash-dotted lines were obtained by limiting the calculation of the escape rate to the lowest energy transition, while the dashed lines include the transitions within $k_B T_C$ from the lowest energy transition. Just using the lowest energy transition already provides a rather satisfactory agreement with the full calculations, showing that at low temperatures only the very low energy transitions matter. The reason is that the distributions of activation energies in Fig. 3.15 do not increase fast enough at low energies, and are penalized by the corresponding decreasing attempt frequencies, to give a non-negligible weight to transitions with activation energies significantly larger than the minimum.

At low temperatures, the effective activation energy thus reduces to the lowest activation energy of the samples. Predicting an effective attempt frequency is

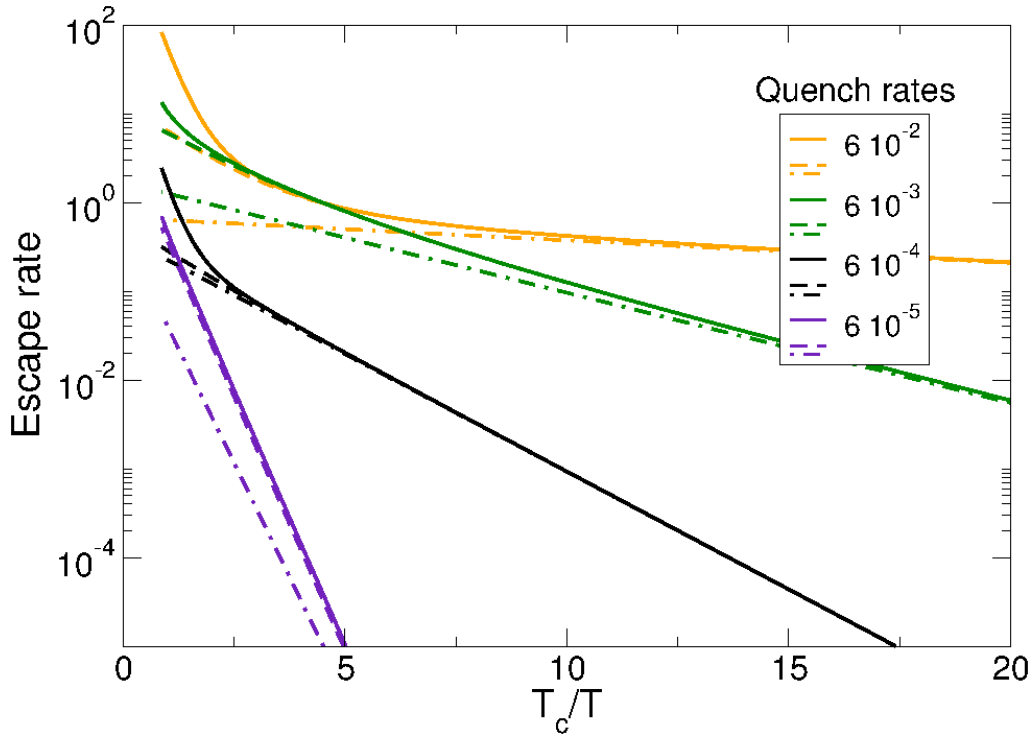


FIGURE 3.23: Prediction of the escape rate in glasses quenched at different rates. The fits were obtained using only the lowest energy transition (dash-dotted lines) or the transitions with $k_B T_C$ from the lowest energy transition (dashed lines).

more difficult because we have to account for a degeneracy factor, i.e., the number of transitions within $k_B T_C$ (see Fig. 3.24).

This effect is most visible for the best-relaxed glass where the prediction from a single transition is a factor between 5 and 10 less than the full calculation. One should also keep in mind that the present rates are only estimates since the samples are necessarily incomplete.

Large variations in the low-temperature rates of Fig. 3.23 were observed depending on the number and properties of low-energy saddles contained in the samples. However, as mentioned before, for the specific system studied here, the

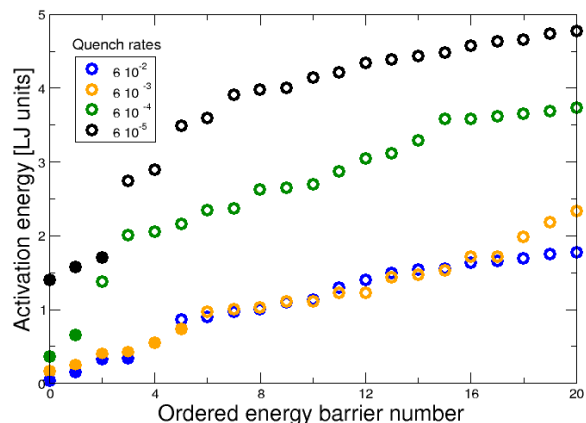


FIGURE 3.24: Twenty lowest energy barriers for glasses quenched at different rates. Filled circles represent the transitions within $k_B T_C$.

saddle points visited during MD simulations lay within the range of lower energies sampled by ART.

The above results show that a glass contains very wide ranges of activation energies and attempt frequencies that are probably characteristic of fragile glasses, which contain diverse atomic environments. It was also found that the dynamics at low temperatures is controlled by the lowest energy transitions, which have high frequencies close to the Debye frequency. This justifies the usual assumption of a single attempt frequency, but also shows that predicting the effective attempt frequency requires that we account for a degeneracy factor, which is difficult to evaluate without an exhaustive sampling of the potential energy landscape near the minimum energy transition.

SILICA GLASSES

Silica glass is the prototype of a glass former that exhibits at ambient pressure an open three-dimensional network structure, comprising of corner-shared SiO_4 tetrahedra. It is the base component for a large part of the earth's mantle as well as most commercial glasses. As a very important glass former, this system has been extensively studied in experiments and by means of computer simulations [141, 198, 200, 228–233]. There are different types of potentials in use, which seem to be able to give a more or less realistic description of the real system. One of the most successful, which was also applied in this study, is the Beest-Kramer-Santen potential. This potential contains only two-body terms, which makes it very attractive for computer simulations. Normally it includes long-range Coulombic interactions, but here we used a further approximation as presented in Chapter 2.

In this chapter the short-range and intermediate-range structure of a 3000-atom silica glass system as a function of cooling rate, density and pressure is investigated. We attempt to answer if the simple BKS potential without Ewald summation is able to reproduce the polyamorphism observed experimentally in silica glasses subject to hydrostatic compression and characterized mainly in terms of coordination numbers. Here, the ring distribution and potential energy landscape are also considered in describing the differences in the glass structure under pressure. The change in density was obtained in two ways: by quenching glasses directly at various volumes and by deforming the glass using three different methodologies.

We will also show, that the dependence of the attempt frequencies on activation

energies for thermally-activated processes in silica glasses is in line with the Meyer-Neldel compensation rule, as opposed to the results obtained for metallic glasses, presented in Chapter 3.

The systems investigated in this chapter consist of 1000 silicon atoms and 2000 oxygen (see Fig. 4.1) atoms of masses 28.086 and 15.9994 u , respectively. They were placed in simulation cells of lengths ranging from 17.82Å to 15.41Å giving nine samples quenched at constant temperature and volume. The densities of these samples varied from 2.20g/cm³ (reference density) to 3.40g/cm³ which covers the range studied experimentally [234]. The Coulomb interaction was taken into account by using the Wolf truncation method and its contribution to the potential was cut-off and shifted at $R_C^{Coul} = 10.17\text{Å}$ [198].

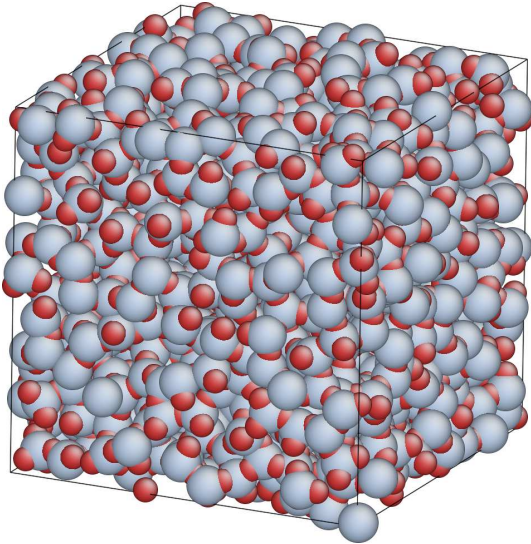


FIGURE 4.1: Visualization of the amorphous silica system investigated in this study.

The non-Coulombic part was truncated at $R_C^{Buck} = 5.5\text{Å}$. The cooling rates investigated here varied between $5.2 \times 10^{14} K/s$ down to $5.2 \times 10^{11} K/s$, so covering 4 orders of magnitude. Each quench was initialized by equilibration at $T = 5200K$ (the mode coupling temperature for silica glass $T_C \approx 1450K$) for 5000 MD steps (the step size was 1.0fs), followed by runs at a series of temperatures until 0K temperature was reached. As in the case of metallic glasses, the initial

equilibration at constant temperature was done using Anderson thermostat and the succession of energy minimizations at each temperature by quenched dynamics. In order to improve the statistics of the results we averaged for each cooling rate over three independent runs. Since the differences in the values of investigated properties were small, the error bars were omitted in the figures presented later in this chapter.

4.1 As-quenched silica glasses

4.1.1 Structural characteristics

Figures 4.2 and 4.3 present the dependence on density of the potential energy per atom and hydrostatic pressure in the systems. For energies one can see an expected trend - glasses quenched more slowly have lower energies, though the differences between the fastest and slowest cooling rates remain limited around 0.1eV . For each quench rate it is possible to indicate a density for which the system reaches the lowest energy. These densities range from 2.3 to 2.6g/cm^3 for the samples prepared slowly and from $2.4 - 2.5$ to 2.6g/cm^3 for the least relaxed glasses. From 2.6g/cm^3 the energy rises for all systems due to changes in bonds lengths and increased repulsion between atoms.

In Fig. 4.3 the changes in pressure when the density increases are shown. For all quench rates the trend is the same and the differences in pressure at each density are most distinguishable between the samples quenched at the slowest and the fastest cooling rates. From the figure the equilibrium pressure for each quench rate can be estimated. For the best relaxed glass the equilibrium density is about 2.30g/cm^3 and increases for glasses quenched faster. This value compares well with the experimental values, showing that the BKS potential in the form applied in this study gives a reasonably good description of the trends in amorphous silica [235]. Since $P = -dE/dV$ the minima in 4.2 should be the same as the points where $P = 0$ in 4.3 and this is approximately what one can see here.

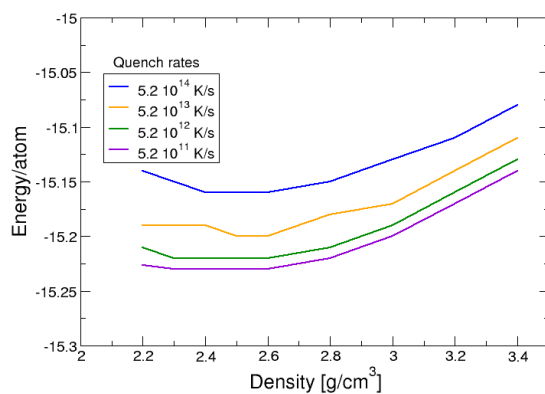


FIGURE 4.2: Energy per atom versus density for different densities and quench rates.

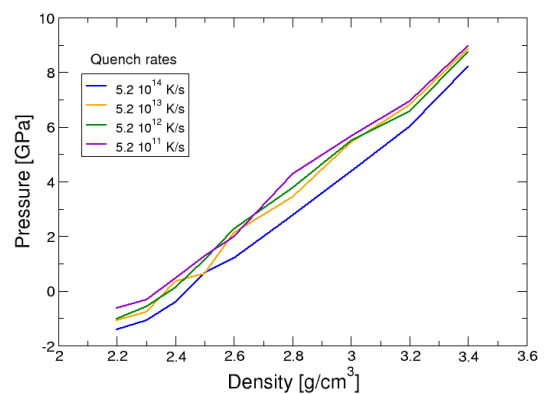


FIGURE 4.3: Pressure in function of density for different densities and quench rates.

From the results depicted in the figures above it is possible to conclude that the density of silica glasses *decreases* with decreasing cooling rate. To understand this behaviour it is necessary to take a look at the tetrahedral structure of amorphous silica. As will be said and shown later in this section, the bond lengths between Si and O atoms and values of $O - Si - O$ angle are rather insensitive to the cooling rate, being close to 1.60\AA and 109.5° , respectively. Thus the tetrahedra do not change their size when the quench rate is varied. The decrease in the density of better relaxed glasses has therefore to be a result of relative arrangement of neighboring tetrahedra. It was suggested (see Ref. [141]) that the tetrahedra become more regular and move away from each other when quenching the system more slowly, thus making the structure less dense. This phenomenon of an opening network is closely connected with the changes in $Si - O - Si$ angle (the angle between neighboring tetrahedra). Its value increases with decreasing cooling rate, indicating that the network of tetrahedra opens up.

As reported in the literature [235, 236], the non-densified silica glass is characterized by a wide distribution of the $Si - O - Si$ angle ranging from 120° to 180° , with the most probable value of 144° to 153° . For the reference system considered here ($\rho = 2.20\text{g/cm}^3$), this value was approximately equal 153.5° , which is in good agreement with experiments.

In experimental study using Raman scattering the Raman spectrum of pristine silica is dominated by a main band at 440cm^{-1} [237]. It has been observed that this band shifts with increasing pressure to about 500cm^{-1} at 4GPa . The main band position of the maximum is related to the $Si - O - Si$ angle and its shift corresponds to the decrease of the inter-tetrahedral angle when the pressure increases. Fig. 4.4 presents the changes in the $Si - O - Si$ angle in silica at

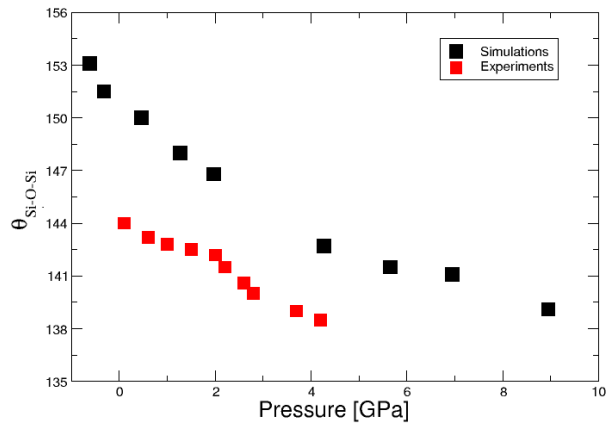


FIGURE 4.4: Inter-tetrahedral angle $\theta_{Si-O-Si}$ in silica quenched at different pressures (in black). In red data from experiments.

different pressures from our simulations of the best relaxed system (in black) and from experiments (in red) [237]. The maximum decreasing rate is observed up to

around 4.0GPa which agrees quite well with the Raman shift of the main band, that saturates around the same pressure, indicating no further decrease of the angle value [238]. As observed in experiments (red squares), the sudden decrease in the $Si-O-Si$ angle occurs between 2 and 3GPa . It corresponds to an anomalous behavior in the bulk modulus, that reaches its minimum at 2.5GPa [237], leading to a more flexible glass. Beyond $3-4\text{GPa}$ the structure is highly pressed and $Si-O-Si$ angle changes more slowly. Eventually, the $Si-O-Si$ angle from our simulations reached 139.5° for the most pressurized sample.

From Fig.4.4 it is difficult to estimate the starting point of the abrupt decrease in the inter-tetrahedral angle for the simulation data. The angle values for the lowest pressures are higher than in experiments, but as mentioned before, they differ also between experimental studies. Nevertheless, the simulation results with applied BKS potential show similar trends as observed in experiments. The values of the $O-Si-O$ angle were rather insensitive to the density and pressure increase. For a perfect tetrahedra this angle is 109.47° [141]. For the reference configuration investigated here it ranged between 90 and 130° with the most probable value of 109.7° , which covers the ranges reported in the literature [198]. The changes observed for as-quenched glasses were smaller than 4° and varied from 109.7° for the reference configuration to 106.4° for the highest pressure.

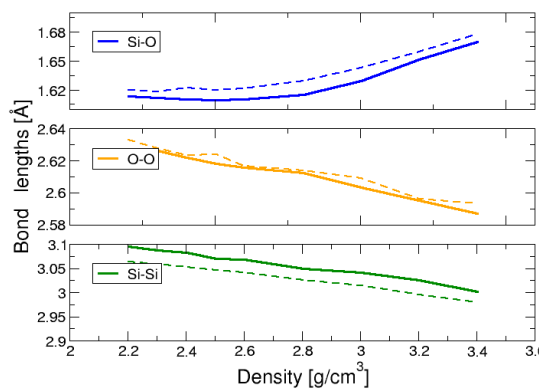


FIGURE 4.5: $Si-O$, $O-O$ and $Si-Si$ bonds lengths versus density for the highest (dashed lines) and the lowest cooling rates (solid lines).

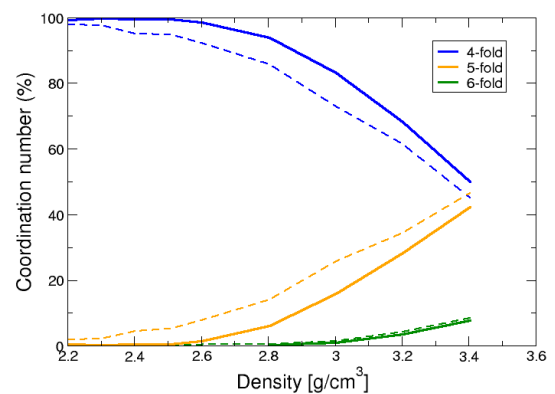


FIGURE 4.6: Coordination numbers of Si atoms as a function of density for the highest (dashed lines) and the lowest cooling rates (solid lines).

To gain a deeper understanding of how the structure of silica glasses changes with increasing density and pressure, the bonds lengths between $Si-O$, $O-O$ and

Si – Si atoms were investigated. The obtained results are presented in Fig. 4.5. The solid lines represent changes for the best relaxed glasses ($5.2 \times 10^{11} K/s$) at each of nine considered densities, whereas the dashed lines correspond to the samples quenched the most rapidly ($5.2 \times 10^{14} K/s$). The distance between *Si* and *O* atoms for the reference density was found to be 1.62 \AA , which is in very good agreement with the values reported from experiments (1.62 \AA [235]). The *O – O* and *Si – Si* bonds lengths for the same density are equal to 2.63 \AA and 3.07 \AA , respectively. In experiments these values vary between 2.63 \AA [239] and 2.65 \AA [235] for the *O – O* bonds and from 3.07 \AA [240] to 3.12 \AA [235] in case of distances between silicon atoms. From the figure one can recognize that with increasing density/pressure the bonds between *Si – O* atoms tend to get shorter up to the density of $2.6 g/cm^3$, which corresponds to $2 GPa$ in pressure and then elongate, reaching 1.67 \AA for the highest density. This nearest-neighbor bond lengthening with increasing density and pressure seems unusual, but it is known from the studies of crystalline SiO_2 that the *Si – O* bond length increases with compression of the *Si – O – Si* angle and with increases in coordination of silicon atoms (bonds elongate to make room for additional oxygen atoms) [241, 242]. The compression of the *Si – O – Si* angle is also responsible for decreasing *Si – Si* separations, as shown in green in Fig. 4.5. The lengths decrease in *O – O* bonds is connected to the lengthening of *Si – O* distances and an increase in *Si* coordination with increasing density. To make room for additional oxygen atoms around a given silicon atom, oxygen atoms need to get closer to each other. The changes in bond lengths in silica glasses do not seem to be affected by the level of glass relaxation. For all investigated densities, the difference in separations does not exceed 1%.

One of the ways to characterize the short range order in glasses is to look at the nearest neighbors of a given particle. Figure 4.6 depicts the changes in coordination number of silicon atoms for the samples quenched at different densities. Solid lines represent the best relaxed glass and dashed lines show the differences in the *Si* neighborhood for the systems cooled down very fast. From the figure one can see that almost all silicon atoms are surrounded by four oxygen atoms for densities up to $2.6 g/cm^3$. This can be understood by taking into account that at low pressures silica forms a network of corner-sharing tetrahedra, each of which has a silicon atom in its center and four oxygen atoms at its corners. For the fastest cooling rate and the lowest density, only around 3% of silicon atoms are not fourfold coordinated. For the slowest cooling rate their number is reduced to less than 0.5%. This shows that the local order of the network, i.e. the frequency of tetrahedra, increases with

decreasing cooling rate. The silicon atoms that are not fourfold coordinated are surrounded by five oxygen atoms and the fraction of fivefold coordinated silicons increases with density as presented in Fig. 4.6. Starting from the density of 2.6g/cm^3 also the number of silicon atoms surrounded by six oxygens increases, reaching approximately 10% for the highest density investigated here. As showed in Fig. 4.5, above this density the $Si - O$ bond lengths increase, indicating these phenomena are connected. As mentioned above, in this range of densities also the influence of the cooling rate is more pronounced, with differences up to 10%. As expected, the above results show that glasses quenched more slowly have more fourfold coordinated silicon atoms and they are more stable in pressure. Similarly, the increase of the $Si - Si$ distance with decreasing cooling rate is consistent with a more open network.

The aspect of Si coordination numbers will be brought back later in this chapter, when discussing the evolution of the silica glass under hydrostatic pressure up to 25GPa . The obtained results will then be compared to experiments (X-ray diffraction), since the latter indicate no fivefold coordinated silicon atoms and direct structural transformation from four to six oxygens around a silicon for higher pressures [243]. This would mean that although the BKS potential does quite well to reproduce the short- and medium-range structure of amorphous silica at ambient pressure, it may be less realistic for highly compressed glasses.

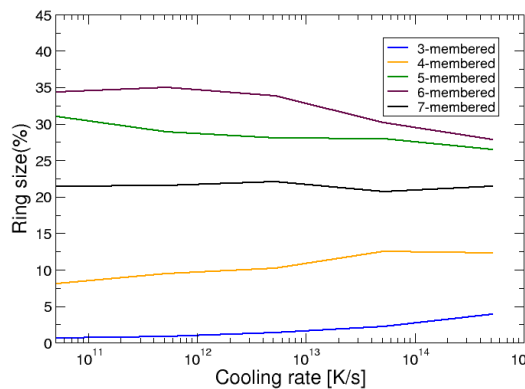


FIGURE 4.7: Percentage of rings of size n versus the cooling rate.

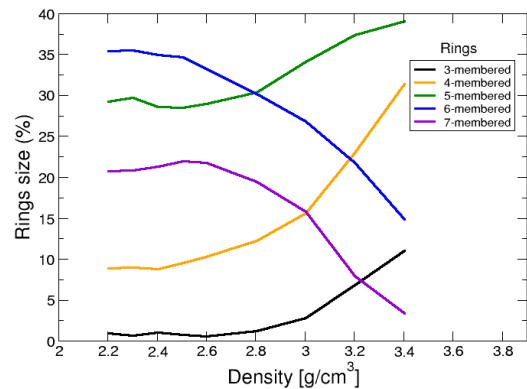


FIGURE 4.8: Percentage of rings of size n versus density.

To characterize the structure of a network of the intermediate length scale the distribution of the frequency of rings of a given size is considered. The definition of a ring has already been given in Section 2.3.2. It is generally believed that

amorphous SiO_2 is structurally similar to the most common crystalline forms of silica and this should also be reflected in the rings statistics. From Fig. 4.7 one can recognize that for all cooling rates investigated, rings of size 6 are the most frequent (35% of all rings). This fact can be understood by considering the phase diagram of silica. At zero pressure the crystalline phase obtained from the liquid phase (β -cristobalite), has only rings of size 6 [141]. It may thus be expected that rings of this size would be the most abundant in glasses. Fig. 4.7 shows that this is indeed the case. From the figure one can also see that very short and very long rings occur rarely and their fraction is lower for better relaxed glasses (less than 2% in case of three-membered rings for the lowest quench rate). The dependence of the ring sizes on the cooling rate is noticeable and means that the structure becomes more ordered when the cooling rate is lowered.

In the Raman spectrum of silica glass at ambient pressure there are two relatively sharp bands at 492 and 605cm^{-1} . These "defect" lines are denoted D_1 and D_2 , respectively [237]. Their origin is associated with symmetric stretching modes of three- and four-membered rings. It has been found that as the density of amorphous silica is increased, these defect lines increase in intensity and shift towards higher frequencies. At the pressure of 4GPa , D_1 shifts to 510cm^{-1} and D_2 to 620cm^{-1} [238]. Figure 4.8 presents the evolution of ring sizes with increasing density. One may easily notice that when the density increases, the quantity of three- and four-membered rings rises, which is in line with the experiments. The rise is accompanied by the decrease in the abundance of long rings (six- and seven-membered). This may be a consequence of the $Si - O - Si$ angle compression as well as the increase in the Si coordination numbers. The ring statistics will be also discussed later in this chapter in the section on the silica glass under hydrostatic pressure.

4.1.2 Potential energy landscape of as-quenched glasses

As in case of metallic glasses, the potential energy landscape of amorphous silica has been explored in order to investigate the nature of thermally-activated processes that are responsible for the structural relaxation of these materials below the glass transition temperature (1446K for SiO_2 [141]). The investigation was performed using the activation-relaxation technique and random searches were iterated until at least 1000 distinct saddles were found for each configuration. The

distributions of activation energies and attempt frequencies were obtained by displacing the system along a random direction from a single initial configuration for each quench rate. The estimation of attempt frequencies was done using the harmonic transition state theory. Eigenfrequencies were determined as before, by diagonalizing the Hessian matrix of the initial configuration and of each activated state.

Figures 4.9 and 4.10 present distributions of activation energies for the silica glass system of density $2.20\text{g}/\text{cm}^3$ at four different quench rates. Similarly to the results obtained for metallic glasses, these distributions are wide and have the usual shape with the same trend: glasses quenched more slowly have a smaller density of low activation energies (the distributions shift towards higher energies when a sample is better relaxed). This result confirms an expected picture of the potential energy landscape, where deeper energy minima are surrounded by higher energy barriers.

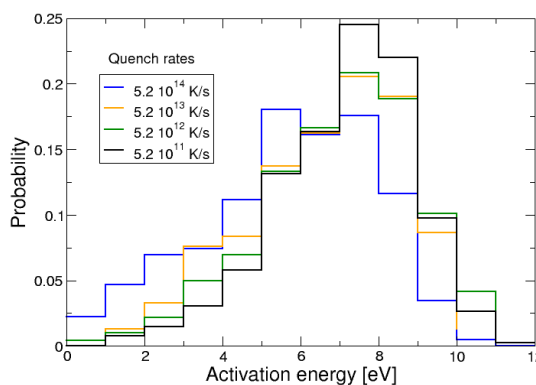


FIGURE 4.9: Distributions of activation energies in silica glasses quenched at different rates when only oxygen atoms are involved ($X_{range} = 1.5\text{\AA}$).

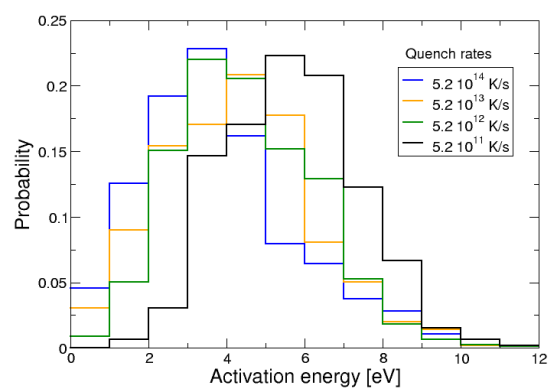


FIGURE 4.10: Distributions of activation energies in silica glasses quenched at different rates when both Si and O atoms are involved ($X_{range} = 4.0\text{\AA}$).

In comparison with Fig. 4.9, the distributions in Fig. 4.10 are strongly shifted towards lower activation energies for all cooling rates. The differences between these two distributions come from the two types of transitions occurring in silica glasses. As emphasized in Chapter 2, one can define a parameter of the ART method that controls the number of atoms to be displaced during the first activation phase, when all eigenvalues are positive. It turned out that when this parameter was set to include a single atom (Fig. 4.9), the transitions involved only the displacement of O atoms. The attempts when silicon atoms were forced

to move systematically failed. There were, of course, transitions when a silicon atom was involved, but it was a result of the $Si - O$ bonds lengths, ranging from 1.40\AA or a bit less, to 1.75\AA . The ART parameter responsible for the number of atoms to displace defines in fact a sphere of a given radius, within which atoms are given a random displacement. It was set to 1.5\AA for single atom ART runs and therefore sometimes it was possible to move a silicon atom, but along with a neighboring oxygen, that was distant by less than 1.5\AA . The simplest transitions, over the lowest energy barriers, correspond to two oxygen atoms exchanging their sites around a silicon atom. To go over higher barriers more oxygen atoms had to perform multiple jumps between silicons in their neighborhood. The number of oxygens displacing the most during a transition oscillated around 5-6 atoms (excluding the simplest transitions as stated above). During such rearrangements, the existing rings are broken and new ones are formed. There were also cases when the rings destroyed on the way to the activated state, were restored after relaxation to a new minimum.

When the ART parameter (denoted in Chapter 2 as X_{range}) was set to 4.0\AA , i.e. included around 10 atoms, the transitions occurred mostly due to displacements of the silicon atoms. In this type of barrier crossings, the simplest ones (with the lowest activation energies) correspond to a partial rotation of a silicon with its nearest oxygen neighbors.

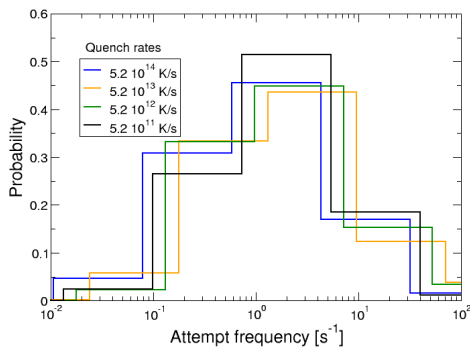


FIGURE 4.11: Distributions of attempt frequencies in glasses quenched at different rates (for the $X_{range} = 4.0$).

For higher energy barriers, the transition occurred by larger displacements of silicon atoms (usually one or two for the highest activation energies), "dragging" the oxygen atoms from their neighborhood. The number of oxygens involved in a transition never exceeded 9. During these events, both rings breakings and multiple oxygen jumps were observed.

Figure 4.11 shows the distributions of attempt frequencies for the systems of $\rho = 2.20\text{g/cm}^3$, quenched at four rates. The range of frequencies is much narrower than in case of metallic glasses and spans around four orders of magnitude. The distributions have very similar shapes and are only marginally affected by the quench rate but it is difficult to point out the trend apart from the distributions for the fastest and slowest cooling rates, where the attempt frequencies of the latter shift towards slightly higher values. Between the three slowest quench rate this trend seems to be the opposite.

The distributions of activation energies were also obtained for amorphous silica quenched directly at different volumes and are presented in Fig. 4.12. All configurations were quenched at the slowest cooling rate. Similarly to the distributions in Figs. 4.9 and 4.10, they show the usual shape with the most probable activation energy for each density investigated in this study.

Also a clear trend can be distinguished: distributions of activation energies shift towards lower energies in more dense glasses.

This can be understood from the description of the thermally activated processes in silica glasses when more atoms are displaced to reach a saddle point. In order to cross a high energy barrier, silicon atoms are moved by larger distances and this rearrangement affects usually two *Si* atoms (one for lower activation en-

ergies) and their oxygen neighbors. With increasing density, the mobility of silicon atoms is hindered and the transitions involve only one or none of atoms of this type. Thus, for high densities, the thermally-activated events reduce to the rearrangement of oxygen atoms, jumping between neighboring silicons, which increases the density of low energy saddles as depicted in the figure.

In Fig. 4.13 the relation between the activation energy of an event and its attempt frequency is presented. For the sake of clarity, only two quench rates are shown. This plot confirms the wide energy and frequency ranges as well as the trends

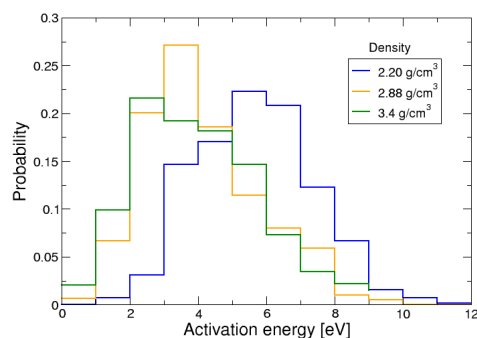


FIGURE 4.12: Distributions of activation energies in silica glasses quenched at different densities at the slowest cooling rate ($X_{range} = 4.0$).

mentioned above – activation energies shift towards higher energies and attempt frequencies towards higher frequencies in glasses quenched more slowly.

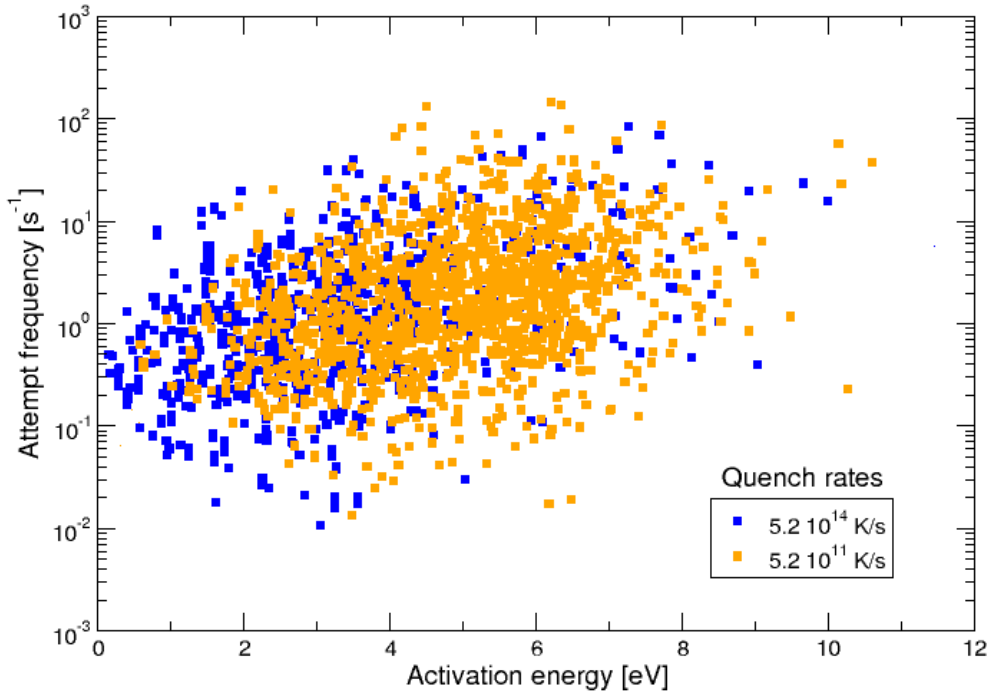


FIGURE 4.13: Relation between activation energy and attempt frequency within the hTST for thermally activated transitions in silica glasses quenched at two different rates.

As opposed to metallic glasses, we found that the Pearson's product-moment correlation coefficient decreases for better relaxed glasses. For the amorphous silica quenched most rapidly it was equal to 0.45 and for the best relaxed 0.37, indicating decreasing a linear relation in glasses quenched more slowly. Only the ν_{att} vs. E_A relations for the case with $X_{range} = 4.0$ are shown but the trends are the same when only oxygen atoms are involved in the transitions.

The dependence from Fig. 4.13 is opposed to the one found for metallic glasses but in line with the usual Meyer-Neldel rule, where the attempt frequency increases on average exponentially with the activation energy. Since the harmonic approximation of the transition state theory has been also applied to silica glasses, the key to explain the observed differences should lie in the nature of the investigated transitions. As mentioned above, there is a single initial configuration for each quench rate. According to Eq. 2.23, an increase of the attempt frequency with

increasing activation energy thus implies that saddles with a higher activation energy have a smaller average curvature (are wider in shape). This picture of the potential energy landscape is more intuitive than the one seen for metallic glasses. This difference is a consequence of the potential used to model silica glasses. The BKS potential was tailored to reconstruct the tetrahedral structure of SiO_2 and one requires that the charges within one tetrahedron are neutralized. Due to this kind of structure, the observed thermally-activated transitions involve less degrees of freedom even for the simplest events as compared with metallic glasses. In metallic glasses the simplest transitions correspond to the rattling within a cage of nearest neighbors, in amorphous silica to oxygen atoms exchanging sites. Even for these events, transitions in metallic glasses involve more collective motions. This may result in less complex structure of activated states on the SiO_2 potential energy landscape.

4.2 Evolution of SiO_2 under deformation.

Silica is one of the most important and abundant materials on earth. In the crystalline state, it exists in several polymorphic forms. In analogy with this phenomenon it was expected that more than one distinct phases may be also formed from amorphous states of silica. These distinct phases, each with a different atomic structure, are distinguished by their density which is a reliable order parameter for *polyamorphism*. **Low Density Amorphous (LDA)** and **High Density Amorphous (HDA)** phases are their usual denominations [237]. Such pressure-induced changes in the structure of SiO_2 have attracted considerable attention because of its importance not only in high-pressure physics but also in materials science and geophysics, since silica glass under high pressure has been used as a model of silicate magma in the earth's interior. Numerous theoretical and experimental studies have revealed that permanent densification of amorphous SiO_2 , the transition between LDA and HDA structures, occurs around 8 – 10 GPa [198, 237, 244].

In this study we would like to reproduce the polyamorphism of silica glasses using the Wolf-truncated BKS potential. The structural changes observed during the hydrostatic compression performed by researches were characterized mainly by the increase of coordination number, i.e., the number of oxygen atoms around a silicon atom, from four to six for pressures between 20 and 40 – 45 GPa [244].

Here, we also consider ring distributions in function of density and pressure. One of the ways to change the density of amorphous silica samples was to quench glasses directly from different volumes, which was presented in the previous sections of this chapter. The other one was deforming glass using three different methodologies:

- quasistatic deformation with strain increments $\delta L/L = 0.00003$ followed by energy minimizations with a force tolerance of $0.001eV/\text{\AA}$
- deformations by finite increments $\delta L/L = 0.003$ followed by MD simulation at $T = 1200K$ for $5ps$ and energy minimizations with the same force tolerance
- deformation at constant strain rate $\dot{L}/L = 0.0003$ and temperature and force tolerance as above

The deformation were performed until the pressure reached $30GPa$.

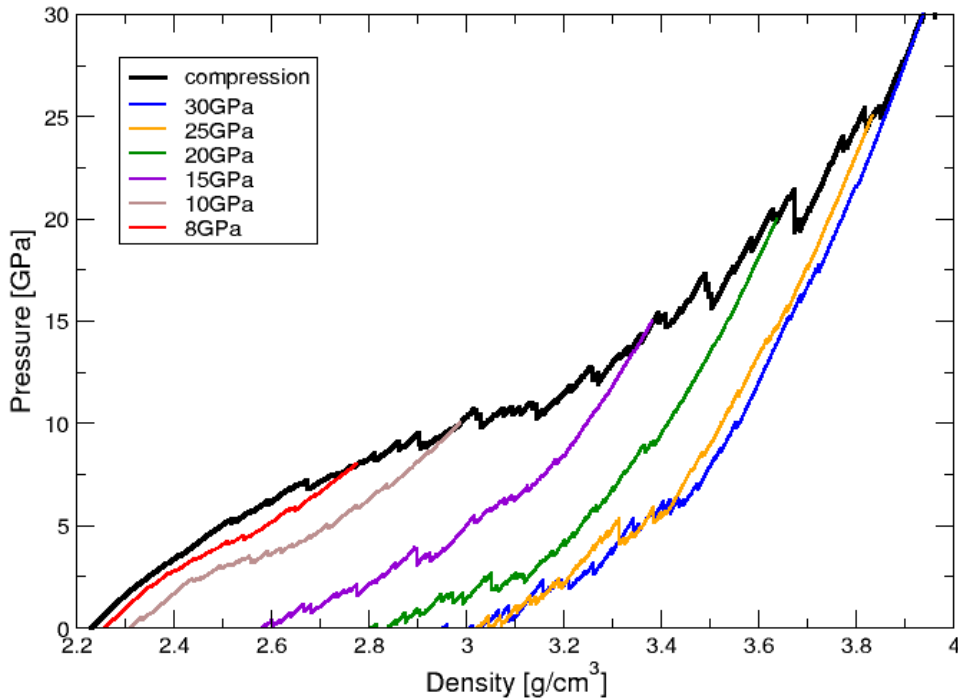


FIGURE 4.14: Relation between pressure and density for quasi-static compression and unloads from chosen configurations at different pressures.

Figure 4.14 presents changes in pressure for the hydrostatic compression of a reference amorphous silica system in function of density. From this figure one can

notice that the pressure increases for increasing density (decreasing volume). The first plastic events occur around 7GPa . As will be shown later in this section, it is also reflected in the coordination number of Si atoms and rings statistics. This suggests that the configurations unloaded from pressures below this value wouldn't depict any permanent densification and sets a transition threshold between LDA and HDA phases. In fact, we performed quasi-static unloadings to zero pressure from pressures 1.5 , 3.0 and 5.0GPa and for each one the relative volume change ($\Delta V/V$) was zero (see Fig. 4.15). Decompression from 8GPa showed the first irreversible volume variation $\sim 2.5\%$. This result confirms early permanent change in the silica glass structure reported from experiments. Further unloadings from the configurations at larger pressures show an increasing changes in volume, with a significant densification occurring above 10GPa . This corresponds to the macroscopic plastic threshold ($\approx 12\text{GPa}$) of silica glass and was reported earlier by Mantsi *et al.* [198]. For pressures exceeding 20GPa the densification tends to flatten around 27% (see Fig. 4.15) which corresponds to a density of 3.03g/cm^3 . This agrees quite well with experimental results obtained by Raman spectroscopy ($\approx 20\%$), remembering the simplifications applied to the BKS potential used in this study [234].

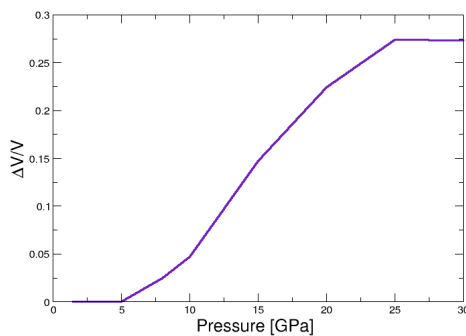


FIGURE 4.15: Relative volume variation after unloadings as a function of maximum pressure applied.

The densification of the system upon pressure is accompanied by structural changes. The characterization of these changes were done by considering the coordination number of silicon atoms, variations in the bonds lengths between $Si-O$, $O-O$ and $Si-Si$ and distributions of rings of different sizes. The performed analyses concerned both compression and decompression. The investigations of the latter were mostly

done for two configurations unloaded to zero pressure from 10 and 25GPa .

The structural changes under high pressure are also indicated by the evolution the $\theta_{Si-O-Si}$ angle, which was also reported for the as-quenched samples in the previous sections of this chapter. Figure 4.16 presents changes in the inter-tetrahedral angle in the samples decompressed to zero pressure from the maximum pressures ranging

between 1.5 and 25 GPa.

This evolution curve is constant below around 8 GPa, indicating the elastic, fully reversible regime, and shows a saturation plateau above 20 GPa, which is in good accordance with the relative volume variations depicted in Fig. 4.15, although we still note that densification starts before permanent changes in $Si - O - Si$ angle.

For a better quantification of the changes in the structure of silica under high pressures, we also investigated the evolution of Si coordination number and bond lengths between different types of atoms as a function of applied pressure.

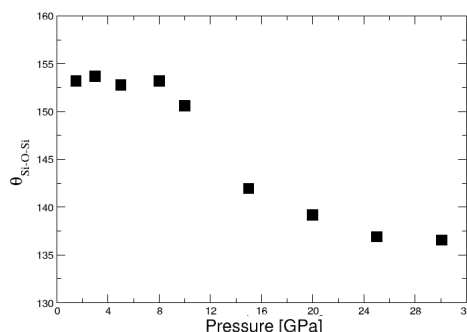


FIGURE 4.16: Inter-tetrahedral angle at ambient pressure as a function of the maximum pressure reached.

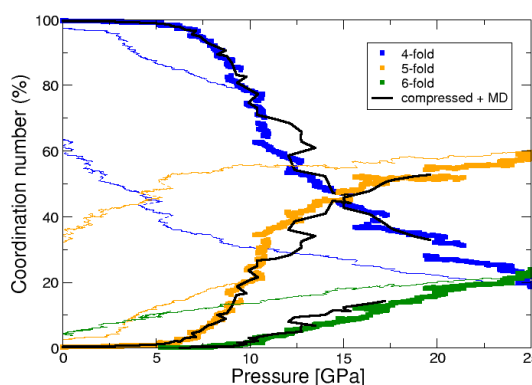


FIGURE 4.17: Coordination number of Si atoms as a function of pressure, during the compression (squares) and decompression (dashed lines) from 10 and 25 GPa. Black lined denote changes obtained from the compression at 1200 K.

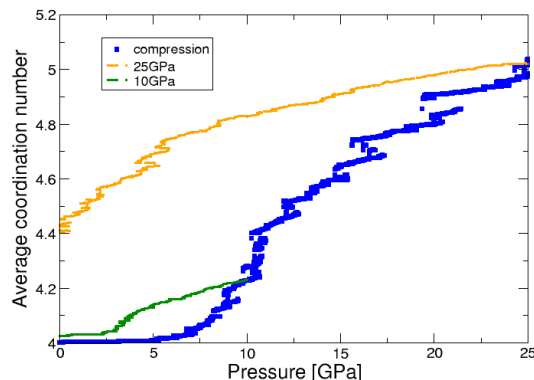


FIGURE 4.18: Average coordination number of silicon atoms during the quasi-static compression (blue squares) and the decompression (dashed lines) from 10 and 25 GPa.

Figure 4.17 presents the evolution of the coordination number of silicon atoms when subject to elevated pressures. Both for athermal and thermal compressions,

the transformation connected with the change of the number of oxygen atoms in the nearest neighborhood of silicons, starts at 5GPa . The amount of fourfold coordination numbers decreases and fivefold increases the most abruptly for pressures ranging from 8 to 15GPa , which is closely connected with the changes observed in the $Si-O-Si$ angles in amorphous silica under pressure. The experimental results show that the structure of silica glasses transforms from fourfold to sixfold coordinated for pressures between 20 and above 40GPa [229, 241, 243]. In this study, we do not reach such high pressures, but from Fig. 4.17 one can notice, that the sixfold coordinated silicon atoms already appear from 5GPa , with a more abrupt increase above 10GPa . The presence of fivefold coordination numbers has been a matter of debate. Researchers usually report the occurrence of the transformation from four to six, without addressing questions about the possible existence of intermediate structures. Computer simulations reveal that fivefold coordinated silicon atoms indeed exist [198], but this can still be an artifact since the BKS potential does not account for the electronic structure of the atoms. It has been suggested though, that the transformation from four- to six-fold coordination is not direct and one can expect the presence of the 5-fold structure [245]. This transformation was studied by X-ray Raman scattering (XRS) and the X-ray absorption spectra of crystalline silica, quartz and stishovite, are well-known (4- and 6-fold coordinated, respectively). The most distinctive difference separating them is the appearance of a second band in the stishovite spectrum. This feature has been used as the fingerprint for the existence of 6-fold coordination in silicates [245]. The question is, whether this peak really signals the presence of the 6-fold structure. When amorphous silica is compressed, oxygen atoms outside the first coordination shell are pushed closer to silicons. Since the only available electrons are those from the oxygen lone pairs and the Si valence octet is already filled, it has to use the empty $3d$ orbitals to accommodate these electrons. Interactions between the oxygen lone pair orbitals with the vacant Si $3d$ orbitals lead to increase Si coordination and stabilization of the dense structure [245]. The hybridization between Si $3d$ and O $2p$ levels occurs at the same energy where the second peak in the x-ray absorption spectrum is observed and takes place whenever an oxygen atom is pushed into the coordination shell of a silicon. Therefore it has been proposed that the emergence of that peak in the XRS is an indication of increased coordination number and not necessarily a signal of the presence of 6-fold coordination [245].

Figure 4.17 also presents the evolution of the coordination number of silicon atoms in amorphous silica when decompressed from 10 and 25GPa . One can see that

for the former sample, the coordination number is almost fully restored, reaching back around 97% of all silicon atoms. In case of the sample unloaded from 25GPa the changes in the structure are much more pronounced. Only around 60% of Si atoms are surrounded by four oxygens, 35% has five oxygen neighbors and the number of 6-fold coordinated silicons oscillated around 5%. These two samples can be regarded as high density amorphous phases of SiO_2 and will be investigated further in this chapter in terms of ring distributions, bond lengths, activation energies and vibrational density of states.

Figure 4.18 shows the average coordination number of silicon atoms during the quasi-static compression (blue squares) and the decompression (dashed lines) from 10 and 25GPa . It confirms changes in the nearest neighborhood of Si atoms for pressures above 5GPa and the permanent change for the sample decompress from 25GPa . It has been reported from experiments[246], that the coordination number at 27GPa was calculated to be 5, which is consistent with the results from Fig. 4.18. The authors of that study suggest that it is difficult to judge whether silica glass has a mixed state of fourfold- and sixfold-coordinated structures or a single fivefold-coordinated structure at this pressure. They state however that it is unlikely that fourfold and sixfold-coordinated structures coexist and the transformation from a fourfold to a sixfold-coordinated structure may not be of first-order [246].

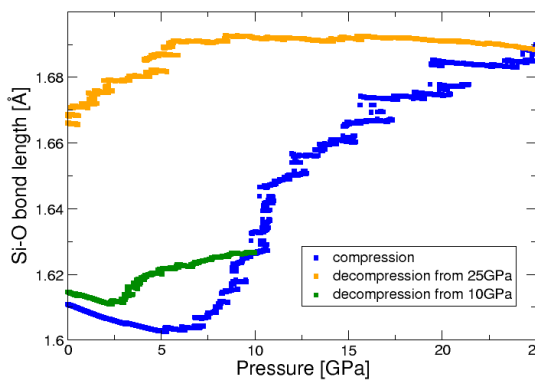


FIGURE 4.19: Bonds lengths between Si and O atoms in function of the applied pressure for quasistatic compression and decompression from 10 and 25GPa

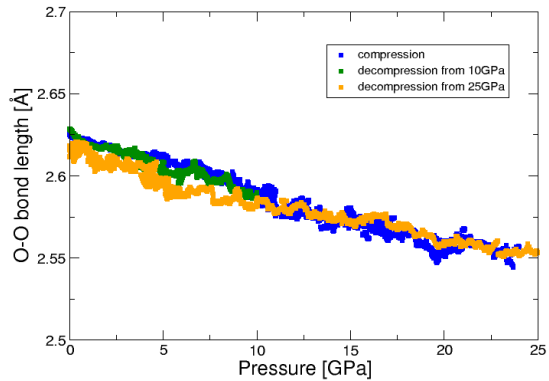


FIGURE 4.20: Bonds lengths between oxygen atoms in function of the applied pressure for quasistatic compression and decompression from 10 and 25GPa .

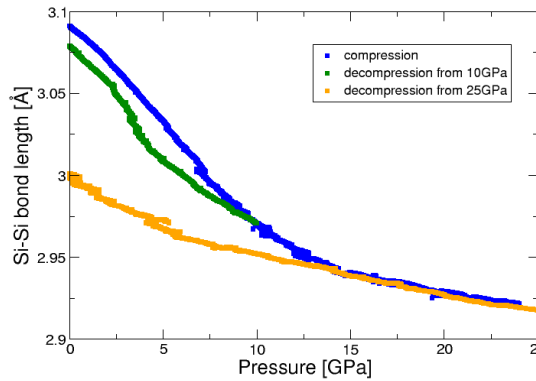


FIGURE 4.21: Bonds lengths between silicon atoms in function of the applied pressure for quasistatic compression and decompression from 10 and 25GPa

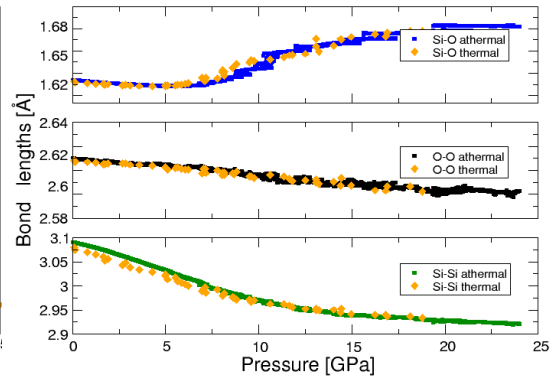


FIGURE 4.22: Comparison of the bonds lengths between atoms obtained from athermal compression (squares) and deformation at 1200K (diamonds).

The calculated $Si - O$ nearest distances as a function of pressure are shown in Fig. 4.19. In agreement with experiments [233, 246], as a result of elastic compression there is a slight initial shortening of the $Si - O$ distance to 1.60\AA . Then, above $10 - 12\text{GPa}$ this distance increases abruptly, reaching 1.69\AA at 25GPa . This lengthening is expected since to accommodate extra oxygen into the first Si coordination shell, the distances between oxygen and silicon atoms have to elongate. This result is in good agreement with the literature as well [246]. When decompressed from 10GPa , the $Si - O$ bonds lengths are almost restored, whereas for the sample decompressed from 25GPa , the distances remain about 0.06\AA longer, which is in accordance with the increase of coordination number at ambient pressure for the same sample.

The bonds between oxygen atoms get shorter under compression (see Fig. 4.20), from 2.62\AA to 2.55\AA at the highest pressure applied. This is due to increased number of this type of atoms around a given silicon. The $O - O$ bonds are least affected when comparing high density amorphous phases at ambient pressure to the initial sample before compression, with a difference not exceeding 0.03\AA . The distances between silicon atoms decrease from 3.1\AA to 2.92 at 25GPa (see Fig. 4.21). It is a result of changes observed in the $Si - O - Si$ angle, which brings silicons closer to each other. In case of these bonds, the irreversible changes are more pronounced when decompressed to ambient pressure from 25GPa , with the difference in the length reaching 0.1\AA .

To characterize the structure of a network on the intermediate length scale we considered the distribution of rings of a given size, as was done for as-quenched samples presented earlier in this chapter.

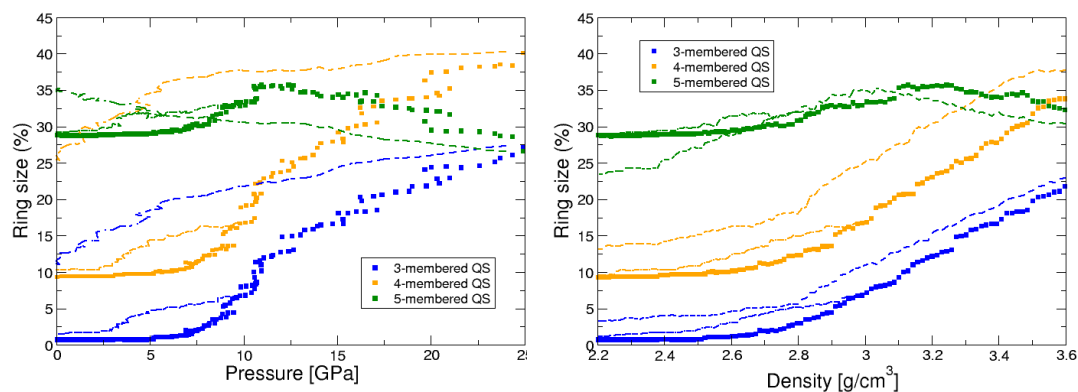


FIGURE 4.23: Distribution of 3-, 4- and 5-membered rings in function of pressure (left) and density (right) for quasistatic compression (squares) and decompression from 10 and 25 GPa (solid and dashed lines, respectively).

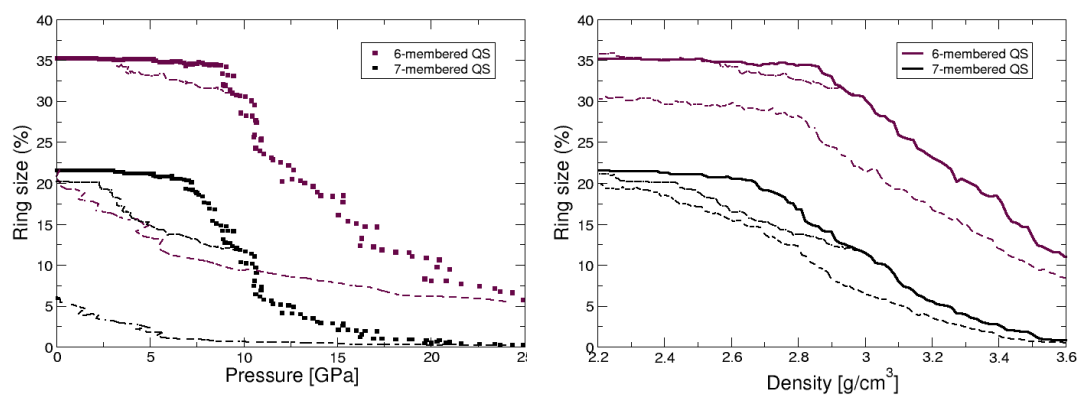


FIGURE 4.24: Distribution of 6- and 7-membered rings in function of pressure (left) and density (right) for quasistatic compression (squares) and decompression from 10 and 25 GPa (solid and dashed lines, respectively).

Figures 4.23 and 4.24 depict the frequency of the most abundant rings in amorphous silica and their evolution with increasing pressure and density (left and right graphs of each figure, respectively), as well as the changes in the distributions when the samples were decompressed quasi-statically from 10 (solid lines in each figure) and 25 GPa (dashed lines). Usually, the ring sizes considered in the studies range from 3 to 8-membered ones, since for better relaxed glasses the number of small and big rings decreases and rings with 9 $Si - O$ segments are rarely present. In

case of 2-membered rings, they are also sparse and mostly omitted in search, because they are associated with edge sharing tetrahedra and as stated before, the density of glasses prepared at low cooling rates decreases due to tetrahedra moving away from each other, which reduces the probability of edge sharing. Depending on the ring size, the frequency rises between 5 and 8 GPa for the shortest rings and decreases for the 6- and 7-membered ones. This may be a consequence of increasing the coordination number of *Si* atoms and decreasing of inter-tetrahedral angles. Higher density and therefore less space for atoms to rearrange hinders the formation of larger rings. It was suggested by experimental analyses [237, 238, 247] that the increase in the fraction of 3- and 4-membered rings is associated with the shifts of D_2 and D_1 "defect" bands in Raman spectrum of glassy SiO_2 . The intensity of these bands are enhanced on compression above 8 GPa. Below this value the observed shifts are fully reversible [237]. It was also reported that above 30 GPa the D_2 band, corresponding to breathing modes of three-membered rings, broadens rapidly and loses its intensity, which could suggest that at very high pressures the formation of very small rings (2-membered or edge sharing tetrahedra) is possible [247]. In this study we have not reached such high pressures and the rings distribution has not been investigated for pressures larger than 25 GPa. The fraction of small rings rises most steeply between 8 and 15 GPa, which is consistent with changes of coordination number of silicon atoms and the decrease of $Si-O-Si$ angle. For higher pressures the rise is less abrupt reaching eventually 30 and 40% in case of 3- and 4-membered rings, respectively. Rings of larger sizes show a decreasing trend for the same range of pressures, with an exception in case of 5-membered rings. Their number increases between 8 and around 13 GPa and then slowly goes down for larger pressures and densities. After unloading from 10 GPa (solid thin lines in both figures) the ring distributions were almost completely restored. Similar effect was observed in coordination numbers, as presented earlier. This is because the densification after decompression from 10 GPa remains limited (the density is equal to $2.31 g/cm^3$) and the structure is not strongly affected. As for the configuration unloaded from 25 GPa, its structure differs significantly from the initial one. The density at ambient pressure is $3.03 g/cm^3$ and this is reflected in the abundance of 3- and 4-membered rings (12 and 25%). Below this density, the pressure in the glass becomes negative, but even then when the initial density is restored, the initial ring structure is not recovered. At $3.03 g/cm^3$, the fraction of 6-membered rings, the most frequent ones in the uncompressed sample, is reduced by 15%. By the same value decreases

the frequency of the 7-membered rings. The configuration decompressed from 25GPa can be regarded as a true, distinct amorphous phase of silica glass.

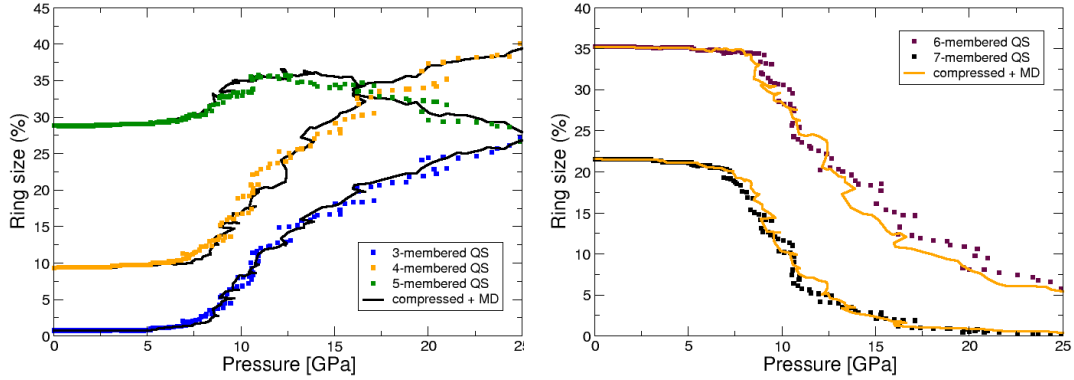


FIGURE 4.25: Distribution of all rings sizes in function of pressure for quasi-static compression (squares) and deformation at constant strain rate (black solid lines for smaller and orange solid lines for larger rings).

As mentioned before, one of the methodologies to obtain pressurized configurations of amorphous silica was compression at constant strain rate and constant temperature of 1200K . The comparison of rings distributions for these two techniques is presented in Fig. 4.25. One can easily notice that the evolution of ring sizes both for small (in black in the left graph) and large rings (in orange in the right graph) are the same, showing only negligible differences with pressure as those obtained through quasi-static deformation.

Potential energy landscape of high density amorphous phase.

As pointed out above, the configuration decompressed from 25GPa can be regarded as a true, distinct amorphous phase of silica glass. With this in mind, we wanted to investigate the nature of the thermally-activated processes occurring in this phase. The search for the activated states was performed the same way as in case of the reference configuration ($2.20\text{g}/\text{cm}^3$, lowest cooling rate), namely using the activation-relaxation technique. In order to sample the potential energy landscape around the initial equilibrium, a number of Si and O atoms within a radius $X_{range} = 4.0\text{\AA}$ from a given atom were displaced along a random direction. The efficiency of the search was slightly lower than in case of the reference configuration, but only by around $5 - 7\%$, which is still satisfactory, bearing in mind that the search was performed using many cores.

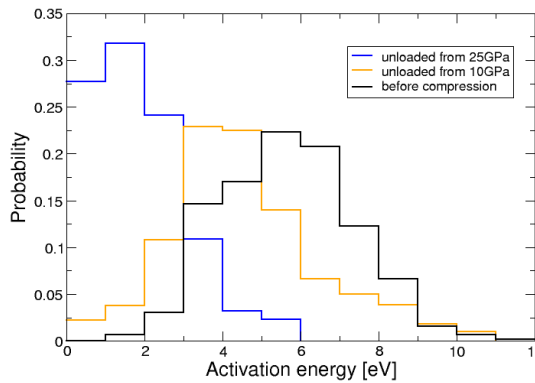


FIGURE 4.26: Distributions of activation energies for quasistatic compression and decompression from 10 and 25GPa

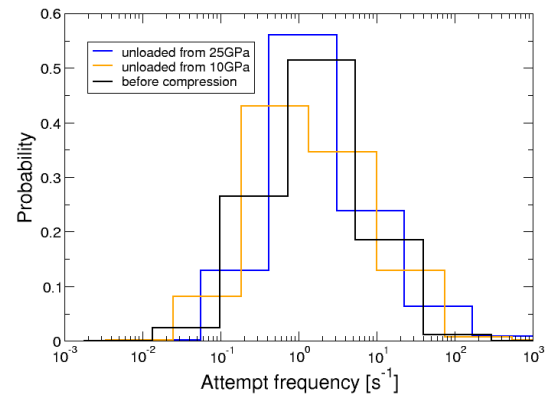


FIGURE 4.27: Distributions of attempt frequencies for quasistatic compression and decompression from 10 and 25GPa

The distributions of activation energies and attempt frequencies were obtained from more than 1000 distinct activated states and are presented in Fig. 4.26 and 4.27. Activation energies (Fig. 4.26) show a trend of shifting towards lower values with increasing pressure the configurations were subject to before unloading (shown in orange and blue). This is a consequence of plastic, irreversible deformations of the glass structure and has also been observed in metallic glasses [12]. The distributions have an usual shape and one is able to indicate the most probable value of activation energy.

Figure 4.27 presents the distributions of attempt frequencies for configurations decompressed from 10 (in orange) and 25GPa (in blue) and compared to those of the reference sample. In all cases the frequencies span over the same range (4 – 5 orders of magnitude), but no clear trend and significant differences between the distributions can be pointed out. Similar effect was observed for as-quenched amorphous silica presented earlier in this chapter. As in case of metallic glasses and as-quenched silica glasses the relation between the activation energy of a thermally-activated event and its attempt frequency was considered for the different amorphous phases of SiO_2 . The obtained results are depicted in Fig. 4.28. For the sake of clarity, only the reference sample (in orange) and the one unloaded from 25GPa are presented. The results reflect the differences observed in the distribution of activation energies, where the density of low energy saddle points of the sample decompressed from 25GPa was higher than that of the reference

configuration. The shapes and trends of the relation in Fig. 4.28 are similar for both phases, namely the attempt frequencies tend to shift very slightly towards higher values with increasing activation energies (which is in line with the Meyer-Neldel compensation rule). The Pearson's product-moment correlation coefficient increases for the configurations decompressed from high pressures and is equal to 0.43 for the configuration shown in blue (0.37 for the reference phase).

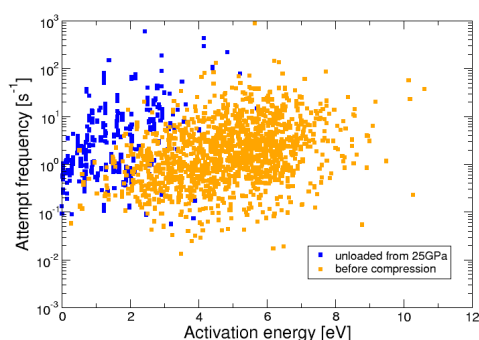


FIGURE 4.28: Relation between activation energy and attempt frequency for thermally activated transitions in different amorphous phases of silica glasses.

between them, which leads to breaking bonds and changes in the local distribution of rings. In all cases, only one *Si* atom moves significantly (in as-quenched silica glasses usually two of them were active in each transition, when more than one atom was chosen to be displaced in order to search for saddle points).

The nature of thermally-activated events in high density amorphous phases is similar to those observed in silica glasses before compression. For low energy activated states, the transitions correspond to *Si* atoms slightly rotating with its neighboring oxygens or their very small displacement without affecting the short-range structure. For higher activation energies, silicon atoms displace more, often dragging their nearest oxygens or pushing be-

Vibrational density of states of LDA and HDA phases.

The last quantity that has been investigated in this study was the vibrational density of states of different amorphous phases, that we obtained during our research. This quantity gives and insight into their dynamical behavior.

The eigenfrequencies were computed by diagonalizing the dynamical matrix for each considered configuration. Fig. 4.29 shows so-obtained distribution. In case of the reference sample (in black) as well as the sample decompressed from 10GPa (in orange), the distribution has two main features. The first one is a double peak at high frequencies and the second one is a broad mountain at intermediate and low frequencies. The distributions of the reference phase and the sample unloaded

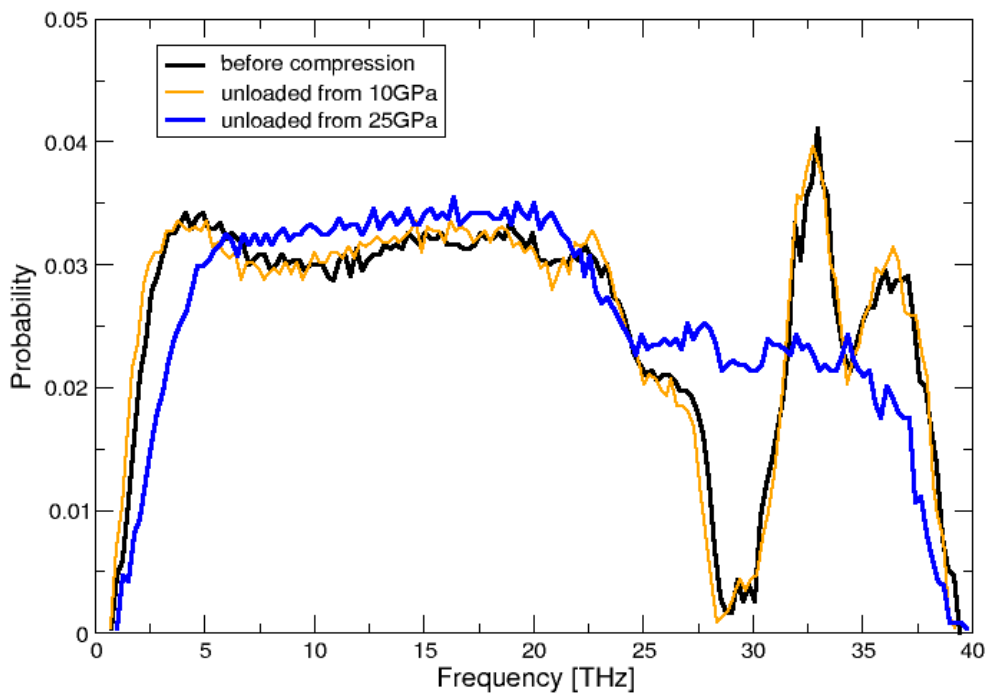


FIGURE 4.29: Vibrational density of states for different amorphous phases of silica.

from 10GPa basically do not differ. As was shown before, their structures after decompression of the latter are very similar and therefore the dynamics is not influenced either.

The double peak at high frequencies was associated with the breathing modes of tetrahedra and is mostly due to oxygen atoms [141, 248]. It was shown [141], that these two peaks are sensitive to the cooling rate. For silica glasses quenched more slowly their height significantly increases and the gap between them tends to decrease. As mentioned before, for better relaxed glasses, the tetrahedra move away from each other, lowering the density of the system, which allows that bigger number of them contributes to the rise of the peaks at approximately 33 and 37THz . The location and shape of these two peaks agrees well with experiments suggesting that the vibrational properties of the simulated glass seem to be closely related to that of the real material [141, 249].

The distribution at low and intermediate frequencies doesn't reproduce the experimental one so well. It is probably due to the fact that in this frequency range

most of the modes involve the movement of several particles, thus they extend over larger region of space and the BKS potential is not able to reproduce correctly the forces on the intermediate range distances.

The vibrational density of states obtained for the configuration unloaded from 25GPa is significantly different from the one of the reference system. First of all it doesn't contain the double peak present for the latter at high frequencies. This is a consequence of the breakdown in the intermediate range order. In high density amorphous phase of silica the tetrahedral structure is largely destroyed and the sample contains lots of defects, 5- and 6-fold coordinated silicon atoms. Since the number of normal modes needs to be conserved, the changes in the structure result in filling the gap present in the reference system at around 30THz . At low frequencies, the shift towards higher values can be noticed. This can be associated with the permanent densification of the system decompressed from 25GPa .

4.2.1 Comparison with as-quenched silica glasses

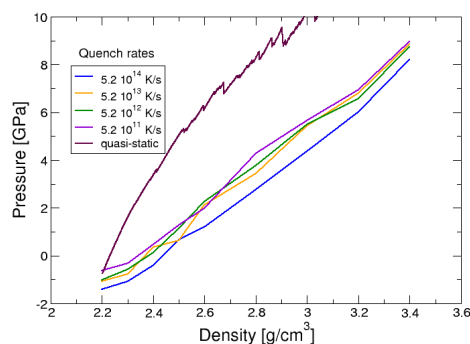


FIGURE 4.30: Relation between pressure and density for quasi-statically compressed and as-quenched silica glasses.

Figure 4.30 presents a relation between pressure and density for the silica glasses quenched at constant volume and those compressed hydrostatically. From the figure one can easily notice that the pressure increases much more rapidly in the deformed glasses than in the as-quenched glasses, reaching 4GPa already for the density of 2.40g/cm^3 (as-quenched glasses reach this pressure at around 2.80g/cm^3 for the best relaxed sample). This is understandable since as-quenched glasses were slowly relaxed at finite temperature, which released the stresses in the system, while quasi-statically deformed glasses are purely mechanically driven, without a thermal relaxation.

Figures 4.31, 4.32, 4.33 and 4.34 show a geometrical characterization of the deformed and as-quenched silica glasses in terms of coordination number of silicon atoms. Both the changes in a particular number of oxygen neighbors and average

coordination number show the same property – as quenched and deformed glasses are almost identical at a given density. The difference between the glasses is visible when comparing the pressure at which the structural changes start. Since the pressure in as-quenched glasses is much smaller than in the deformed glasses, the short-range transitions occur at much smaller pressures in the glasses quenched at constant volume.

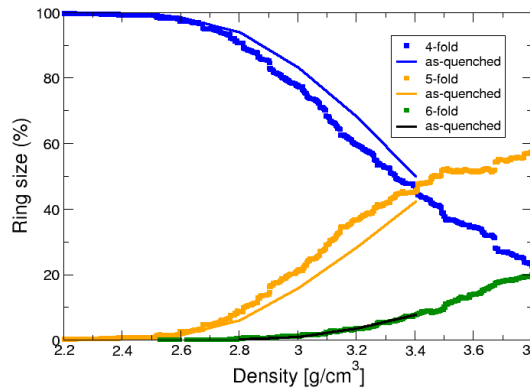


FIGURE 4.31: Evolution of coordination number as a function of density for deformed glasses (squares) and as-quenched glasses (solid lines).

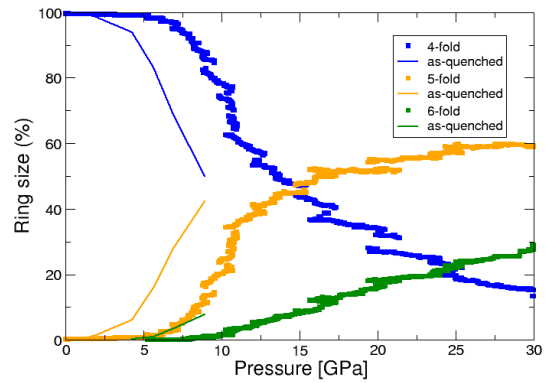


FIGURE 4.32: Evolution of coordination number as a function of pressure for deformed glasses (squares) and as-quenched glasses (solid lines).

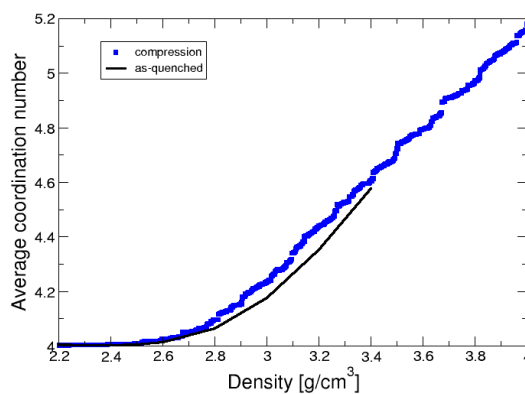


FIGURE 4.33: Average coordination number as a function of density for deformed glasses (squares) and as-quenched glasses (solid line).

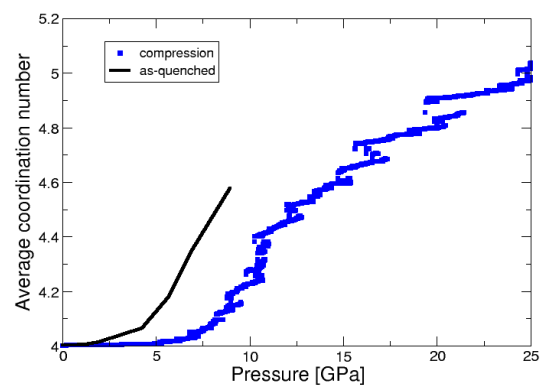


FIGURE 4.34: Average coordination number as a function of pressure for deformed glasses (squares) and as-quenched glasses (solid line).

The changes of the coordination number of Si atoms in the as-quenched glasses begin approximately at $3GPa$, whereas in the case of deformed glasses these changes start above $5GPa$. From this pressure the differences between the glasses are even more pronounced, reaching around 35% for the 4- and 5-fold coordination numbers at $7 - 8GPa$. One can also notice that in the as-quenched glasses the sixfold coordinated silicon atoms can be found for lower pressures than in the deformed systems.

The differences in the short-range order between the as-quenched and deformed systems can be also seen in the bond lengths between the silicon and oxygen atoms as presented in Fig. 4.35 and 4.36 below.

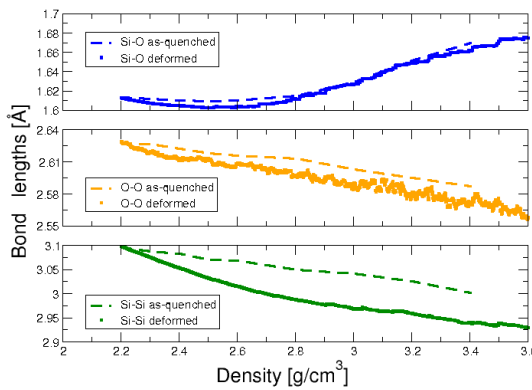


FIGURE 4.35: Bond lengths as a function of density for deformed glasses (squares) and as-quenched glasses (dashed lines).

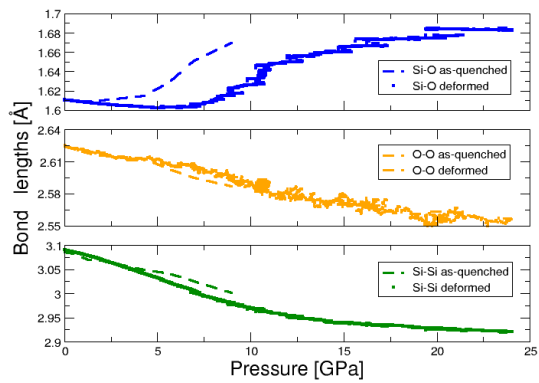


FIGURE 4.36: Bond lengths as a function of pressure for deformed glasses (squares) and as-quenched glasses (dashed line).

As observed in the case of the coordination number of silicon atoms here the bond lengths are almost identical at a given density for both types of systems. The only noticeable difference is present for $Si - Si$ bonds, that are on average longer in the case of the decompressed glasses. This is due to the thermal relaxation the as-quenched samples were subject to during preparation. Their structure is more ordered and the polyhedra forming the network are more distant from each other. The changes between the as-quenched and decompressed systems are more visible when the bond lengths are related to the pressure. The $Si - O$ bonds start to increase above $3GPa$ in the as-quenched glasses, which corresponds exactly to the starting point of the increase in the number of oxygen neighbors for these configurations. Although the bonds are longer for lower pressures in as-quenched

glasses, the slope of this change is similar when the pressure in the deformed systems exceeds 8GPa , which was also observed in the evolution the coordination number. There is no noticeable difference between $O - O$ and $Si - Si$ bonds as a function of pressure.

Similarly to the short-range order, the changes in the medium-range order, characterized by the distributions of rings of different sizes, also occur at much smaller pressures in the as-quenched glasses than in the deformed glasses.

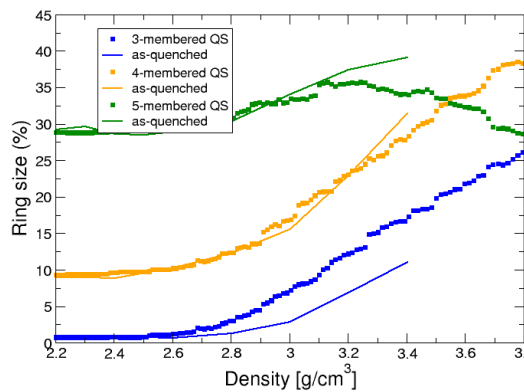


FIGURE 4.37: Evolution of small ring sizes as a function of density for deformed glasses (squares) and as-quenched glasses (solid lines).

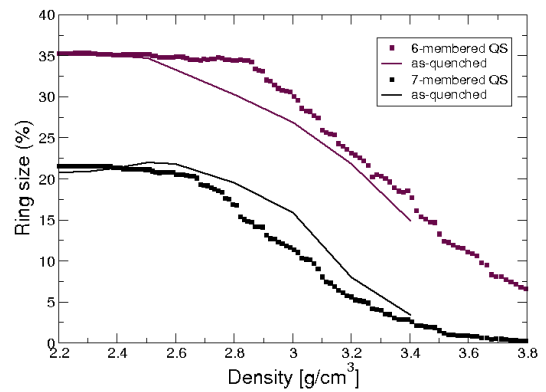


FIGURE 4.38: Evolution of small ring sizes as a function of pressure for deformed glasses (squares) and as-quenched glasses (solid lines).

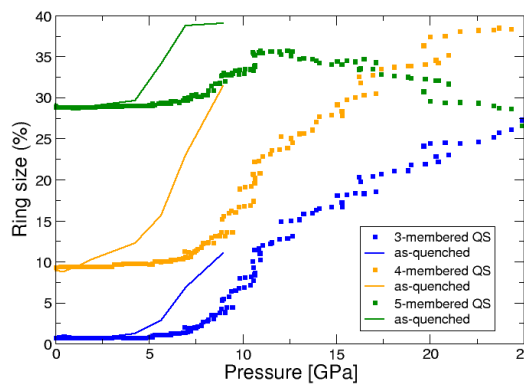


FIGURE 4.39: Evolution of small ring sizes as a function of density for deformed glasses (squares) and as-quenched glasses (solid lines).

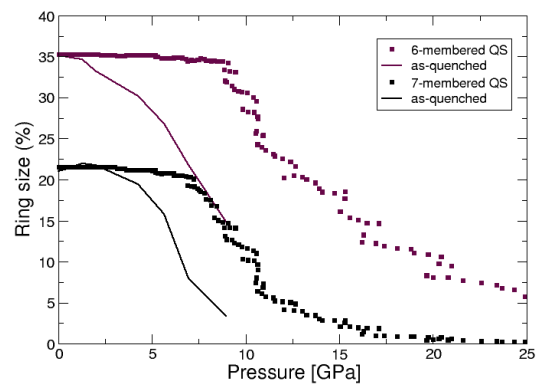


FIGURE 4.40: Evolution of small ring sizes as a function of pressure for deformed glasses (squares) and as-quenched glasses (solid lines).

Figures 4.37, 4.38, 4.39 and 4.40 depict the evolution of the ring sizes as a function of density and pressure. As noticed in the short-range structure, the ring distributions are almost the same for the as-quenched and deformed glasses when plotted as a function of density. Small deviations are present for 3-membered rings for densities above 2.8g/cm^3 and for 6- and 7-membered rings, but these differences are negligible since they do not exceed 4% (Fig. 4.37 and 4.38). When the ring distributions are related to the pressure, the changes start, depending on the size of a ring, around $2 - 3\text{GPa}$. Small-size rings, 4- and 5-membered, become more numerous by approximately 20 and 10%, respectively in the case of as-quenched glasses at the pressure around 7GPa . For the decompressed glasses, the 6-membered rings are still most abundant, whereas for the glasses quenched at constant volume their fraction drops to 20%.

The comparison of the deformed and as-quenched glasses presented above can suggest that one can prepare two glasses with the same density and the same geometrical characteristics but widely different pressures and energies. The coordination number, $Si-O-Si$ angle and distribution of rings seem to be not sensitive enough to distinguish between these low and high pressure configurations. Also, if we relax a deformed glass at finite temperature and constant density, its pressure and density will decrease and will probably tend to the as-quenched pressure and density. What rearrangements would take place that decrease the pressure and energy without changing the short- and medium-range order remains an open question.

4.2.2 Comparison with experiments

As shown in experiments, above 10 GPa, silica glasses enter a plastic regime marked by permanent densification after decompression [228, 237, 250]. The densification increases gradually with the maximum applied pressure and saturates at about 20 % beyond 25 GPa [251]. Based mainly on Raman spectroscopy measurements [247, 252], densification was shown to occur through an alteration of the medium range order (MRO) in the glass. The MRO can be characterized by the size distribution of rings and densification was shown to be marked by an increase in the population of small three- and four-membered rings and a decrease in larger rings [237, 238]. Concomitantly, the inter-tetrahedral angle $\theta_{Si-O-Si}$ decreases [237]. In analogy with crystalline polymorphism [228], this pressure-induced transition has been described as an evidence of polyamorphism in silica

glasses, the densification corresponding to a progressive transformation from a low-density amorphous (LDA) phase to a high-density amorphous (HDA) phase of silica. We should note however that the mechanism relating densification to the change of MRO is not clear to this date. Also, x-ray diffraction measurements have evidenced a second structural transition, which affects the short-range order (SRO) in the glass, i.e. the Si-O coordination number. Through the transition, Si atoms see their number of first neighbor O atoms increase from 4 to 6, such that the tetrahedral structure observed at ambient pressure is transformed into an octahedral structure [244, 253]. In contrast with the MRO transition which is irreversible upon decompression, this second transition has been found reversible experimentally, i.e. after decompression, the densified glass contains only fourfold coordinated Si atoms. The pressure range over which this transition occurs and its potential overlap with the MRO transition are matters of debates [244, 245, 253, 254]. In atomistic simulations, both MRO and SRO transitions occur simultaneously and are often assimilated with one another [255–259], while experimentally, a range of pressures has been reported. An increase in coordination number causes an increase in the Si-O bond length and early x-ray diffraction measurements showed a constant bond length up to at least 8 GPa [241]. More recently, transitions were reported from 15 GPa [233] or above 20 GPa [229, 253], thus showing that the SRO transition occurs at higher pressure than the MRO transition. However, using x-ray Raman scattering [260], the SRO transition was found to start at around 10 GPa and to end at around 25 GPa, thus fully overlapping with the MRO transition.

We should note that both numerically and experimentally, most works focus either on the SRO or on the MRO and rarely are both discussed together. In particular in experiments, MRO and SRO transitions are studied using different techniques that provide different information, vibrational modes for Raman spectroscopy and structure factor for x-ray diffraction. Since depending on the reference, the pressure ranges of the transitions may or may not overlap, it is not clear if both transitions are not the two faces of a single structural transformation. We can understand intuitively that an increase in the coordination number increases the proportion of short rings, but the ring size can decrease by atomic rearrangements without altering the coordination. It remains however that experimentally, the SRO transition is reversible upon decompression [251] while the MRO transition is irreversible.

As stated above, the MRO and SRO transitions in the simulations happen at

the same time and the SRO transition is irreversible. This means that in the simulations, the HDA phase is characterized by an increased proportion of small rings, a decreased Si-O-Si angle as well as an increased coordination number, whereas experimentally the HDA phase is fourfold, like the LDA.

The irreversible increase in coordination number in our simulations comes primarily from fivefold coordinated atoms that represent 35 % of the Si atoms after decompression from 25 GPa. This irreversibility may be an artifact of the numerical models, which in most cases treat the electronic structure of the glass in a very simplified way. More first-principles calculations [245] would be required to answer this question. They could also answer another question related to the fact that numerical glasses after compression and decompression contain fivefold coordinated atoms while experimentally, Si atoms seem to be either four- or six-fold coordinated [260]. If for some electronic structure reason, fivefold coordinated Si atoms were energetically high unfavorable, as experimental data seem to infer [260], we would recover the reversibility of the SRO transition. Would that also affect the equivalence between SRO and MRO upon compression seen in the simulations? This remains an open question that would be extremely interesting to answer.

Compared to the experiments, we should note also that the plastic regime starts at a lower pressure, close to 5 GPa in the deformed glasses and close to 2 GPa in the as-quenched glasses. This discrepancy is probably partly due to the level of relaxation of the glasses, which remains limited compared to the experiments, but it could also be another consequence of our highly simplified energetic model.

The objective of the study presented in this chapter was to investigate thermally-activated processes in silica glasses and check if the BKS potential can reproduce the amorphous–amorphous transition observed in experiments at high pressures.

The obtained results on thermally-activated transitions show that one can distinguish two types of these events. One, when only oxygen atoms are involved (exchanging sites with other oxygens around the same silicon atom or jumping between few silicons, but with no changes in the local structure), and second, when silicons rearrange more, what leads to changes in the local intermediate range order (breaking rings and forming new ones). The activated energies show the same trend as in case of metallic glasses, shifting towards higher values for better relaxed configurations. The attempt frequencies span over 4–5 orders of magnitude

and seem to be insensitive to cooling rate. As opposed to metallic glasses, they tend to increase with increasing activation energies, satisfying the Meyer-Neldel compensation rule.

The polyamorphism observed in experiments could be reproduced using the BKS potential. It was shown here in terms of coordination number of silicon atoms, rings distribution and distances between all types of atoms, that the elastic, reversible regime ends around $7 - 8\text{GPa}$ (first permanent densification that could be observed), which is close to experimental results. The first structural changes (coordination number, increase in small rings) start at around 5GPa and, as mentioned above, this not what was observed in experiments. Accounting for the fact that the BKS potential contains only two-body terms and the level of relaxation of the simulated glasses is much lower than in experiments, which decreases the elastic limit, it outlines well the properties of silica glasses, even with the Wolf truncation applied here.

SUMMARY AND PERSPECTIVES

This thesis was strictly numerical. The idea behind it was to predict the thermally activated kinetics in glasses such as those encountered experimentally. The nature of such microscopic events occurring in disordered systems was studied both under mechanical stress and in ageing conditions.

As stressed many times throughout this study, the thermally-activated processes are ubiquitous in the structural relaxation and deformation of glasses at low temperatures. Unfortunately, they take place over timescales long compared to those accessible to direct Molecular Dynamics simulations. In this thesis we attempted to characterize the thermally-activated events employing methods that let us exceed these timescales. The most widely used here was the Activation-Relaxation Technique. It was applied to search for saddle points on the potential energy landscape of two types of glasses: metallic and silica glasses. We proved that this method is able to identify enough activated states to build statistically relevant samples, from which stationary distributions can be computed. Nevertheless, it still has its downsides. We found that ART searches are biased towards higher activation energies and it is hard to find energies below $1.5 - 2.0\epsilon_{AA}(eV)$ in case of the best relaxed glasses. To cover the range of the energies missed by ART, other methods were applied, such as Nudged Elastic Band (NEB) combined with Molecular Dynamics and Autonomous Basin Climbing (ABC). The saddles obtained by applying MD+NEB showed that the activated states visited by the simulated system during its time evolution lie within the lower range sampled by the ART calculation. The problem of ART is that the density of states found in this range of energies is low. Another drawback of this method is its efficiency. It was never higher than 25%, but the efficiency became less important when it

was implemented to work within OpenMP parallel computing method. Dividing most time consuming operations in each search among many threads allowed to find more than 1000 distinct saddle points for 4000-atom metallic glass system and 3000-atom silica glass system in less than 72 hours, which is a satisfactory result. Therefore it is safe to conclude that thermally-activated transitions can be sampled with ART efficiently enough and other methods presented in this thesis may be used to confirm trends found by ART.

To characterize a thermally-activated process we investigated two quantities: activation energies and attempt frequencies. Since in the definition of an attempt frequency the curvature of the initial minimum and the saddle point are present, we wanted to see if there was a relation between attempt frequencies and activation energies of a given event. Such correlation had been observed before for a wide range of phenomena and is referred to as the Meyer-Neldel compensation rule. We confirmed the simple picture of the potential energy landscape, showing that glasses quenched more rapidly have higher density of low energy saddle points (wide distributions of activation energies shift towards higher energies in better-relaxed glasses). As for attempt frequencies, we found that for metallic glasses these prefactors are distributed over a range of almost ten orders of magnitude, in stark contrast with the common assumption that they are given by a typical vibrational frequency. For silica, these ranges are narrower, but still span over 4 – 5 orders of magnitude. The relation between activation energies and attempt frequencies was found to be inverse to the Meyer-Neldel compensation rule in case of metallic glasses within the harmonic approximation of the transition state theory. However, when combined with a multiple-hop analysis that takes into account the multiplicity of possible transitions, a direct Meyer-Neldel behavior is recovered.

Although the ranges of activation energies and attempt frequencies are wide, we showed that the dynamics at low temperatures is controlled by the lowest energy transitions, which have high frequencies close to the Debye frequency, which justifies a posteriori the usual assumption of a single attempt frequency.

Investigating the molecular dynamics trajectories of metallic glass systems we found that the escape from a metabasin does not happen by a single barrier crossing between two long-lived minima, but rather through a number of short-lived intermediate states. The number of these states ranges from a few to over a

hundred.

Apart from thermally-activated states, we also focused on the short and medium range order of glasses. They were characterized using two methods: Voronoi tessellations for metallic glasses, providing us information about near neighbor conformations, and in case of silica, statistics of ring distributions. We confirmed that in case of metallic glasses the level of relaxation is closely connected with the fraction of icosahedra formed in the structure. For better relaxed samples, this fraction increases, reaching almost 13% for the systems quenched at the lowest cooling rate. This dependency though works only with the Wahnström potential and cannot be observed for the Kob-Andersen systems.

The results obtained for silica glasses show that one can distinguish two types of thermally-activated events. One, when only oxygen atoms are involved (exchanging sites with other oxygens around the same silicon atom or jumping between few silicons, but with no changes in the local structure), and second, when silicons rearrange more, which leads to changes in the local intermediate range order (breaking rings and forming new ones). The activated energies show the same trend as in case of metallic glasses, shifting towards higher values for better relaxed configurations. As mentioned above, the attempt frequencies span over 4 – 5 orders of magnitude and seem to be insensitive to cooling rate. As opposed to metallic glasses, they tend to increase with increasing activation energies, satisfying the Meyer-Neldel compensation rule.

The silica glasses were also investigated to answer if the simple BKS potential without Ewald summation is able to reproduce polyamorphism observed in silica glasses subject to hydrostatic compression. To achieve that we looked mainly at the coordination number of silicon atoms and the distribution of rings. Accounting for the fact that the BKS potential contains only two-body terms and the level of relaxation of the simulated glasses is much lower than in experiments, which decreases the elastic limit, it outlines well the properties of silica glasses, even with the Wolf truncation applied in this dissertation. Nevertheless questions remain concerning the change of coordination number upon decompression which is found irreversible in the simulations while it is reversible in experiments.

Although a lot has been done in this study, there are still many questions to be answered. As stated in Chapter 2 when describing the intermediate, short-lived

states visited by a system during its escape from an initial metabasin, one needs more insightful characteristics of these states, based on a richer set of data. This could be performed on a bigger system to see how the fraction of broken bonds depends on the distance between two equilibrium states that lie close to each other in the configuration space. The trend observed for the angle between the exit point from an initial long-lived state and the entry point to a final minimum would also be clearer. The entropic nature of the transitions at low temperature, which involve a large number of short-lived states, should also be investigated in more details.

The short-range order of metallic glasses was investigated only for the Wahnström system. As emphasized above, a trend of increasing fraction of icosahedra on the level of glass relaxation was reported. This study could be extended to systems modeled with Kob-Andersen potential. Although we found that the level of relaxation is not indicated by the number of icosahedra, we could check if polyhedra around atoms form regular structures at intermediate length scales and if we can attribute such structures to the cooling rate applied to prepare a glass.

The extensive investigation of thermally-activated processes that lead to plastic deformations revealed their interesting properties, that were pointed earlier in this section. Nevertheless it is still hard to predict what properties of the system make particular regions more prone to such transformations. It would be interesting to focus on this aspect in the future. One would also need new/modified numerical tools to make the search for activated states less expensive. It could be achieved by finding a way to improve the efficiency of the Activation-Relaxation Technique. Unfortunately we haven't been successful yet in increasing the ratio of saddle points found on the potential energy landscape to the number of attempts performed. Another question is if even within kT_C exhaustive sampling is possible. We showed that in the case of metallic glasses the anharmonic Meyer-Neldel rule is not met within the harmonic approximation of the transition state theory. Can anharmonicity be introduced to restore this rule? It is another open question.

The most important aspect concerning silica glasses to be focused on in the future would probably be the differences between the simulations and the experiments. One should make an effort to improve energetic models of SiO₂ and account for the electronic structure of the atoms. Perhaps it would be enough to see the short

and medium range order change at different pressures when compressing a system hydrostatically. We also show that the classical quantities used to characterize changes in the silica glass structure, i.e. coordination number, ring distributions and Si-O-Si angle, are not sensitive enough to distinguish between configurations quenched at constant volume and those deformed quasi-statically. The observation of the rearrangements occurring when the deformed samples are subject to finite temperature relaxation would be a good starting point for such study. One main subject that is left for future study is how to prepare better-relaxed glasses whose structure could be better compared to experimental glasses. This is still a fully opened question.

In all cases one should find a way to prepare better relaxed glasses. The quench rates used in simulations are higher by around 12 orders of magnitude as compared to experiments. In order to do that, we used in our work the vapor-deposited glasses (proposed by Prof. Juan de Pablo group—see Chapter 3 for references) and tried to use Parallel Replica Dynamics (PRD). Unfortunately the attempts failed in both cases. Hence, this still remains an open question of prime importance since beyond the question of the realism of the interatomic potential, the difference in levels of relaxation between numerical and experimental glasses limits the possibility of comparison between simulations and experiments.

BIBLIOGRAPHY

- [1] J.F. Loeffler. *Intermetallics*, 11:529, 2003.
- [2] M. Telford. *Materials Today*, 7:36, 2004.
- [3] USB drive case made of metallic glass, <http://allthatmatters.heber.org/tag/metallic-glasses/>.
- [4] Golf clubs made of metallic glass, http://web.ornl.gov/info/ornlreview/v38_1_05/article17.shtml.
- [5] M. Malekan, S.G. Shabestari, W. Zhang, S.H. Seyedein, R. Gholamipour, K. Yubuta, A. Makino, and A. Inoue. *Materials Science and Engineering: A*, 553:10, 2012.
- [6] E. Pekarskaya, C. P. Kim, and W. L. Johnson. *Journal of Materials Research*, 16:2513, 2001.
- [7] Scanning transmission electron microscopy, <https://www.engr.wisc.edu/news/archive/2012/May11.html> .
- [8] Nowosielski and R. Babilas. *Journal of Achievements in Materials and Manufacturing Engineering*, 37:332, 2009.
- [9] Jingwei Liu Lianyi Chen Xiaodong Wang J.Z. Jiang Qingping Cao, Feng Xu. *J. Mater. Res.*, 24:2924, 2009.
- [10] FEM and icosahedral structure of metallic glasses, <http://monash.edu/news/show/new-experiment-opens-window-on-glasses> .

- [11] Scanning tunneling microscopy, http://en.wikipedia.org/wiki/Scanning_tunneling_microscope.
- [12] D. Rodney, A. Tanguy, and D. Vandembroucq. *Modelling and Simulation in Materials Science And Engineering*, 19:083001, 2011.
- [13] Exploring potential energy landscape, http://www.engr.ucsb.edu/~shell/che210d/Exploring_the_energy_landscape.pdf.
- [14] Periodic boundary conditions, <http://www.ncbi.nlm.nih.gov/pmc/tools/openftlist/>.
- [15] Ting Zhu, Ju Li, and Sidney Yip. *Atomistic Reaction Pathway Sampling: The Nudged Elastic Band Method and Nanomechanics Applications*. John Wiley & Sons, Ltd, 2013.
- [16] Alessandro Laio and Michele Parrinello. *Proceedings of the National Academy of Sciences*, 99:12562, 2002.
- [17] Daniel Söpu. PhD thesis, TU Darmstadt, September 2011.
- [18] H. W. Sheng, W. K. Luo, F. M. Alamgir, J. M. Bai, and E. Ma. *Nature*, 439:419, 2006.
- [19] Sébastien Leroux and Philippe Jund. *Computational Materials Science*, 50:1217, 2011.
- [20] A. Bunde, K. Funke, and M.D. Ingram. *Solid State Ionics*, 105:1, 1998.
- [21] F.R. Paturi. *Die Geschichte vom Glas*. 1988.
- [22] R.H. Doremus. *Glass Science*. 1973.
- [23] L.A.B. Pilkington. *Proceedings of the Royal Society of London A*, 314:1, 1969.
- [24] W. Klement, R.H. Willens, and P. Duwez. *Nature*, 187:869, 1960.
- [25] Yan Hui Liu, Gang Wang, Ru Ju Wang, De Qian Zhao, Ming Xiang Pan, and Wei Hua Wang. *Science*, 315:1385, 2007.

- [26] H. Guo, P. F. Yan, Y. B. Wang, J. Tan, Z. F. Zhang, M. L. Sui, and E. Ma. *Nature Materials*, 6:735, 2007.
- [27] H.S. Chen and D. Turnbull. *Acta Metallurgica*, 17:1201, 1969.
- [28] H.S. Chen. *Acta Metallurgica*, 22:1505, 1974.
- [29] M.C. Lee, J.M. Kendall, and W.L. Johnson. *Applied Physics Letters*, 40:382, 1982.
- [30] H.W. Kui, A.L. Greer, and D. Turnbull. *Applied Physics Letters*, 45:615, 1984.
- [31] A. Inoue, T. Zhang, and T. Masumoto. *Materials Transactions JIM*, 30:965, 1989.
- [32] A. Inoue, T. Zhang, T. Masumoto, A. Kato, and S.G. Kim. *Materials Transactions JIM*, 32:609, 1991.
- [33] T. Zhang, A. Inoue, and T. Masumoto. *Materials Transactions JIM*, 32:1005, 1991.
- [34] A. Peker and W.L. Johnson. *Applied Physics Letters*, 63:2342, 1993.
- [35] A. Inoue, N. Nishiyama, and H. Kimura. *Materials Transactions JIM*, 38:179, 1997.
- [36] A. Inoue and A. Takeuchi. *Acta Materialia*, 59:2243, 2011.
- [37] A. Inoue. *Acta Materialia*, 48:279, 2000.
- [38] N. Nishiyama, A. Inoue, and K. Amiya. *Journal of Non-Crystalline Solids*, 353:3615, 2007.
- [39] D.C. Hofmann. *Journal of Materials*, 2013:517904, 2013.
- [40] A.I. Salimon, M.F. Ashby, Y. Brechet, and A.L. Greer. *Materials Science and Engineering A*, 375:385, 2004.
- [41] M.F. Ashby and A.L. Greer. *Scripta Materialia*, 54:321, 2006.

- [42] A. Inoue, B.L. Shen, H. Koshiba, H. Kato, and A.R. Yavari. *Nature Materials*, 2:661, 2003.
- [43] J.J. Lewandowski and A.L. Greer. *Nature Materials*, 5:15, 2007.
- [44] C.A. Schuh, T.C. Hufnagel, and U. Ramamurty. *Acta Materialia*, 55:4067, 2007.
- [45] P. Lowhaphandu and J.J. Lewandowski. *Scripta Materialia*, 38:1811, 1998.
- [46] C.C Hays, C.P. Kim, and W.L. Johnson. *Physical Review Letters*, 84:2901, 2000.
- [47] F. Szuecs, C.P. Kim, and W.L. Johnson. *Acta Materialia*, 49:1507, 2001.
- [48] A Hirata and Y. Hirotsu. *Materials*, 3:5263, 2010.
- [49] Electron diffraction, http://en.wikipedia.org/wiki/Electron_diffraction.
- [50] Transmission electron microscopy, <http://encyclopedia.thefreedictionary.com/Electron+microscope>, http://en.wikipedia.org/wiki/Transmission_electron_microscopy.
- [51] A Hirata, T. Morino, Y. Hirotsu, K. Itoh, and T. Fukunaga. *Materials Transactions JIM*, 48:1299, 2007.
- [52] Y. Hirotsu, M. Uehara, and M. Ueno. *Journal of Applied Physics*, 59:3081, 1986.
- [53] Y. Hirotsu, T. Ohkubo, and M. Matsushita. *Microscopy Research and Technique*, 40:284, 1998.
- [54] Tadakatsu Ohkubo and Yoshihiko Hirotsu. *Physical Review B*, 67:094201, 2003.
- [55] J. Li, L. Wang, and T.C. Hufnagel. *Physical Review B*, 65:144201, 2002.
- [56] A.S. Argon. *Journal of Physics and Chemistry of Solids*, 43:945, 1982.
- [57] F. Spaepen and D. Turnbull. *Scripta Metallurgica*, 8:563, 1974.

- [58] S. L. Montgomery P. Lowhaphandu, L. A. Ludrosky and J. J. Lewandowski. *Intermetallics*, 8:487, 2000.
- [59] A. Inoue. *Intermetallics*, 8:455, 2000.
- [60] P.E. Donovan and W.M. Stobbs. *Acta Metallurgica*, 29:1419, 1981.
- [61] Bright field microscopy, http://en.wikipedia.org/wiki/Bright_field_microscopy.
- [62] R. P. Trivedi T. Lee, B. Senyuk and I. I. Smalyukh. *arXiv:1108.3287*, 2011.
- [63] Dark field microscopy, http://en.wikipedia.org/wiki/Dark_field_microscopy.
- [64] K. F. Kelton and T. W. Wu. *Applied Physics Letters*, 46:1059, 1985.
- [65] C.T. Liu, M.F. Chisholm, and M.K. Miller. *Intermetallics*, 10:1105, 2002.
- [66] S.J. Pennycook, A.R. Lupini, M. Varela, A. Borisevich, Y. Peng, M.P. Oxley, K. Benthem, and M.F. Chisholm. page 152. Springer New York, 2007.
- [67] J. Wall A. V. Crewe and J. Langmore. *Science*, 168:1338, 1970.
- [68] Scanning transmission electron microscopy, http://en.wikipedia.org/wiki/Scanning_transmission_electron_microscopy. .
- [69] R. Babilas R. Nowosielski. *Physical Review Letters*, 108:195505, 2012.
- [70] X. K. Xi, D. Q. Zhao, M. X. Pan, W. H. Wang, Y. Wu, and J. J. Lewandowski. *Physical Review Letters*, 94:125510, 2005.
- [71] Scanning electron microscopy, http://en.wikipedia.org/wiki/Scanning_electron_microscopy.
- [72] Joseph I. Goldstein; Dale E. Newbury; Patrick Echlin; David C. Joy; Charles Fiori; Eric Lifshin. Springer New York, 1981.
- [73] A. C. Y. Liu, M. J. Neish, G. Stokol, G. A. Buckley, L. A. Smillie, M. D. de Jonge, R. T. Ott, M. J. Kramer, and L. Bourgeois. *Physical Review Letters*, 110:205505, 2013.

- [74] M. M. J. Treacy and K. B. Borisenko. *Science*, 335:950–953, 2012.
- [75] M. M. J. Treacy, J. M. Gibson, L. Fan, D. J. Paterson, and I. McNulty. *Reports on Progress in Physics*, 68:2899, 2005.
- [76] Fluctuation electron microscopy, http://www.public.asu.edu/~mtreacy/fluctuation_microscopy.htm .
- [77] R. Wiesendanger, L. Eng, H.R. Hidber, L. Rosenthaler, L. Scandella, U. Staufer, H.-J. Güntherodt, N. Koch, and M. Allmen. volume 11, page 595. Springer Berlin Heidelberg, 1988.
- [78] D.M. Kulawansa, J.T. Dickinson, and S.C. Langford. *Journal of Materials Research*, 8:2543, 1993.
- [79] Uwe Köster. *Materials Science and Engineering*, 97:233, 1988.
- [80] A. Zaluska, L. Zaluski, and A. Witek. *Materials Science and Engineering: A*, 122:251 – 255, 1989.
- [81] A. I. Oreshkin, V. N. Mantsevich, S. V. Savinov, S. I. Oreshkin, V. I. Panov, N. S. Maslova, and D. V. Louzguine-Luzgin. *Applied Physics Letters*, 101:181601, 2012.
- [82] Arribart H. and Abriou D. *Ceramics-Silikáty*, 44:121, 2000.
- [83] G. Binnig, C. F. Quate, and Ch. Gerber. *Physical Review Letters*, 56:930, 1986.
- [84] U. Ramamurty, S. Jana, Y. Kawamura, and K. Chattopadhyay. *Acta Materialia*, 53:705, 2005.
- [85] Small-angle x-ray scattering, http://en.wikipedia.org/wiki/Small-angle_X-ray_scattering.
- [86] C.P.Peter Chou and Frans Spaepen. *Acta Metallurgica*, 23:609, 1975.
- [87] T.W. Wu and F. Spaepen. *Acta Metallurgica*, 33:2185, 1985.
- [88] David B. Williams Ricardo B. Schwarz Faisal M. Alamgir, Himanshu Jain. *Micron*, 433:34, 2003.

- [89] V. Kokotin O. Shuleshova B. Beuneu K. Saksli N. Mattern J. Eckert A.L. Greer I. Kaban, P. Jovari. *Acta Materialia*, 61:2509, 2013.
- [90] Small-angle neutron scattering, http://en.wikipedia.org/wiki/Small-angle_neutron_scattering.
- [91] Hicter Pierre Maret Mireille, Chieux Pierre. *Zeitschrift für Physikalische Chemie*, 157:109, 2011.
- [92] Martin J. Hollamby. *Phys. Chem. Chem. Phys.*, 15:10566, 2013.
- [93] P. Lamparter and S. Steeb. *Journal of Non-Crystalline Solids*, 106:137, 1988.
- [94] Andrew J. Jackson. Nist center for neutron research, http://www.ncnr.nist.gov/summerschool/ss10/pdf/SANS_NR_Intro.pdf. 2008.
- [95] Yuri B. Melnichenko and George D. Wignall. *Journal of Applied Physics*, 102:021101, 2007.
- [96] J.-B. Suck and H. Rudin. volume 53 of *Topics in Applied Physics*, page 217. Springer Berlin Heidelberg, 1983.
- [97] T M Holden. *Journal of Physics F: Metal Physics*, 11:1737, 1981.
- [98] J.D. Axe. volume 20, page 507. Springer US, 1976.
- [99] H. A. Mook, N. Wakabayashi, and D. Pan. *Physical Review Letters*, 34:1029, 1975.
- [100] J. D. Axe, G. Shirane, T. Mizoguchi, and K. Yamauchi. *Physical Review B*, 15:2763, 1977.
- [101] H. A. Mook and C. C. Tsuei. *Physical Review B*, 16:2184, 1977.
- [102] J. A. Tarvin, G. Shirane, R. J. Birgeneau, and H. S. Chen. *Physical Review B*, 17:241, 1978.
- [103] A. P. Sokolov, A. Kisliuk, M. Soltwisch, and D. Quitmann. *Physical Review Letters*, 69:1540, 1992.
- [104] R. J. Hemley, H. K. Mao, P. M. Bell, and B. O. Mysen. *Physical Review Letters*, 57:747, 1986.

- [105] Michael Leitner, Bogdan Sepiol, Lorenz-Mathias Stadler, Bastian Pfau, and Gero Vogl. *Nat Mater*, 8:717, 2008.
- [106] B. Ruta, Y. Chushkin, G. Monaco, L. Ciletti, E. Pineda, P. Bruna, V. M. Giordano, and M. Gonzalez-Silveira. *Physical Review Letters*, 109:165701, 2012.
- [107] X-ray photon correlation spectroscopy (xpcs), <http://sector7.xray.aps.anl.gov/~dufresne/UofM/xpcs.html>. .
- [108] X-ray photon correlation spectroscopy (xpcs), http://www-conf.slac.stanford.edu/uxss/2012/presentations/UXSS_XPCS_Sikorski.pdf. .
- [109] C. A. Angell. *Science*, 267:1924, 1995.
- [110] B. Ruta, Y. Chushkin, G. Monaco, L. Cipelletti, E. Pineda, P. Bruna, V. M. Giordano, and M. Gonzalez-Silveira. *Physical Review Letters*, 109:165701, 2012.
- [111] P. Oelhafen, M. Liard, H.-J. Güntherodt, K. Berresheim, and H.D. Polaschegg. *Solid State Communications*, 30:641, 1979.
- [112] Photoemission spectroscopy, http://en.wikipedia.org/wiki/Photoemission_spectroscopy.
- [113] P. Oelhafen. *Materials Science and Engineering*, 99:239, 1988.
- [114] Peter Kizler. *Physical Review Letters*, 67:3555, 1991.
- [115] X-ray absorption spectroscopy, http://en.wikipedia.org/wiki/X-ray_absorption_spectroscopy. .
- [116] XAS and XES, <http://physics.usask.ca/~chang/homepage/xray/xray.html>. .
- [117] J. McLeod. *Behavioral Sciences*, 34:1, 1989.
- [118] M. P. Allen and D. J. Tildesley. *Computer Simulation of Liquids*. Oxford University Press, USA, 1989.

- [119] W. E. Morrell and J. H. Hildebrand. *The Journal of Chemical Physics*, 4: 224, 1936.
- [120] Nicholas Metropolis, Arianna W. Rosenbluth, Marshall N. Rosenbluth, Augusta H. Teller, and Edward Teller. *The Journal of Chemical Physics*, 21: 1087, 1953.
- [121] W. W. Wood and F. R. Parker. *The Journal of Chemical Physics*, 27:720, 1957.
- [122] B. J. Alder and T. E. Wainwright. *The Journal of Chemical Physics*, 27: 1208, 1957.
- [123] B. J. Alder and T. E. Wainwright. *The Journal of Chemical Physics*, 31: 459, 1959.
- [124] A. Rahman. *Physical Review*, 136:A405, 1964.
- [125] Laurent J. Lewis and Göran Wahnström. *Physical Review E*, 50:3865, 1994.
- [126] G.F. Signorini, J.L. Barrat, and M.L. Klein. *The Journal of Chemical Physics*, 8:563, 1974.
- [127] James R. Rustad, David A. Yuen, and Frank J. Spera. *Physical Review B*, 44:2108, 1991.
- [128] Wei Jin, Rajiv K. Kalia, Priya Vashishta, and José P. Rino. *Physical Review Letters*, 71:3146, 1993.
- [129] Peter H. Poole, Mahin Hemmati, and C. Austen Angell. *Physical Review Letters*, 79:2281, 1997.
- [130] Daniel J. Lacks. *Physical Review Letters*, 80:5385, 1998.
- [131] Hideki Tanaka. *Physical Review Letters*, 80:113, 1998.
- [132] Francesco Sciortino, Peter H. Poole, Ulrich Essmann, and H. E. Stanley. *Physical Review E*, 55:727, 1997.
- [133] James Badro, David M. Teter, Robert T. Downs, Philippe Gillet, Russell J. Hemley, and Jean-Louis Barrat. *Physical Review B*, 56:5797, 1997.

- [134] Glenn H. Fredrickson and Hans C. Andersen. *The Journal of Chemical Physics*, 83:5822, 1985.
- [135] Walter Kob and Hans C. Andersen. *Physical Review E*, 47:3281, 1993.
- [136] Walter Kob and Hans C. Andersen. *Physical Review E*, 48:4364, 1993.
- [137] Felix Ritort. *Physical Review Letters*, 75:1190, 1995.
- [138] U. Buchenau, M. Prager, N. Nücker, A. J. Dianoux, N. Ahmad, and W. A. Phillips. *Physical Review B*, 34:5665, 1986.
- [139] A. Wischnewski, U. Buchenau, A. J. Dianoux, W. A. Kamitakahara, and J. L. Zarestky. *Physical Review B*, 57:2663, 1998.
- [140] P.M. Derlet, R. Maaß, and J.F. Löffler. *The European Physical Journal B*, 85:1, 2012.
- [141] Katharina Vollmayr, Walter Kob, and Kurt Binder. *Physical Review B*, 54:15808, 1996.
- [142] Walter Kob. *Journal of Physics: Condensed Matter*, 11:R85, 1999.
- [143] A Takada, C R A Catlow, and G D Price. *Journal of Physics: Condensed Matter*, 7:8659, 1995.
- [144] A Takada, C R A Catlow, and G D Price. *Journal of Physics: Condensed Matter*, 7:8693, 1995.
- [145] D. Chandler. *Introduction to Modern Statistical Mechanics*. Oxford University Press, 1987.
- [146] Roman Petrenko and Jaroslaw Meller. *Molecular Dynamics*. John Wiley & Sons, Ltd, 2001.
- [147] M. T. Dove. *Seminarios de la Sociedad Española de Mineralogía*, 4:7, 2008.
- [148] E. R. Hernández. *AIP Conference Proceedings*, 1077:95, 2008.
- [149] Arthur F. Voter. volume 235, page 1. Springer Netherlands, 2007.

- [150] Monte carlo or molecular dynamics, http://cmt.dur.ac.uk/sjc/thesis_dlc/node58.html.
- [151] William L. Johnson. *MRS Proceedings*, 554:311, 1998.
- [152] Arthur F. Voter, Francesco Montalenti, and Timothy C. Germann. *Annu. Rev. Mat. Res.*, 32:321, 2002.
- [153] Daniel L. Ensign, Peter M. Kasson, and Vijay S. Pande. *Journal of Molecular Biology*, 374:806, 2007.
- [154] L. C. E. Struik. *Physical aging in amorphous polymers and other materials*. Elsevier North-Holland Amsterdam, 1978.
- [155] Ping Chen, P Boolchand, and D G Georgiev. *Journal of Physics: Condensed Matter*, 22:065104, 2010.
- [156] Thomas B. Schröder, Srikanth Sastry, Jeppe C. Dyre, and Sharon C. Glotzer. *The Journal of Chemical Physics*, 112:9834, 2000.
- [157] Martin Goldstein. *The Journal of Chemical Physics*, 51:3728, 1969.
- [158] Frank H. Stillinger and Thomas A. Weber. *Science*, 225:983,, 1984.
- [159] Frank H. Stillinger. *Physical Review E*, 59:48, 1999.
- [160] M. Scott Shell, Pablo G. Debenedetti, and Athanassios Z. Panagiotopoulos. *Physical Review Letters*, 92:035506, 2004.
- [161] Andreas Heuer. *Physical Review Letters*, 78:4051, 1997.
- [162] L. Angelani, G. Parisi, G. Ruocco, and G. Vilianni. *Physical Review E*, 61:1681, 2000.
- [163] David Rodney and Christopher Schuh. *Physical Review Letters*, 102:235503, 2009.
- [164] Frank H. Stillinger. *Science*, 267:1935,, 1995.
- [165] Francesco Delogu. *Physical Review Letters*, 100:255901, 2008.
- [166] S. G. Mayr. *Physical Review Letters*, 97:195501, 2006.

- [167] Akihiro Kushima, Xi Lin, Ju Li, Jacob Eapen, John C. Mauro, Xiaofeng Qian, Phong Diep, and Sidney Yip. *The Journal of Chemical Physics*, 130:224504, 2009.
- [168] CJ Cerjan and WH Miller. *Journal of Chemical Physics*, 75:2800, 1981.
- [169] G Henkelman and H Jonsson. *Journal of Chemical Physics*, 111:7010, 1999.
- [170] Lindsey J. Munro and David J. Wales. *Physical Review B*, 59:3969, 1999.
- [171] Srikanth Sastry, Pablo G. Debenedetti, and Frank H. Stillinger. *Nature*, 393:554, 1998.
- [172] Hannes Jónsson and Hans C. Andersen. *Physical Review Letters*, 60:2295, 1988.
- [173] Göran Wahnström. *Physical Review A*, 44:3752, 1991.
- [174] W Gotze and L Sjogren. *Reports on Progress in Physics*, 55:241, 1992.
- [175] W. Kob. *arXiv:cond-mat/9702073v1*, 1997.
- [176] Pablo G. Debenedetti and Frank H. Stillinger. *Nature*, 410:259, 2001.
- [177] F. Sciortino, W. Kob, and P. Tartaglia. *Physical Review Letters*, 83:3214, 1999.
- [178] Kurt Broderix, Kamal K. Bhattacharya, Andrea Cavagna, Annette Zippelius, and Irene Giardina. *Physical Review Letters*, 85:5360, 2000.
- [179] L. Angelani, R. Di Leonardo, G. Ruocco, A. Scala, and F. Sciortino. *Physical Review Letters*, 85:5356, 2000.
- [180] David J. Wales, Mark A. Miller, and Tiffany R. Walsh. *Nature*, 394:758, 1998.
- [181] Stephan Büchner and Andreas Heuer. *Physical Review Letters*, 84:2168, 2000.
- [182] R. Aldrin Denny, David R. Reichman, and Jean-Philippe Bouchaud. *Physical Review Letters*, 90:025503, 2003.

- [183] B. Doliwa and A. Heuer. *Physical Review E*, 67:031506, 2003.
- [184] B. Doliwa and A. Heuer. *Physical Review E*, 67:030501, 2003.
- [185] B. Doliwa and A. Heuer. *Physical Review Letters*, 91:235501, 2003.
- [186] Marcel Utz, Pablo G. Debenedetti, and Frank H. Stillinger. *Physical Review Letters*, 84:1471, 2000.
- [187] Gyan P. Johari and Martin Goldstein. *The Journal of Chemical Physics*, 53:2372, 1970.
- [188] Thomas F. Middleton and David J. Wales. *Physical Review B*, 64:024205, 2001.
- [189] G. A. Appignanesi, J. A. Rodriguez Fris, R. A. Montani, and W. Kob. *Physical Review Letters*, 96:057801, 2006.
- [190] Andreas Heuer. *Journal of Physics: Condensed Matter*, 20:373101.
- [191] Walter Kob and Hans C. Andersen. *Physical Review E*, 51:4626, 1995.
- [192] B. W. H. van Beest, G. J. Kramer, and R. A. van Santen. *Physical Review Letters*, 64:1955, 1990.
- [193] Yunfeng Shi and Michael L. Falk. *Physical Review B*, 73:214201, 2006.
- [194] David Chandler, Juan P. Garrahan, Robert L. Jack, Lutz Maibaum, and Albert C. Pan. *Physical Review E*, 74:051501, 2006.
- [195] Hiroshi Kobayashi, Haruyuki Takahashi, and Yosio Hiki. *Journal of Applied Physics*, 88:3776, 2000.
- [196] Maozhi Li, C. Z. Wang, S. G. Hao, M. J. Kramer, and K. M. Ho. *Physical Review B*, 80:184201, 2009.
- [197] Walter Kob and Jean-Louis Barrat. *Physica A: Statistical Mechanics and its Applications*, 263:234, 1999.
- [198] G. Kermouche B. Mantsi, A. Tanguy and E. Barthel. *Eur. Phys. J. B*, 85:304, 2012.

- [199] A. D. Buckingham, P. W. Fowler, and Jeremy M. Hutson. *Chemical Reviews*, 88:963, 1988.
- [200] Antoine Carré, Ludovic Berthier, Jürgen Horbach, Simona Ispas, and Walter Kob. *The Journal of Chemical Physics*, 127:114512, 2007.
- [201] P Jund, M Rarivomanantsoa, and R Jullien. *Journal of Physics: Condensed Matter*, 12:8777, 2000.
- [202] P. P. Ewald. *Annalen der Physik*, 369:253, 1921.
- [203] William C. Swope, Hans C. Andersen, Peter H. Berens, and Kent R. Wilson. *The Journal of Chemical Physics*, 76:637, 1982.
- [204] Hans C. Andersen. *The Journal of Chemical Physics*, 72:2384, 1980.
- [205] H. Jonsson, G. Mills, and W. Jacobsen. page 385. World Scientific, 1998.
- [206] H. Eyring. *Journal of Chemical Physics*, 3:107, 1935.
- [207] Arthur F. Voter and Jimmie D. Doll. *The Journal of Chemical Physics*, 80:5832, 1984.
- [208] George H. Vineyard. *Journal of Physics and Chemistry of Solids*, 3:121, 1957.
- [209] G. T. Barkema and Normand Mousseau. *Physical Review Letters*, 77:4358, 1996.
- [210] David Rodney and Christopher A. Schuh. *Physical Review B*, 80:184203, 2009.
- [211] Normand Mousseau and G. T. Barkema. *Physical Review E*, 57:2419, 1998.
- [212] G. T. Barkema and Normand Mousseau. *Physical Review Letters*, 81:1865, 1998.
- [213] Normand Mousseau and Laurent J. Lewis. *Physical Review B*, 56:9461, 1997.
- [214] Normand Mousseau, G. T. Barkema, and Simon W. de Leeuw. *The Journal of Chemical Physics*, 112:960, 2000.

- [215] C. Lanczos. *Applied Analysis*. Dover, New York, 1988.
- [216] Graeme Henkelman, Blas P. Uberuaga, and Hannes Jónsson. *The Journal of Chemical Physics*, 113:9901, 2000.
- [217] G. Z. Voronoi. *J. Reine u. Angew. Math.*, 134:199, 1908.
- [218] Voro++, <http://math.lbl.gov/voro++/>.
- [219] S. V. King. *Chemical Reviews*, 213:1112, 1967.
- [220] Sadanand Singh, M. D. Ediger, and Juan J. de Pablo. *Nature Materials*, 12:139, 2013.
- [221] Nikolaos P. Kopsias and Doros N. Theodorou. *The Journal of Chemical Physics*, 109:8573, 1998.
- [222] W. Meyer and H. Neldel. *Z. Tech. Phys.*, 18:588, 1937.
- [223] Ghyslain Boisvert, Laurent J. Lewis, and Arthur Yelon. *Physical Review Letters*, 75:469, 1995.
- [224] J C Dyre. *Journal of Physics C: Solid State Physics*, 19:5655, 1986.
- [225] A Yelon, B Movaghar, and R S Crandall. *Reports on Progress in Physics*, 69:1145, 2006.
- [226] Craig Maloney and Anael Lemaitre. *Physical Review Letters*, 93:195501, 2004.
- [227] Craig E. Maloney and Daniel J. Lacks. *Physical Review E*, 73:061106, 2006.
- [228] A. Carré, J. Horbach, S. Ispas, and W. Kob. *EPL (Europhysics Letters)*, 82:17001, 2008.
- [229] Yasuhiro Inamura, Yoshinori Katayama, Wataru Utsumi, and Ken-ichi Funakoshi. *Physical Review Letters*, 93:015501, 2004.
- [230] T. Rouxel, H. Ji, T. Hammouda, and A. Moréac. *Physical Review Letters*, 100:225501, 2008.

- [231] R. J. Hemley, H. K. Mao, P. M. Bell, and B. O. Mysen. *Physical Review Letters*, 57:747, 1986.
- [232] Jurgen Horbach and Walter Kob. *Physical Review B*, 60:3169, 1999.
- [233] C. J. Benmore, E. Soignard, S. A. Amin, M. Guthrie, S. D. Shastri, P. L. Lee, and J. L. Yarger. *Physical Review B*, 81:054105, 2010.
- [234] T. Deschamps, C. Martinet, D. de Ligny, and B. Champagnon. *Journal of Non-Crystalline Solids*, 355:1095, 2009.
- [235] R. L. Mozzi and B. E. Warren. *Journal of Applied Crystallography*, 2:164, 1969.
- [236] J. R. G. Da Silva, D. G. Pinatti, C. E. Anderson, and M. L. Rudee. *Philosophical Magazine*, 31:713, 1975.
- [237] Camille Sonnevile, Thierry Deschamps, Christine Martinet, Dominique de Ligny, Alain Mermet, and Bernard Champagnon. *Journal of Non-Crystalline Solids*, 382:133, 2013.
- [238] T. Deschamps, C. Martinet, D. de Ligny, and B. Champagnon. *Journal of Non-Crystalline Solids*, 355:1095, 2009.
- [239] David I. Grimley, Adrian C. Wright, and Roger N. Sinclair. *Journal of Non-Crystalline Solids*, 119:49, 1990.
- [240] J. H. Konnert and J. Karle. *Acta Crystallographica Section A*, 29:702, 1973.
- [241] Charles Meade, R. J. Hemley, and H. K. Mao. *Physical Review Letters*, 69:1387, 1992.
- [242] G. V. Gibbs. *American Mineralogist*, 67:421, 1982.
- [243] Jung-Fu Lin, Hiroshi Fukui, David Prendergast, Takuo Okuchi, Yong Q. Cai, Nozomu Hiraoka, Choong-Shik Yoo, Andrea Trave, Peter Eng, Michael Y. Hu, and Paul Chow. *Physical Review B*, 75:012201, 2007.
- [244] Tomoko Sato and Nobumasa Funamori. *Physical Review Letters*, 101:255502, 2008.

- [245] M. Wu, Y. Liang, J.Z. Jiang, and J.S. Tse. *Scientific Reports*, 2:398, 2012.
- [246] Tomoko Sato and Nobumasa Funamori. *Physical Review B*, 82:184102, 2010.
- [247] R. J. Hemley, H. K. Mao, P. M. Bell, and B. O. Mysen. *Physical Review Letters*, 57:747, 1986.
- [248] Wei Jin, Priya Vashishta, Rajiv K. Kalia, and Jose P. Rino. *Physical Review B*, 48:9359, 1993.
- [249] Elisabetta Venuti Raffaele Guido Della Valle. *Chemical Physics*, 179:411, 1994.
- [250] P.W. Bridgman and I. Simon. *Journal of Applied Physics*, 24:405, 1953.
- [251] D. Vandembroucq, T. Deschamps, C. Coussa, A. Perriot, E. Barthel, B. Champagnon, and C. Martinet. *J. Phys.: Condens. Matter*, 20:485221, 2008.
- [252] C. Sonnevile, A. Mermet, B. Champagnon, C. Martinet, J. Margueritat, D. de Ligny, T. Deschamps, and F. Balima. *Journal of Chemical Physics*, 137:124505, 2012.
- [253] Nobumasa Funamori and Tomoko Sato. *Physical Review Letters*, 102:209604, 2009.
- [254] V.V. Brazhkin. *Physical Review Letters*, 102:209603, 2009.
- [255] J.S. Tse, D.D. Klug, and Y. Le Page. *Physical Review B*, 46:5933, 1992.
- [256] W. Jin, R.K. Kalia, and P. Vashishta. *Physical Review B*, 50:118, 1994.
- [257] R.G. Della Valle and E. Venuti. *Physical Review B*, 54:3809, 1996.
- [258] D.J. Lacks. *Physical Review Letters*, 80:5385, 1998.
- [259] K. Trachenko and M.T. Dove. *Physical Review B*, 67:064107, 2003.
- [260] J.F. et al. Lin. *Physical Review B*, 75:012201, 2007.

Résumé: Les matériaux amorphes sont omniprésents dans la vie quotidienne. Leur utilisation est cependant limitée en raison d'une structure désordonnée à l'échelle atomique. Les études de la plasticité des solides amorphes sont encore gênées par l'absence de tout défaut identifiable responsable de la plasticité. Il est reconnu que la plasticité est le résultat des transformations de réarrangements locaux, impliquant des petits groupes de particules. Ces réarrangements sont thermiquement activés et sont communs dans le processus de relaxation structurelle des verres à basse température. Le but de cette thèse était de prédire les cinétiques thermiquement activées dans des verres métalliques et de silice. La nature de ces événements microscopique qui se produisent dans des systèmes désordonnés a été étudiée à la fois sous des contraintes mécaniques et dans des conditions de vieillissement, suivie par l'étude de leur influence sur l'ordre atomique local dans ces matériaux.

Abstract: Amorphous materials are ubiquitous in everyday life and present at all levels of industry and technology. Their usage, however, is limited due to a disordered structure at the atomic level. Studies of plasticity in amorphous solids, are still hampered by the lack of any identifiable defect responsible for the plastic response. It is acknowledged that plasticity is the result of shear transformations - local rearrangements involving small clusters of particles. These rearrangements are thermally activated and are ubiquitous processes in the structural relaxation and deformation of glasses at low temperatures. The purpose of this thesis was the prediction of thermally activated kinetics in metallic and silica glasses. The nature of such microscopic events occurring in disordered systems was studied both under mechanical stress and in ageing conditions, followed by the investigation of their influence on the local atomic order in these materials.